UNIVERSIDAD NACIONAL DEL LITORAL

DOCTORADO EN INGENIERÍA

Modelado y simulación de fenómenos de flujo y transporte en medios porosos integrados a dispositivos de microfluídica

Gabriel Santiago Gerlero

FICH
FACULTAD DE INGENIERÍA Y CIENCIAS HÍDRICAS

INTEC
INSTITUTO DE DESARROLLO TECNOLÓGICO PARA LA INDUSTRIA QUÍMICA

CIMEC
CENTRO DE INVESTIGACIÓN EN MÉTODOS COMPUTACIONALES

sinc(*i*)
INSTITUTO DE INVESTIGACIÓN EN SEÑALES, SISTEMAS E INTELIGENCIA COMPUTACIONAL

Tesis de Doctorado **2024**

UNIVERSIDAD NACIONAL DEL LITORAL

Facultad de Ingeniería y Ciencias Hídricas

Instituto de Desarrollo Tecnológico para la Industria Química

Centro de Investigación en Métodos Computacionales

Instituto de Investigación en Señales, Sistemas e Inteligencia Computacional

MODELADO Y SIMULACIÓN DE FENÓMENOS DE FLUJO Y TRANSPORTE EN MEDIOS POROSOS INTEGRADOS A DISPOSITIVOS DE MICROFLUÍDICA

Gabriel Santiago Gerlero

Tesis remitida al Comité Académico del Doctorado

como parte de los requisitos para la obtención

del grado de

DOCTOR EN INGENIERÍA

Mención Mecánica Computacional

de la

UNIVERSIDAD NACIONAL DEL LITORAL

2024

UNIVERSIDAD NACIONAL DEL LITORAL

Facultad de Ingeniería y Ciencias Hídricas

Instituto de Desarrollo Tecnológico para la Industria Química

Centro de Investigación en Métodos Computacionales

Instituto de Investigación en Señales, Sistemas e Inteligencia Computacional

MODELADO Y SIMULACIÓN DE FENÓMENOS DE FLUJO Y TRANSPORTE EN MEDIOS POROSOS INTEGRADOS A DISPOSITIVOS DE MICROFLUÍDICA

Gabriel Santiago Gerlero

Lugar de Trabajo:

CIMEC (UNL–CONICET)

Centro de Investigación en Métodos Computacionales

Facultad de Ingeniería y Ciencias Hídricas

Universidad Nacional del Litoral

Director:

Dr. Pablo Alejandro Kler — CIMEC (UNL–CONICET)

Co-director:

Dr. Claudio Luis Alberto Berli — INTEC (UNL–CONICET)

Jurado Evaluador:

Dr. Gustavo Buscaglia — Instituto de Ciências Matemáticas e de Computação (USP)

Dr. Axel Larreteguy — Universidad Argentina de la Empresa

Dr. Sebastián Ubal — IBB (UNER–CONICET)

2024

Certificación

Declaración legal del autor

Esta Tesis ha sido remitida como parte de los requisitos para la obtención del grado de Doctor ante la Universidad Nacional del Litoral y ha sido depositada en la Biblioteca de la Facultad de Ingeniería y Ciencias Hídricas para que esté disponible a sus lectores bajo las condiciones estipuladas por el Reglamento de la mencionada Biblioteca.

Citaciones breves de esta disertación son permitidas sin la necesidad de un permiso especial, en la suposición de que la fuente sea correctamente citada. Solicitudes de permiso para una citación extendida o para la reproducción de este manuscrito en un todo o en parte serán exigidas por el portador legal del derecho de propiedad intelectual de la misma.

Gabriel Santiago Gerlero

Aclaración

La presente tesis se encuentra organizada bajo el formato de Tesis por Compilación, aprobado en la resolución Nº 255/17 (Expte. Nº 888317-17) por el Comité Académico de la Carrera de Doctorado en Ingeniería, Facultad de Ingeniería y Ciencias Hídricas, Universidad Nacional del Litoral. Dicha resolución estipula:

"En el caso de optar por la Tesis por Compilación, ésta consistirá en una descripción técnica de al menos 30 páginas, redactada en español e incluyendo todas las investigaciones abordadas en la tesis. Se deberán incluir las secciones habituales indicadas a continuación en la Sección Contenidos de la Tesis. Los artículos científicos publicados por el autor, en el idioma original de las publicaciones, deberán incluirse en un Anexo con el formato unificado al estilo general de la Tesis indicado en la Sección Formato. El Anexo deberá estar encabezado por una sección donde el tesista detalle para cada una de las publicaciones cuál ha sido su contribución. Esta sección deberá estar avalada por su director de Tesis. El documento central de la Tesis debe incluir referencias explícitas a todas las publicaciones anexadas y presentar una conclusión que muestre la coherencia de dichos trabajos con el hilo conceptual y metodológico de la tesis. Los artículos presentados en los anexos podrán ser artículos publicados, aceptados para publicación (en prensa) o en revisión."

A la ciencia y tecnología, que nunca me defraudaron; y a las que espero no defraudar.

Agradecimientos

Nunca el aprendizaje es un proceso individual: siempre están “los otros” mediatizando los conocimientos y observando y guiando los procesos para convertirlos en logros. Por eso es que mis agradecimientos son múltiples y profundos.

En primer lugar, a la UTN, que me otorgó el título de grado que me permitió aspirar a nuevos horizontes. A la UNL, que luego me adoptó como alumno, y que además me permitió estrenarme como docente. Al CONICET, que me brindó el ámbito, las herramientas y su gente para que me desarrollara profesionalmente.

Mención aparte merece mi director de tesis, el Dr. Pablo Alejandro Kler, por haber confiado tanto en mí y por haberme dado la libertad y el espacio para desarrollar mi tesis con una permanente guía en la que manifestó tanto su profunda sabiduría humana como sus vastos conocimientos profesionales. A mi co-director, el Dr. Claudio Luis Alberto Berli, que siempre me asesoró desde el lugar de la experiencia y el saber, pero buscando que yo alcanzara mi autonomía.

A mis compañeros de CIMEC; los que pasaron y los que hoy están: a todos, porque de todos aprendí y me ayudaron a crecer personal y profesionalmente. A quienes comparten mi pasión por el desarrollo de software, estén donde estén. Y al Grupo Santafesino de Microfluídica, por hacer de la interdisciplinariedad una fuente inagotable de conocimientos e inspiración.

A mi novia Joana, con quien compartí todos los momentos desde el inicio de este camino hacia el doctorado.

Finalmente, a mi familia, por la confianza inmensa, el afecto incondicional y el apoyo integral.

Índice general

Índice de figuras

Índice de tablas

Resumen

Los dispositivos de microfluídica analíticos basados en papel (μPADs) tienen numerosas ventajas: disponibilidad, bajo costo, autonomía, biocompatibilidad, compatibilidad con reacciones incluyendo especies pre-adsorbidas y potencial de empleo de electroforesis.

En las etapas de diseño y optimización de estos dispositivos, son de gran utilidad las simulaciones computacionales. Las simulaciones permiten a los diseñadores de los dispositivos probar diferentes configuraciones, materiales y condiciones de operación de manera virtual, antes de pasar a la fabricación física. Esto no solo ahorra tiempo y recursos, sino que también proporciona una comprensión más profunda del comportamiento de los dispositivos en diferentes situaciones.

La principal contribución de esta tesis consiste en el desarrollo, validación y publicación de varias herramientas de software numéricas de código abierto para la simulación de flujo y/o transporte en medios porosos destinadas a la caracterización de sustratos y el prototipado numérico de μPADs. Estas herramientas se pueden usar para predecir comportamientos y resultados, y así optimizar diseños sin necesidad de utilizar prototipos físicos. En conjunto con estas herramientas, se han estudiado, extendido, validado e implementado relaciones constitutivas aplicables al flujo capilar en papel.

Las herramientas y modelos originales desarrollados constituyen un aporte significativo a la comunidad científico-tecnológica dedicada a esta temática, el cual se ve reflejado en las publicaciones con referato que compila esta tesis.

Abstract

Microfluidic paper-based analytical devices (μPADs) offer numerous advantages: availability, low cost, autonomy, biocompatibility, compatibility with reactions including pre-adsorbed species, and the potential for performing electrophoresis.

In the design and optimization stages of these devices, computational simulations are highly useful. Simulations enable device designers to test different configurations, materials, and operating conditions in a virtual manner before moving on to physical fabrication. This not only saves time and resources but also provides a deeper understanding of the devices' behavior in various situations.

The main contribution of this thesis lies in the development, validation, and publication of several open-source numerical software tools for simulating flow and/or transport in porous media, aimed at the characterization of substrates and numerical prototyping of μPADs. These tools can be used to predict behaviors and outcomes, thus optimizing designs without the need for physical prototypes. In conjunction with these tools, constitutive relations applicable to capillary flow in paper have been studied, extended, validated, and implemented.

The original tools and models developed constitute a significant contribution to the scientific and technological community dedicated to this topic, as reflected in the peer-reviewed publications compiled in this thesis.

Capítulo 1

Introducción

La microfluídica comprende la ciencia y la tecnología de la manipulación de fluidos en dispositivos artificiales donde los volúmenes involucrados son menores al microlitro. Debido al amplio rango de problemas fundamentales y aplicados, este campo de investigación y desarrollo es esencialmente multidisciplinario. En el área del diagnóstico clínico, la microfluídica busca desarrollar dispositivos autónomos portátiles, no solamente para atender a poblaciones aisladas, sino también para emergencias, salas de cirugía, puntos de atención, y cuidado personal. Estos microsistemas buscan prevenir diseminación de enfermedades, evaluar resultados de tratamientos y controlar el uso de medicamentos *in situ*, aumentando la eficiencia y disminuyendo considerablemente los costos de asistencia sanitaria. También son importantes los aportes de la microfluidica en el monitoreo ambiental, los controles bromatológicos y la producción y/o síntesis de drogas y sustancias de muy alto valor agregado, entre otras muchas aplicaciones [Mesquita et al., 2022, Liu et al., 2021]

Los dispositivos de microfluídica analíticos construidos en base a sustratos porosos (µPADs por sus siglas en inglés), tales como el papel y otros derivados de la celulosa o fibra de vidrio, entre otros, ofrecen varias ventajas: tienen gran disponibilidad y bajo costo, son autónomos—pues permiten el flujo autopropulsado mediante capilaridad—, son compatibles con los sistemas biológicos, permiten la adsorción/desorción de proteínas para reacciones enzimáticas y/o antígeno–anticuerpo, y, una vez embebidos, pueden facilitar la interacción con campos eléctricos—ya sea para separaciones electroforéticas o para detección electroquímica—[Modha et al., 2021, Ozer et al., 2020]. Estas propiedades hacen que estos dispositivos sean idóneos para la detección de patógenos y diagnóstico de enfermedades infecciosas, entre otros ensayos químicos [Kim et al., 2020]. En efecto, el papel cumple con todos los requisitos fijados por la OMS para desarrollar tecnologías de diagnóstico para el control y tratamiento en sectores de bajos recursos, que son las poblaciones mayormente afectadas por las patologías infecciosas [Yager et al., 2006].

La mecánica computacional es una disciplina que contempla el uso de métodos computaciona-

les para resolver problemas de la física. En el ámbito de la microfluídica, las simulaciones computacionales han demostrado tener una gran utilidad en el desarrollo y optimización de dispositivos. En particular, en el desarrollo de los dispositivos de microfluídica basados en papel, adquiere notoria importancia el empleo de prototipos numéricos. Las simulaciones numéricas contribuyen a acelerar los procesos de diseño, ya que evitan iteraciones empíricas sobre prototipos reales [Schaumburg et al., 2018a].

Esta tesis doctoral se encuentra en el marco disciplinar aplicado de la microfluídica, tomando como soporte fundamental las ciencias de la computación; y en particular la mecánica computacional. Los objetivos planteados, reflejan un intento de síntesis entre esos campos del conocimiento, con una directriz de dar un soporte y así lograr contribuir al desarrollo de aplicaciones ingenieriles.

1.1. Objetivos

1.1.1. Objetivo general

El objetivo general de la presente tesis ha sido el desarrollo de modelos matemáticos, métodos numéricos y programas de computación originales para la simulación de fenómenos de flujo y transporte en medios porosos, orientados al diseño y desarrollo de dispositivos de microfluídica basados en papel con aplicaciones analíticas (µPADs).

1.1.2. Objetivos específicos

En particular, esta tesis contempló los siguientes objetivos específicos:

1. investigar posibles esquemas de modelado y desarrollar y validar herramientas numéricas para simulación de flujo no saturado en sustratos porosos de uso en microfluídica, con enfoque especial en casos de flujo lateral y el tratamiento de problemas inversos de estimación de parámetros;

2. proponer y validar experimental y numéricamente modelos de flujo no saturado aplicables a microfluídica en papel;

3. desarrollar y validar herramientas numéricas para simulaciones de transporte en condiciones de flujo saturado y con presencia de campos eléctricos en sustratos de uso en microfluídica (e-µPADs);

4. desarrollar y validar herramientas numéricas que resuelvan flujo y transporte reactivo acoplados en medios porosos no saturados para prototipado numérico de dispositivos microfluidicos en papel.

1.2. Antecedentes

El adecuado tratamiento numérico del comportamiento de los dispositivos implica no sólo el modelado en varias dimensiones de los flujos de las fases involucradas (normalmente, un líquido muestra y el aire), sino también del transporte de las especies, así como de otros fenómenos inherentes al ensayo en cuestión, como reacciones químicas y efectos causados por los campos eléctricos.

1.2.1. Flujo lateral y problemas inversos

El flujo de fluidos en medios porosos no saturados puede modelarse con la ecuación de Richards [Richards, 1931]. Esta es una ecuación diferencial parcial no lineal que describe los cambios en el contenido de humedad y/o presión debido a los efectos de la gravedad y la acción capilar. Los modelos de flujo en medios porosos proporcionan expresiones de relaciones constitutivas necesarias [Sun et al., 2021]. Un caso especial de la ecuación de Richards ocurre cuando el flujo es horizontal o cuando el efecto de la gravedad puede ser despreciado; en este caso también se la conoce como la ecuación de difusión de la humedad [Bear and Cheng, 2010].

Como ecuación diferencial parcial, la ecuación de Richards se resuelve comúnmente con métodos numéricos basados en métodos de diferencias finitas, elementos finitos o volúmenes finitos, emparejados con iteración de punto fijo (método de Picard) o el método de Newton-Raphson para lidiar con los términos no lineales [Farthing and Ogden, 2017, List and Radu, 2016, Lai and Ogden, 2015, Caviedes-Voullième et al., 2013]. Los paquetes de software que siguen estos esquemas están ampliamente disponibles y se utilizan en hidrología, y van desde herramientas diseñadas exclusivamente para casos unidimensionales [Šimůnek et al., 2016] hasta otras que extienden el soporte a geometrías arbitrarias [Horgue et al., 2022]. Sin embargo, los términos no lineales mencionados incluidos en las ecuaciones a resolver implican serios desafíos computacionales para estos métodos, y por lo tanto, la investigación sobre esquemas numéricos mejorados para estas aplicaciones aún está en curso. Tal investigación puede considerar geometrías unidimensionales verticales u horizontales. En el primer grupo, por ejemplo, List and Radu [2016] propusieron un nuevo esquema de linealización con mejores propiedades de convergencia; Alastal and Ababou [2019] desarrollaron un método particular llamado *Moving Multi-Front* para resolver la ecuación de Richards para flujo

no saturado en columnas porosas homogéneas verticales, y Shanmugam et al. [2020] presentaron un esquema de ponderación para el cálculo de conductividades hidráulicas que puede producir resultados más precisos.

Alternativamente, en presencia de flujo horizontal, la ecuación de Richards es susceptible a la transformación de Boltzmann [Boltzmann, 1894]. Esta transformación de semejanza reduce la ecuación diferencial parcial no lineal a una ecuación diferencial ordinaria no lineal equivalente, y puede aplicarse a problemas de flujo horizontal en dominios semi-infinitos [Bear and Cheng, 2010]. Este enfoque ha sido adoptado por investigadores que buscan soluciones analíticas a problemas de flujo no saturado [Philip, 1960, Prevedello et al., 2008, Su et al., 2017]; sin embargo, las soluciones exactas se limitan a problemas con funciones de difusividad restringidas a algunas formas particulares, excluyendo aquellas actualmente aceptadas como las más precisas. Más recientemente, la transformación de Boltzmann se ha aplicado en la formulación de métodos semi-analíticos para estos problemas [Chen and Dai, 2015, Tzimopoulos et al., 2015]. Hayek [2018] presentó un método analítico aproximado general para la ecuación de Richards en flujo horizontal; desafortunadamente, como se discute en el documento, el método es incompatible con ciertos modelos constitutivos (notablemente, el modelo de Van Genuchten). Mathias and Sander [2021] presentaron un método pseudoespectral para resolver directa e inversamente la ecuación de Richards horizontal basado en el software propietario MATLAB. La transformación de Boltzmann también se ha utilizado en problemas inversos de flujo horizontal donde el perfil de saturación puede aproximarse con una función analítica [Evangelides et al., 2010].

Es importante destacar que la transformación de Boltzmann también puede ser útil combinada con un tratamiento numérico estándar [Klute, 1952, Philip, 1955, Braddock and Parlange, 1980, Andersen, 2023], lo que resulta en un esquema más eficiente (y/o más preciso) frente a los métodos numéricos tradicionales utilizados para la ecuación de Richards. Específicamente, dicho esquema puede evitar la necesidad de iteraciones de paso de tiempo. Además, es posible evitar el requisito de una malla computacional como entrada al programa, lo que hace que el *solver* sea más fácil de usar. Asimismo, en comparación con un método analítico aproximado, el enfoque numérico no sufre de la incompatibilidad que aparece cuando el gradiente de la función de difusividad tiende a infinito bajo condiciones límite para la saturación, como lo señaló Hayek [2018].

Relacionado a estos aspectos presentados respecto al flujo lateral y problemas inversos, en el marco de esta tesis se presenta *Fronts* [Gerlero et al., 2023], una herramienta numérica para resolver casos horizontales de la ecuación de Richards con la aplicación de la transformación de Boltzmann. Como tal, *Fronts* está diseñado para manejar problemas donde el flujo ocurre a lo largo de un solo eje y los dominios pueden considerarse semi-infinitos. Construido con el objetivo de

ser de código abierto, más fácil de usar y más rápido que las herramientas existentes que pueden resolver estos problemas, el software tiene implementaciones independientes en dos lenguajes de programación diferentes: Python y Julia, con versiones cargadas en el registro oficial de paquetes de cada ecosistema. Ambas variantes incluyen los *solvers*, un conjunto de casos de tutorial y documentación de referencia en línea que especifica su uso. La elección de los entornos refleja las tendencias actuales de uso en la computación científica, con Python como un entorno popular para este tipo de aplicaciones, mientras que Julia es un lenguaje más nuevo con propiedades especiales que favorecen su adopción para aplicaciones numéricas donde los tiempos de cálculo son un factor importante [Bezanson et al., 2017]. *Fronts* puede utilizarse tanto para resolver problemas en los que se conocen las funciones hidráulicas subyacentes, seleccionadas de una biblioteca de modelos constitutivos integrados, o proporcionadas arbitrariamente por los usuarios; así como para problemas inversos en los que se deben encontrar los parámetros de un modelo constitutivo (también arbitrario). *Fronts* fue desarrollado pensando en la comunidad en general, aunque se identifica un campo de aplicación más específico en microfluídica basada en papel [Schaumburg et al., 2018b, Asadi et al., 2022].

1.2.2. Modelos de flujo no saturado

La microfluídica basada en papel ha crecido de manera continua en la última década, principalmente debido a sus capacidades para la implementación de ensayos químicos y bioquímicos portátiles [Salentijn et al., 2018]. Las ventajas ofrecidas por los dispositivos analíticos basados en papel han sido ampliamente reportadas en la literatura [Ozer et al., 2020], sin embargo, pueden resumirse como: bajos costos de fabricación, transporte, operación (debido a pequeños volúmenes de reactantes) y disposición final; junto con la compatibilidad con diferentes métodos de detección (a veces involucrando dispositivos móviles [Hassan et al., 2020, Schaumburg et al., 2022]) que los hacen fáciles de usar por personal no capacitado [Kim et al., 2020]. La característica más importante y atractiva de todos los dispositivos microfluídicos basados en papel es la capacidad de bombear fluidos sin ninguna fuente de energía externa, con la sola acción de las fuerzas capilares debido a la naturaleza absorbente de las fibras de celulosa [Modha et al., 2021]. El flujo capilar en los dispositivos microfluídicos basados en papel ha sido explotado desde los primeros trabajos a principios del siglo XX [Yetisen et al., 2013], posteriormente con el uso generalizado de ensayos de flujo lateral [Berli and Kler, 2016], y recientemente en aplicaciones más complejas [Mora et al., 2019]. Especialmente al considerar estos desarrollos recientes que involucran disposiciones experimentales complejas de varias capas y pasos [Schaumburg and Berli, 2019], un control preciso y exacto del flujo de fluidos es crítico.

Desafortunadamente, el control del flujo de fluidos en dispositivos microfluídicos basados en papel ha sido estudiado principalmente a través de enfoques empíricos debido a las siguientes dos razones [Franck et al., 2021]: (i) como se mencionó anteriormente, los procesos de fabricación son asequibles, y múltiples experimentos con diferentes disposiciones y condiciones operativas pueden llevarse a cabo simultáneamente dentro de plazos razonables [Yamada et al., 2017]; y (ii), dado que el papel es una estructura porosa intrincada de fibras entrelazadas, las predicciones de los comportamientos del flujo son particularmente desafiantes y, actualmente, no hay modelos matemáticos robustos y validados disponibles [Schaumburg et al., 2018b]. Este enfoque empírico ciertamente ha sido efectivo para configuraciones de ensayos de flujo lateral y dispositivos simples; pero a medida que los dispositivos microfluídicos basados en papel se han vuelto más complejos, se requieren modelos más generales y precisos del flujo [Lim et al., 2019].

En este punto, podemos discriminar entre condiciones de flujo saturado y no saturado. Es frecuente en la comunidad de microfluídica basada en papel emplear modelos matemáticos simplificados de dispositivos que operan bajo condiciones de flujo saturado, es decir, cuando todo el dominio operativo del dispositivo está completamente mojado [Schaumburg et al., 2018a]. Cuando se asumen condiciones de flujo saturado, la Ley de Darcy es suficiente para modelar el flujo: con la permeabilidad constante, sólo las condiciones de contorno de presión son suficientes para obtener una solución válida para el campo de velocidad [Gerlero et al., 2021b]. Sin embargo, considerar un dominio completamente saturado excluye los efectos locales de la capilaridad. Además, las condiciones de flujo no saturado son las que son realmente críticas para el rendimiento analítico de los dispositivos basados en papel en general, que en muchos casos prácticos contienen reactivos preadsorbidos como partículas marcadoras o anticuerpos (entre otros) que son transportados por el frente de fluido infiltrante [Rath and Toley, 2021].

Las condiciones de flujo no saturado durante los procesos de imbibición son extremadamente complejas y fueron estudiadas inicialmente mediante modelos basados en la Ecuación de Lucas-Washburn [Elizalde et al., 2016, Pan et al., 2021]. Tales modelos son apropiados para determinar la posición del frente de mojado de manera promediada en presencia de infiltración unidimensional, pero no son capaces de describir las formas observables de tales frentes, ni pueden aplicarse en dominios bidimensionales o tridimensionales [Bear and Cheng, 2010]. Para describir precisamente los frentes de fluido durante los procesos de imbibición, se debe tener en cuenta adecuadamente la dependencia de la presión capilar y la permeabilidad con la saturación [Santagata et al., 2020]. Vale la pena señalar que no sólo la saturación es importante para estas aplicaciones: el campo de velocidad del flujo, obtenido de derivadas de la saturación, permite un modelado adicional del transporte escalar con ecuaciones de convección-difusión-reacción [Gamazo et al., 2016], crucial

para el diseño de dispositivos analíticos microfluídicos basados en papel.

La ecuación de Richards [Richards, 1931] es la más aceptada para describir el flujo de fluidos en medios porosos no saturados [Hertaeg et al., 2020]. Cuando se consideran dispositivos microfluídicos basados en papel, se produce el caso especial previamente mencionado de la ecuación de Richards en el cual la gravedad puede ser despreciada (debido a la posición habitual de los dispositivos y/o el efecto insignificante de la gravedad verificado mediante números de Bond extremadamente bajos y longitudes de mojado extremadamente grandes [Das and Mitra, 2013]). Para el flujo capilar espontáneo, podemos reducir la ecuación de Richards en términos del contenido volumétrico de humedad (θ) para obtener una ecuación de tipo difusión no lineal. Esta ecuación es conocida como la ecuación de difusión de humedad, y la condición clave para el éxito de esta ecuación como un modelo válido para el flujo de imbibición es la función de difusividad de humedad $D(\theta)$ [Bear and Cheng, 2010]. Modelos hidráulicos para $D(\theta)$ tales como los propuestos por Brooks and Corey [1964] y Van Genuchten [1980] proporcionan expresiones parametrizadas en forma cerrada para dicha función.

Resolver adecuadamente la ecuación de difusión de humedad puede proporcionar una herramienta importante para mejoras racionales en el diseño de dispositivos microfluídicos basados en papel. El éxito de este proceso numérico está sujeto al uso de un modelo robusto y correcto para $D(\theta)$ y la implementación de una herramienta numérica eficiente para resolver la Ecuación (2.5) con diferentes funciones $D(\theta)$, como la que se propone el primer objetivo de la tesis. Al definir un modelo robusto y correcto para $D(\theta)$, es importante mencionar aquí que los modelos más reconocidos (los ya mencionados modelos de Brooks and Corey [1964] y Van Genuchten [1980]) fueron desarrollados originalmente considerando componentes de suelo comunes (por ejemplo, arena, rocas, arcilla) como sustratos. Claramente, la estructura microscópica del papel difiere de estos componentes de suelo, por lo que pueden necesitarse consideraciones especiales para obtener resultados adecuados de tales modelos. Se ha realizado una cantidad limitada de trabajo tratando de caracterizar sustratos de papel siguiendo estos modelos clásicos orientados al suelo, sin llegar a resultados consistentes y reproducibles [Perez-Cruz et al., 2017, Rath et al., 2018, Rath and Toley, 2021]. La misma situación ocurrió al utilizar otros modelos alternativos [Cummins et al., 2017, Ruoff et al., 1959, 1960, Philip, 1955]. En el desarrollo de esta tesis, se detectó la necesidad de una prueba objetiva de la idoneidad de estos modelos para aplicaciones microfluídicas basadas en papel [Terzis et al., 2018].

Más recientemente, se presentó un conjunto alternativo de correlaciones por Lomeland et al. [2005]. Estos modelos fenomenológicos con el nombre “LET” están orientados hacia el flujo multifásico en suelos, particularmente para aplicaciones en recuperación asistida de petróleo [Lomeland

and Ebeltoft, 2008, Lomeland, 2018]. La gran cantidad de parámetros presentes en los modelos LET permite simplificaciones para producir un nuevo modelo con menos parámetros compatible con aplicaciones microfluídicas basadas en papel. Introduciremos en esta tesis un modelo basado en tal simplificación llamado "LETd", cuyos fundamentos matemáticos se pueden encontrar en la siguiente sección.

En esta tesis, se proponen pruebas objetivas y una discusión sobre la idoneidad de diferentes modelos contemporáneos $D(\theta)$ para representar la dinámica de imbibición de flujo de fluidos en sustratos de papel realizando primero experimentos del proceso de imbibición bajo condiciones controladas y reproduciendo estos frentes de fluido experimentales para encontrar los mejores ajustes de parámetros de los modelos, mostrando las capacidades reales de cada modelo para representar la función de contenido de humedad $\theta(x, t)$ como función del espacio y el tiempo. A través de este estudio, se ofrecen a la comunidad de la microfluídica basada en papel nuevas herramientas para mejorar el diseño de dispositivos.

1.2.3. Flujo y transporte electroforético en medios porosos saturados

Los dispositivos analíticos electroforéticos basados en papel (e-µPADs) han cobrado relevancia en los últimos años debido al auge de los dispositivos microfluídicos basados en papel, utilizados principalmente en diagnósticos en el punto de atención, pero también en otras aplicaciones analíticas [Salentijn et al., 2018]. Las razones detrás de este crecimiento exponencial de las tecnologías basadas en papel se discuten extensamente en la literatura contemporánea [Gong and Sinton, 2017]—pero en resumen, los bajos costos y el alto potencial para su utilización por trabajadores no capacitados en entornos de bajos recursos y con poblaciones remotas, junto con la integración con teléfonos inteligentes y dispositivos móviles, entre otros, crearon el escenario adecuado para esta expansión [Schaumburg et al., 2020b, 2022]. Paradójicamente, las separaciones electroforéticas basadas en papel fueron estudiadas por primera vez hace 70 años, con los trabajos pioneros de Arne Tiselius sobre la separación de proteínas séricas [Cremer et al., 1950, Kunkel and Tiselius, 1951]. Posteriormente, la electroforesis evolucionó a geles y capilares de sílice fundida, y últimamente a chips microfluídicos [Shapiro et al., 1967, Jorgenson and Lukacs, 1981, Ocvirk et al., 2000].

La evolución de la electroforesis contemporánea basada en capilares de sílice fundida estuvo acompañada de descripciones matemáticas adecuadas de los fenómenos involucrados [Bier et al., 1983], y consecuentemente enriquecida con métodos numéricos consistentes para una predicción racional del resultado de experimentos y la optimización de condiciones operativas [Hruška et al., 2006, Thormann et al., 2007, Bercovici et al., 2009]. Tales métodos numéricos se expandieron naturalmente a aplicaciones de chips microfluídicos, ofreciendo implementaciones paralelas 3D

y de alto rendimiento [Márquez Damián et al., 2019, Dovhunová et al., 2020] que aún conservan los mismos modelos matemáticos que describen los fenómenos fisicoquímicos: no han cambiado ninguna condición experimental intrínseca, sino sólo la geometría del dominio computacional.

A pesar del hecho mencionado anteriormente de que las separaciones electroforéticas basadas en papel ya se estudiaron hace 70 años, su desarrollo fue rápidamente abandonado por dos razones: (i) las separaciones basadas en geles y capilares proporcionaron más robustez y reproducibilidad; y (ii) modelar los fenómenos en medios porosos estocásticos como el papel aún no era posible, y por lo tanto, los desarrolladores de e-µPADs carecían de una herramienta racional para la optimización de dispositivos y condiciones experimentales [Schaumburg et al., 2018b]. La complejidad matemática de estos modelos y la baja reproducibilidad de los experimentos para validación retrasaron este proceso.

Con el advenimiento de la nueva ola de microfluídica basada en papel, este escenario ha cambiado notablemente. Por un lado, los sustratos de papel se han vuelto industrialmente más reproducibles y algunos sustratos fueron adoptados como estándares por la comunidad científica, como el papel Whatman #1 y la nitrocelulosa [Mora et al., 2019]. Varias separaciones electroforéticas fueron reportadas en la literatura reciente: por ejemplo, electroforesis de zona basada en papel (PZE) para aminoácidos [Ge et al., 2014] y pequeñas moléculas inorgánicas [Xu et al., 2016, Chagas et al., 2016], así como isotacoforésis (ITP) para aumentar la eficiencia del análisis de flujo lateral (LFA) [Moghadam et al., 2014, Rosenfeld and Bercovici, 2014]. Por otro lado, los sustratos de papel han sido objeto de estudios sistemáticos para obtener modelos matemáticos confiables para una descripción integral de todos los fenómenos acoplados que rigen los diferentes procesos de transporte [Schaumburg et al., 2020a]. En consecuencia, una herramienta numérica confiable para el prototipado numérico de e-µPADs se volvió crucial pero fuertemente ligada a la aplicabilidad de estos modelos matemáticos [Rosenfeld and Bercovici, 2019].

Sólo se han reportado algunos modelos analíticos de separaciones electroforéticas basadas en papel, limitados a canales unidimensionales y al transporte de un compuesto químico único [Rosenfeld and Bercovici, 2014, 2018], o la unión de un analito enfocado en ITP a la zona de reacción [Moghadam et al., 2015] en LFA. Con respecto a aspectos más fundamentales, la dispersión mecánica producida por la red de fibras fue modelada y validada experimentalmente [Urteaga et al., 2018]. Otros autores derivaron descripciones metodológicas para el flujo de fluidos [Scales and Tait, 2006, Di Fraia et al., 2018], o transporte de especies químicas [Shapiro and Probstein, 1993] en materiales porosos. Recientemente, se presentó un modelo integral que recopila todos estos resultados, pero también describe un nuevo efecto llamado dispersión mecánica de solutos impulsada electroforéticamente (EDMSD), y se validó contra resultados de la literatura. Este mo-

delo ofreció la primera descripción integral de los diferentes fenómenos y su acoplamiento para medios porosos/tortuosos, como sustratos de papel [Schaumburg et al., 2020a]. Basado en este modelo matemático reciente, por primera vez es posible un modelado numérico completo de e-µPADs. En esta tesis, se presenta una herramienta numérica de código abierto con soporte completo para simulaciones numéricas de e-µPADs, basado en el modelo mencionado anteriormente [Schaumburg et al., 2020a]. Este es el primer software capaz de producir este tipo de simulaciones numéricas, con validación experimental y gran eficiencia marcada por su rendimiento computacional tanto para ejecuciones secuenciales como en paralelo.

Este conjunto de herramientas numéricas de código abierto se construye sobre el software existente `electroMicroTransport` [Márquez Damián et al., 2019], que conserva todas sus características originales para simular separaciones electroforéticas basadas en capilares y microchips, pero agrega soporte completo para el prototipado numérico de e-µPADs. El conjunto de herramientas numéricas de `electroMicroTransport` se basa en la plataforma OpenFOAM (*Open-source Field Operation and Manipulation*), un proyecto de código abierto gratuito para la solución de problemas multifísicos basado en el método de volumen finito (FVM) [Jasak, 1996, Weller et al., 1998]. OpenFOAM se desarrolla en el lenguaje de programación multiparadigma C++, y la plataforma proporciona características clave como soporte nativo para dominios 3D, compatibilidad automática con cálculos paralelos (que pueden escalar hasta la supercomputación), una sintaxis de programación para la definición de ecuaciones diferenciales parciales que se asemeja a sus expresiones matemáticas, y la disponibilidad de código fuente bajo una licencia GNU GPL. Esta última propiedad ha llevado a su comunidad a participar en esfuerzos colaborativos para ampliar y mejorar el software con nuevos modelos (como es el caso de este trabajo) así como enfoques numéricos más eficientes [Weller et al., 1998].

Además del nuevo soporte completo para el prototipado numérico de e-µPADs, esta extensión de `electroMicroTransport` también ofrece nuevas características globales como una base de datos completa de electrólitos basada en el trabajo del Prof. Hirokawa [Hirokawa et al., 1983] (en sí tomada del software Simul [Hruška et al., 2006]), un nuevo algoritmo para el control constante de la corriente eléctrica en dominios 2D y 3D, y una opción de instalación de Docker que permite que `electroMicroTransport` se ejecute en cualquier computadora independientemente de su sistema operativo [Merkel et al., 2014]. En las siguientes secciones, se presenta una versión condensada del modelo matemático, seguida de una descripción de las contribuciones científicas de `electroMicroTransport`. Finalmente, se presentan ejemplos de aplicaciones basadas en EMUPADs con una discusión de sus resultados.

1.2.4. Flujo y transporte reactivo en medios porosos no saturados

Como ya se mencionó en este capítulo, la microfluídica basada en papel es hoy en día un campo de investigación y desarrollo bien establecido; sin embargo, el número de aplicaciones para usuarios finales sigue siendo ciertamente limitado [Anushka et al., 2023]. El éxito de los LFA, desarrollados inicialmente para tests de embarazo, y más recientemente, ampliamente difundidos con las pruebas rápidas para la detección del SARS-CoV-2 [Toft et al., 2023], no pudo ser replicado por ningún otro dispositivo analítico microfluídico basado en papel (µPAD) [Wang et al., 2023]. A pesar de los enormes esfuerzos realizados por la comunidad científica para desarrollar µPADs que cumplan con los criterios REASSURED propuestos por la Organización Mundial de la Salud (OMS) [Mabey et al., 2004], en la actualidad sólo hay unos pocos ejemplos disponibles para los usuarios finales [Schaumburg et al., 2022]. Muchos enfoques han fallado en cumplir simultáneamente con todos los criterios REASSURED principalmente debido a un alto nivel de dependencia de equipos adicionales para tareas específicas y complementarias como calentamiento, conducción de fluidos, accionamiento de válvulas, incubación y reacciones, entre otras [Aguiar et al., 2023]. Incluir estas tareas dentro de la funcionalidad de los µPADs requiere aumentar la complejidad de los dispositivos con los consiguientes desafíos en los procesos de diseño y fabricación.

Sin embargo, las perspectiva es optimista ya que muchos investigadores tanto en el ámbito académico como en empresas están trabajando actualmente en mejorar diferentes aspectos de los µPADs en diagnóstico médico, monitoreo ambiental y control de calidad de alimentos, entre otros campos, para realizar tareas más complejas al tiempo que son más robustos, portátiles y eficientes [Sharma et al., 2023]. Por ejemplo, para mejorar la robustez y portabilidad, hay nuevos desarrollos en términos de técnicas de fabricación y la integración con la telefonía móvil [Schaumburg et al., 2022, Abou El-Nour et al., 2023]. Simultáneamente, para mejorar la sensibilidad y especificidad, se están probando nuevas técnicas de detección acopladas con las clásicas colorimétricas y electroquímicas [Silva-Neto et al., 2023, Macagno et al., 2023]. Además, al mejorar los mecanismos de transporte y reacción, los límites de detección de los analitos de interés pueden aumentar significativamente [Hamidon et al., 2021].

El proceso mencionado anteriormente de optimización del transporte de fluidos y solutos, así como de las tasas de reacción, implica la caracterización sistemática de diferentes sustratos [Franck et al., 2021], así como el modelado analítico y numérico de los diferentes fenómenos involucrados [Gerlero et al., 2021b]. El éxito de estas tareas permitirá diseños innovadores que superen las limitaciones actuales de los µPADs. Desafortunadamente, la cantidad, complejidad y fuerte interdependencia de los diferentes fenómenos fisicoquímicos que determinan el rendimiento de un µPAD en particular, convierte la producción de modelos µPAD con capacidades de predicción precisas en

una tarea extremadamente desafiante [Modha et al., 2021]. Los fenómenos involucrados incluyen: (i) flujo no saturado de fluidos regidos por fuerzas capilares, (ii) transporte de múltiples especies de soluto, incluyendo advección no saturada, dispersión anisotrópica, adsorción, y (iii) reacciones (bio)químicas, todos ellos fuertemente acoplados y altamente no lineales [Bear and Cheng, 2010].

Bajo condiciones de operación muy básicas y para geometrías simples, algunos modelos analíticos y numéricos pueden ayudar a los diseñadores a determinar tiempos de imbibición o volúmenes de reactivo [Gerlero et al., 2023, Elizalde et al., 2015, Berli and Kler, 2016]. No obstante, para el diseño y la optimización de aplicaciones más sofisticadas que involucran geometrías complejas en 2D, procedimientos de múltiples pasos, múltiples entradas de fluido, varias especies reactivas, entrega secuencial automática de fluidos o diferentes materiales porosos, es necesario contar con prototipos numéricos eficientes en lo computacional y precisos para reproducir toda la fenomenología involucrada [Yang et al., 2021].

Sin embargo, al iniciarse los trabajos de esta tesis, los desarrolladores de µPADs no tenían disponible ninguna herramienta de software capaz de simular todos los fenómenos mencionados y sus interacciones, particularmente aquellos que involucran rea*f*cciones químicas complejas [Schaumburg et al., 2018a]. En contraste, el suelo, como una instancia arquetípica de medio poroso, ha sido estudiado y modelado simultáneamente con un conjunto de ecuaciones similares a las necesarias para modelar µPADs [Ladd and Szymczak, 2021]. Una de las herramientas más poderosas en este escenario es PFLOTRAN [Lichtner et al., 2017], que es de código abierto y altamente eficiente para la computación en paralelo, pero aún no está completamente adaptado para la microfluídica basada en papel [Berthet et al., 2009]. Además, se realizaron algunos intentos de modelización numérica de µPADs con COMSOL Multiphysics; sin embargo, se informaron discrepancias significativas con los resultados experimentales para el flujo no saturado y el transporte escalar [Tirapu-Azpiroz et al., 2018].

Como parte final de esta tesis se presenta `porousMicroTransport`, un paquete novedoso que se integra con la plataforma de código abierto OpenFOAM®. En particular, `porousMicroTransport` ofrece *solvers* altamente eficientes para el flujo saturado y no saturado, incluidos los modelos clásicos de capilaridad (es decir, Brooks and Corey y Van Genuchten) así como algunos alternativos como LET; incluyendo la posibilidad para los usuarios de definir sus propios modelos. En cuanto al transporte escalar en medios porosos, se modelan varios mecanismos como advección (no) saturada, difusión browniana, dispersión mecánica y adsorción, así como una biblioteca general de reacciones químicas de orden arbitrario que permite el modelado de diferentes tipos de reacciones (bio)químicas.

1.3. Organización de la tesis

El texto principal de la tesis está organizado en cuatro capítulos, con los siguientes contenidos:

- En el presente capítulo se realizó introducción a la temática y se describió la motivación y los objetivos a abordar en esta tesis.
- En el Capítulo 2 se presentará la metodología seguida para la resolución de los problemas.
- En el Capítulo 3 se hará un resumen de los resultados obtenidos para cada uno de los objetivos específicos propuestos.
- Finalmente, en el Capítulo 4, se darán las conclusiones generales y se discutirán potenciales trabajos futuros relacionados con los resultados de la tesis.

Capítulo 2

Metodología

Los problemas de flujo y transporte en medios porosos se abordaron desde el marco teórico de la mecánica del continuo. La descripción cuantitativa del transporte de uno o más fluidos con especies químicas diluidas dentro de una matriz porosa se realiza a partir de los principios físicos de conservación de cantidad de movimiento, energía, materia y carga eléctrica. Para el caso específico del movimiento de los fluidos en un medio permeable, las leyes de conservación se pueden aplicar a nivel de un volumen elemental representativo (REV) para obtener una o más ecuaciones diferenciales en la forma de generalizaciones de la Ley de Darcy [Bear and Cheng, 2010]. Por su parte, el transporte escalar se modela mediante el acople al flujo de una ecuación general de transporte para cada especie presente. Estas ecuaciones deben incorporar los fenómenos que ocurren particularmente en medios porosos, como la tortuosidad, dispersión mecánica y la adsorción. El acople normalmente es pasivo (se considera que el transporte escalar no afecta el flujo).

2.1. Flujo lateral y problemas inversos

Consideraremos inicialmente el caso arquetípico de problemas de imbibición mediante flujo lateral en un sustrato poroso de geometría rectangular inicialmente seco, a partir de un reservorio de líquido ubicado en uno de los lados. “Flujo lateral” hace referencia a que la infiltración ocurre en el plano del sustrato (es decir, en alguna dirección perpendicular a su espesor). Se ha establecido la utilidad práctica de esta configuración de flujo en dispositivos con aplicaciones clínicas y de monitoreo ambiental. Con el objeto de simplificar el modelado matemático, el medio poroso se puede tomar por infinito en la dirección de flujo, y el reservorio se considera inagotable y se modela con una condición de borde.

Un primer prototipo matemático para estos problemas se puede obtener aplicando la ley de Darcy [Bear and Cheng, 2010]:

$$\mathbf{u} = -\frac{k}{\mu}\left[\nabla p + \rho g \nabla z\right] \tag{2.1}$$

La ley de Darcy establece una relación lineal entre la velocidad de flujo macroscópica $\mathbf{u}$ y el gradiente de presión generalizada $\nabla p + \rho g \nabla z$, con el factor de proporcionalidad determinado por la permeabilidad k del material poroso (unidades de área) y la viscosidad μ del fluido. En el segundo término, ρ es la densidad del fluido, g la magnitud la aceleración de la gravedad, y z la elevación. La ley de Darcy expresada como en (2.1) sólo es válida para modelar flujo en un medio completamente saturado. Para adaptarla entonces a estos casos de flujo lateral, se podría suponer que existe un frente abrupto de mojado entre una porción del papel aún sin mojar y una porción totalmente mojada, y aplicar la ley de Darcy sobre esta última para obtener una expresión para la posición x del frente de avance durante la imbibición. Asumimos que el sustrato aún no mojado puede ejercer una presión capilar de succión p_c ($p_c < 0$), lo cual permite aproximar ∇p_x de manera uniforme en la porción saturada como p_c/x y arribar a la expresión:

$$x = u_x t = \sqrt{-\frac{k}{\mu} p_c t} = \sqrt{D_0 t} \tag{2.2}$$

En (2.2) se observa la relación $x \propto \sqrt{t}$ típica de los fenómenos de capilaridad: la expresión es análoga a aquella que predice el llenado de un tubo capilar. Si no se conocen k, p_c y μ, se puede determinar D_0 directamente de manera experimental [Elizalde et al., 2016]. Las principales desventajas de este método son dos. En primer lugar, la hipótesis del frente de mojado en flujo capilar como un escalón discontinuo puede no ser aproximación útil en todos los casos, e ignora la forma real del frente de mojado y el campo de velocidades $\mathbf{u}$ durante la imbibición en flujo lateral. Por otro lado, el modelo expresado como (2.2) sólo es válido en presencia de la geometría y condiciones mencionadas. Si bien se ha logrado extender matemáticamente este modelo a ciertas otras formas geométricas con hipótesis similares [Elizalde et al., 2015], en problemas generales con geometrías arbitrarias, este método no es apto para modelar el flujo.

Para modelar el flujo en general, recurrimos a una generalización de la ley de Darcy para condiciones no saturadas. El modelo conocido como de Darcy–Buckingham [Bear and Cheng, 2010] adopta la misma expresión de (2.1) pero admite dos relaciones constitutivas; una de las cuales define la fracción volumétrica de líquido θ como función escalar continua de la presión—valores negativos de presión representan la presión capilar del material no saturado—, y otra que relaciona estas cantidades con una permeabilidad efectiva que ya no es constante. Estas relaciones constitutivas no lineales son definidas por modelos de flujo no saturado, que llevan parámetros cuyos valores dependen de cada medio poroso y fluido circulante. Si al modelo de Darcy–Buckingham se impone además la condición de continuidad $\partial\theta/\partial t = -\nabla \cdot \mathbf{u}$, se llega a la ecuación de Richards

para flujo no saturado en medios porosos [Bear and Cheng, 2010]:

$$C(h)\frac{\partial h}{\partial t} - \nabla \cdot [K(h)\nabla (h+z)] = 0 \tag{2.3}$$

En (2.3), la incógnita es la presión expresada como la altura equivalente de columna de líquido h—igual a $p/(\rho g)$—, la capacidad hidráulica C se define como $C(h) = d\theta/dh$, la permeabilidad efectiva se reemplazó por la función de conductividad hidráulica K (unidades de velocidad).

En sustratos de la microfluídica en papel, los gradientes de presión capilar que se han observado son mucho más significativos que los cambios de elevación en cualquier dispositivo (es decir, $|\nabla z| \ll |\nabla h|$), lo cual permite despreciar el efecto de la gravedad incluso cuando el flujo no es estrictamente horizontal [Schaumburg et al., 2018a], y utilizar directamente:

$$C(h)\frac{\partial h}{\partial t} - \nabla \cdot [K(h)\nabla h] = 0 \tag{2.4}$$

Esta expresión se conoce como la ecuación de Richards "horizontal". Cuando el campo de presiones no es de interés, (2.4) se puede reescribir con la fracción θ como incógnita en forma de ecuación de difusión no lineal tomando $D = K/C$ [Bear and Cheng, 2010]:

$$\frac{\partial \theta}{\partial t} - \nabla \cdot [D(\theta)\nabla \theta] = 0 \tag{2.5}$$

La ventaja de (2.5)—así como de (2.3) y (2.4)—es que son aplicables a problemas en geometrías y con condiciones iniciales y de borde arbitrarias. Para el caso particular de imbibición en un medio rectangular, la definición de un problema matemático de valor inicial y de borde usando (2.5) es:

$$\begin{cases} \dfrac{\partial \theta}{\partial t} = \dfrac{\partial}{\partial x}\left(D(\theta)\dfrac{\partial \theta}{\partial x}\right) & x, t > 0 \\ \theta = \theta_i & t = 0, x > 0 \\ \theta = \theta_s & x = 0, t > 0 \end{cases} \tag{2.6}$$

donde θ_i es la condición inicial (fracción de líquido presente en el papel en condiciones ambientales) y θ_s es igual a la porosidad del medio.

El mayor desafío para el modelado matemático de flujo no saturado usando estas ecuaciones es el de obtener las funciones necesarias (D, o K y C) para los sistemas que se quieren modelar. En el Apartado 2.2, se presentarán distintos modelos de flujo no saturado que proponen expresiones para estas funciones.

Si bien algunos de esos modelos poseen parámetros que se podrían ajustar a ciertos experimentos, estos modelos tienen orígenes en otras aplicaciones, y por lo tanto para su uso en microfluídica

resulta crucial tener herramientas para resolver problemas inversos en los que los parámetros se estiman a través de observaciones de flujo en configuraciones simples, como en flujo lateral.

Los problemas de flujo lateral de (B.2) son susceptibles a la transformación de Boltzmann [Gerlero et al., 2023]. A continuación, mostraremos una forma general de la transformación de Boltzmann aplicable a ciertos problemas regidos por (2.5) y (2.4)—entre los que se incluyen los casos de flujo lateral que hemos considerado—, y presentaremos una estrategia y herramienta de software para resolverlos de manera numérica.

Para aplicar la transformación de Boltzmann, nos restringimos a la ecuación de difusión no lineal (2.5) contemplando un único eje **r**:

$$\frac{\partial \theta}{\partial t} = \frac{1}{r^{m-1}} \frac{\partial}{\partial r} \left(r^{m-1} D(\theta) \frac{\partial \theta}{\partial r} \right) \quad m = 1, 2, 3 \tag{2.7}$$

y, de manera análoga, a la ecuación de Richards horizontal (2.4) también en un eje **r**:

$$C(h) \frac{\partial h}{\partial t} = \frac{1}{r^{m-1}} \frac{\partial}{\partial r} \left(r^{m-1} K(h) \frac{\partial h}{\partial r} \right) \quad m = 1, 2, 3 \tag{2.8}$$

En (2.7) y (2.8), el valor de m determina el número de dimensiones del flujo: $m = 1$ en flujo lateral unidimensional, $m = 2$ para flujo radial en coordenadas polares o cilíndricas, y $m = 3$ para flujo radial en coordenadas esféricas.

La transformación de Boltzmann implica la definición de una nueva variable, que llamamos variable de Boltzmann y denotaremos con ϕ, como:

$$\phi = r/\sqrt{t} \tag{2.9}$$

Cabe destacar que la definición de ϕ implica una autosemejanza de las soluciones que sigue la relación $x \propto \sqrt{t}$ ya mencionada.

La transformación de Boltzmann permite reescribir las derivadas parciales de (2.7) y (2.8) usando reglas de la cadena, tal que las ecuaciones en derivadas parciales se transforman en las ecuaciones diferenciales ordinarias. En el caso de (2.7), la ecuación transformada queda como:

$$-\frac{\phi}{2} \frac{d\theta}{d\phi} = \frac{m-1}{\phi} D(\theta) \frac{d\theta}{d\phi} + D(\theta) \frac{d^2\theta}{d\phi^2} + \frac{dD}{d\theta} \left(\frac{d\theta}{d\phi} \right)^2 \tag{2.10}$$

y la transformación es análoga para (2.8).

Además de las ecuaciones, se deben poder transformar las condiciones iniciales y de borde. La transformación de una condición inicial uniforme es trivial. Para permitir la imposición de condiciones de borde en la variable de Boltzmann, definimos una constante $\phi_b = r_b/\sqrt{t}$ que determina la posición del borde r_b en un problema. Cuando $m = 1$, se puede tomar directamente

$\phi_b = 0$ para imponer la condición de borde en $r = 0$. Esto no es válido cuando $m > 1$, no obstante, $\phi_b \to 0^+$ es una aproximación útil para ciertas condiciones de borde. Teniendo esto en cuenta, es posible imponer ciertas condiciones de tipo Dirichlet, de tipo Neumann, e incluso—con $m = 1$—una condición de caudal constante [Gerlero et al., 2023].

A partir de estas transformaciones posibles a las ecuaciones y condiciones iniciales y de borde, proponemos un esquema numérico para resolver problemas de flujo compatibles con la transformación de Boltzmann.

La base del esquema es el hecho de que las soluciones a problemas de Cauchy de (2.7) y (2.8)—es decir, con condiciones de borde de tipos Dirichlet y Neumann, y sin fijar una condición inicial—se pueden resolver con integración numérica de las ecuaciones diferenciales ordinarias usando las condiciones transformadas y con un criterio de finalización de derivada nula con respecto a ϕ. Luego, sobre esta base, las soluciones a problemas con condición inicial y una condición de borde—sea ésta Dirichlet o de caudal impuesto—se pueden obtener con un método de disparos [Press et al., 2007] que implica resolver iterativamente reducciones a problemas de Cauchy en los que se varía el valor de la condición de borde "libre" hasta que la solución obtenida satisface la condición inicial. Para obtener valores de la condición libre para las iteraciones se emplea un algoritmo de búsqueda de raíz, que comienza por encontrar un intervalo que contenga la raíz deseada y finalmente se aproxima a la raíz aislada usando el método de bisección.

El esquema numérico fue implementado en la herramienta de software *Fronts*, disponible en forma de paquetes *open source* para los lenguages Python y Julia, en ambos casos usando el método ímplicito Radau IIA de orden 5 para la integración [Virtanen et al., 2020, Rackauckas and Nie, 2017] y el algoritmo de búsqueda de raíces mencionado. El uso intensivo de operaciones escalares de punto flotante para la integración favorece la implementación en Julia, donde estas operaciones tienen menor costo computacional que en Python, con el efecto de que se han alcanzado tiempos de cómputo varios órdenes de magnitud menores a los que se pueden lograr para los mismos problemas con herramientas de software que no utilizan la transformación de Boltzmann. *Fronts* acepta modelos de flujo definidos con expresiones arbitrarias, y usa diferenciación automática (Julia) o simbólica (Python) para evaluar las derivadas necesarias de las funciones de los modelos de flujo.

2.1.1. Problemas inversos

La aplicación de la transformación de Boltzmann al problema (B.2) también permite obtener directamente una expresión matemática para la difusividad en función del perfil de mojado θ–ϕ, dada por:

$$D(\theta) = -\frac{1}{2}\frac{d\phi}{d\theta}\int_{\theta_i}^{\theta}\phi d\theta \tag{2.11}$$

Éste es el método de Bruce and Klute [1956], y es una de las formas de resolver un problema inverso en el que la incógnita es la función de difusividad $D(\theta)$ que explica la dinámica de flujo. Si suponemos que el perfil observado se puede aproximar numéricamente de manera suave, la obtención de una función $D(\theta)$ es directa, pero esta última no tendrá necesariamente una expresión analítica. Comúnmente, se desea adoptar una expresión analítica paramétrica para $D(\theta)$ y hallar los valores de los parámetros que mejor aproximan el perfil observado. En estos casos, se pueden usar dos enfoques distintos: uno analítico, en el que se propone una expresión paramétrica analítica para $\phi(\theta)$ y se usa (2.11) para arribar a una función $D(\theta)$ también paramétrica—con obvias restricciones en cuanto a las funciones $D(\theta)$ que se pueden obtener—[Evangelides et al., 2010]; y otro numérico, en el que se usa el esquema de *Fronts* en un bucle de optimización para estimar los parámetros de modelos de flujo arbitrarios.

Como parte del trabajo de tesis, se realizaron ensayos de flujo en dispositivos de microfluídica, y con los perfiles observados experimentalmente se utilizó exitosamente *Fronts* en un problema inverso de estimación de parámetros de los modelos del Apartado 2.2, en búsqueda de los valores de los parámetros que mejor aproximaran las observaciones. También se reconstruyeron funciones $D(\theta)$ de resultados experimentales usando (2.11) e interpolación numérica para evaluar el comportamiento de los modelos en este dominio.

2.2. Modelos de flujo no saturado

2.2.1. Brooks y Corey

El modelo de Brooks and Corey [1964] define la siguiente correlación entre presión y fracción de líquido [Gerlero et al., 2022]:

$$\theta = \theta_r + \frac{\theta_s - \theta_r}{|\alpha h|^n} \quad h < -\frac{1}{\alpha} \tag{2.12}$$

y, para la conductividad hidráulica K:

$$K = K_s\left(\frac{1}{|\alpha h|^n}\right)^{\frac{2}{n}+l+2} \quad h < -\frac{1}{\alpha} \tag{2.13}$$

tal que la difusividad D—para (2.5)—queda:

$$D(\theta) = \frac{K}{C} = K\frac{dh}{d\theta} = \frac{K_s}{\alpha}\frac{1}{n(\theta_s - \theta_r)}\left(\frac{\theta - \theta_r}{\theta_s - \theta_r}\right)^{\frac{1}{n}+l+1} \tag{2.14}$$

Para $h \geq -1/\alpha$, $\theta = \theta_s$ y $K = K_s$. Los parámetros que se deben conocer para emplear el modelo de Brooks y Corey son K_s, α, n, l, θ_s θ_r. Cabe aclarar que θ_s debería nuevamente ser igual a la porosidad del medio. Por su parte, θ_r se conoce como la fracción de líquido residual y representa el otro límite de validez del modelo (esto es, las ecuaciones sólo se definen para θ entre θ_r y θ_s).

Remarcamos también el hecho de que K_s y α sólo aparecen en el factor constante en (2.14). Dicho de otro modo, no es posible obtener sus valores de manera independientemente en ausencia de la influencia de presiones externas o gravedad no despreciable.

2.2.2. Van Genuchten

Por su parte, el modelo de Van Genuchten [1980] propone:

$$\theta = \theta_r + \frac{\theta_s - \theta_r}{(1 + |\alpha h|^n)^m} \quad h < 0 \tag{2.15}$$

con:

$$K = K_s\Theta^l\left(1 - \left(1 - \Theta^{\frac{1}{m}}\right)^m\right)^2 \quad h < 0 \tag{2.16}$$

y ambos con $m = 1 - 1/n$ y $\Theta = (\theta - \theta_r) / (\theta_s - \theta_r)$, tal que:

$$D(\theta) = \frac{K_s}{\alpha}\frac{(1-m)}{m(\theta_s - \theta_r)}\Theta^{l-\frac{1}{m}}\left(\left(1 - \Theta^{\frac{1}{m}}\right)^{-m} + \left(1 - \Theta^{\frac{1}{m}}\right)^m - 2\right). \tag{2.17}$$

Cuando $h \geq 0, \theta = \theta_s$ y $K = K_s$. Los parámetros del modelo Van Genuchten son equivalentes a los del de Brooks y Corey, con la particularidad de que aquí el parámetro m también se puede usar en lugar de n.

2.2.3. LET

Además de las correlaciones dadas por los modelos anteriores, consideraremos también un conjunto de funciones conocidas como correlaciones LET [Lomeland, 2018]. Éstas son una serie de correlaciones paramétricas para flujo no saturado en medios porosos que incluyen tres parámetros "de forma"—L, E y T—, y se definen de tal manera que cada parámetro controla una sección distinta de las curvas resultantes.

Notamos que las expresiones LET convencionalmente involucran la saturación S_w, que se define como la fracción de agua dividida por la porosidad del material. Se puede emplear para la conductividad hidráulica una fórmula LETx, y una función LETs para relacionar la saturación y la presión capilar en imbibición espontánea [Lomeland, 2018]. Combinando ambas funciones LET, se obtiene una expresión para la difusividad [Gerlero et al., 2022]:

$$D(\theta) = \frac{K_s p_{cir}}{\rho g} \frac{E_s S_{wp}^{L_w} S_{wp}^{T_s} \left(1 - S_{wp}\right)^{L_s} \left(L_s S_{wp} - S_{wp} T_s + T_s\right)}{\theta_s S_{wp} \left(S_{wir} - 1\right) \left(S_{wp} - 1\right) \left(E_s S_{wp}^{T_s} + \left(1 - S_{wp}\right)^{L_s}\right)^2 \left(E_w \left(1 - S_{wp}\right)^{T_w} + S_{wp}^{L_w}\right)} \tag{2.18}$$

con:

$$S_{wp} = \frac{S_w - S_{wir}}{1 - S_{wir}} = \frac{\theta - \theta_s S_{wir}}{\theta_s - \theta_s S_{wir}}$$

En la expresión anterior, trasladamos los parámetros que sólo aparecen como factores constantes a la fracción más a la izquierda. Además de éstos, notamos que hay siete otros parámetros desconocidos para definir la difusividad: L_w, E_w, T_w, L_s, E_s, T_s and S_{wir}.

2.3. Flujo y transporte electroforético en medios porosos saturados

En este modelo Schaumburg et al. [2020a], se supone que el medio poroso está saturado y se modela el flujo del solvente usando las ecuaciones de Navier-Stokes adaptadas para medios porosos del tipo manojo de tubos tortuosos no constrictos:

$$\begin{aligned} \frac{\tau}{\theta_s}\frac{\partial \mathbf{u}}{\partial t} + \frac{\tau}{\theta_s}\mathbf{u}\cdot\nabla\left[\frac{\mathbf{u}}{\theta_s}\right] &= \frac{\mu}{\rho\tau}\nabla^2\left[\frac{\mathbf{u}}{\theta_s}\right] - \frac{1}{\rho\tau}\nabla p - \left[\frac{\rho_e}{\rho\tau}\nabla\Phi + \frac{\mu}{\rho}\frac{\mathbf{u}}{k}\right] H(\theta_s) \\ \nabla\cdot\mathbf{u} &= 0 \end{aligned} \tag{2.19}$$

donde τ es la tortuosidad del medio. H es una función escalón de Heaviside hacia la izquierda centrada en $\theta_s = 1$, que en efecto habilita los últimos términos de (2.19) sólo cuando se aplica en un medio poroso, y permite por lo tanto usar las mismas ecuaciones para modelar flujo y transporte electroforético en canales abiertos. ρ_e es la densidad de carga promediada que produce un flujo eléctroosmótico efectivo. El modelo que se adopta en papel para ρ_e es:

$$\rho_e^p = \frac{\theta_s \epsilon \zeta}{\tau k} \tag{2.20}$$

donde ζ es un potencial electrocinético equivalente de las fibras, y ϵ es la permitividad eléctrica del fluido.

Luego, se pueden definir ecuaciones de transporte para los electrolitos presentes en la solución:

$$\frac{\partial(\theta_s c^i)}{\partial t} = -\nabla \cdot \left[\left[\frac{\mathbf{u}}{\theta_s} + \frac{\Omega_i}{\tau^2} \nabla \Phi \right] \theta_s c^i - \left(\frac{D_M^i}{\tau^2} s \left| \frac{\mathbf{u}}{\theta_s} \right| + s_e \left| \frac{\Omega^i}{\tau^2} \nabla \Phi \right| \right) \nabla \left(\theta_s c^i \right) \right] \tag{2.21}$$

donde c^i es la concentración del electrolito i, Ω_i es su movilidad electroforética, D_M^i es su difusividad molecular, s es un coeficiente de dispersión mecánica, s_e es una dispersividad del medio por la dispersión mecánica de índole electroforética del soluto—dispersión que ocurre en el campo de concentraciones de una especie iónica cuando se aplica un campo eléctrico—. La ecuación (E.3) se acopla a una ecuación de conservación de carga para determinar el campo de potencial eléctrico Φ, que a su vez requiere el cómputo de la conductividad eléctrica, en el que aparecen las movilidades, números de carga y concentraciones de los electrolitos [Gerlero et al., 2021b].

2.4. Flujo y transporte reactivo en medios porosos no saturados

El modelado del flujo no saturado en geometrías arbitrarias se puede conseguir resolviendo las ecuaciones presentadas en la secciones 2.1 y 2.2. Resolviendo estas ecuaciones, se puede conocer el campo de fracción de líquido θ (ya sea directamente o como función de las presiones). El campo de velocidad macroscópica $\mathbf{u}$ se puede reconstruir como:

$$\mathbf{u} = -K(h)\nabla h = -D(\theta)\nabla\theta \tag{2.22}$$

Para modelar el transporte reactivo, se parte de una ecuación de transporte por advección–difusión–dispersión similar a (E.3), a la que se agregan los términos de reacciones y dispersión anisotrópica—no contemplada en (E.3)—. Una expresión posible es [Bear and Cheng, 2010]:

$$\frac{\partial \left({R_d}^i \theta c^i \right)}{\partial t} = -\nabla \cdot \left[\mathbf{u} \theta c^i - \left\{ \left(\frac{D_M^i}{\tau^2} + s_T^i \left| \frac{\mathbf{u}}{\theta_s} \right| \right) \boldsymbol{I} + \left(s_L^i - s_T^i \right) \frac{\mathbf{u}\mathbf{u}}{\theta_s |\mathbf{u}|} \right\} \theta \nabla c^i \right] + \theta F^i \tag{2.23}$$

con una dispersividad en dirección transversal al flujo s_T^i y otra en la dirección del flujo s_L^i. $\boldsymbol{I}$ es el tensor identidad. F^i representa uno o más términos de reacción asociados a la especie i, y ${R_d}^i$ es un factor de retardo que cuantifica la resistencia al movimiento de la especie disuelta por la adsorción parcial y reversible a la matriz porosa, explicada en papel por efectos cromatográficos y definida como:

$$R_d{}^i = 1 + \frac{\rho_s \left(1 - \varepsilon_{\text{tot}}\right) K_d{}^i}{\theta} \tag{2.24}$$

donde ρ_s es la densidad del material sólido, ε_{tot} la porosidad total, y $K_d{}^i$ es un coeficiente de particionamiento para la adsorción.

2.5. Software

Si bien se decidió trabajar dentro marco teórico general de la mecánica del continuo, los problemas abordados tienen sus particularidades dimensionales. Por esta razón, se han desarrollado diferentes herramientas de software. *Fronts*, con variantes programadas en los lenguajes Python y Julia, se especializa en problemas de flujo lateral unidimensional, con una implementación muy eficiente específica para la resolución de este tipo de problemas. Por su parte, `electroMicroTransport` y `porousMicroTransport` tienen implementaciones basadas en en el método de volúmenes finitos, y han sido programadas mayormente en el lenguaje C++ sobre la plataforma OpenFOAM [Jasak, 1996, Weller et al., 1998].

2.5.1. Disponibilidad de las herramientas desarrolladas

- *Fronts* (bajo licencias MIT y BSD):
  - `https://github.com/gerlero/Fronts.jl` (Julia)
  - `https://github.com/gerlero/fronts` (Python)
- `electroMicroTransport` (bajo licencia GPLv3):
  - `https://gitlab.com/santiagomarquezd/electroMicroTransport`
- `porousMicroTransport` (bajo licencia GPLv3):
  - `https://github.com/gerlero/porousMicroTransport`

Capítulo 3

Resultados principales

En este capítulo, se muestran resultados destacados relacionados con cada uno de los objetivos específicos de la tesis. Para conocer la metodología propia de cada trabajo y el análisis completo de los resultados, se refiere a los lectores al material original de cada trabajo disponible en los anexos de este documento.

3.1. Flujo lateral y problemas inversos

Se logró el desarrollo de *Fronts*, un conjunto de paquetes de software numéricos para resolver problemas de difusión no lineal, particularmente en flujo lateral en medios porosos. El software utiliza la transformación de Boltzmann para resolver este tipo de problemas en geometrías semi-infinitas de manera precisa y eficiente (Figura 3.1). Para más detalles, referirse al trabajo incluido como Anexo A.

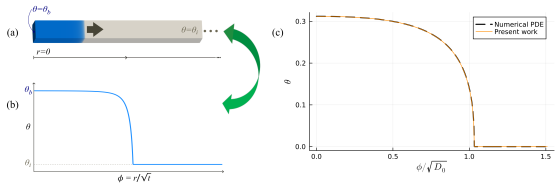

Figura 3.1: (a) Problema de valor inicial y de borde en un dominio rectangular semi-infinito compatible con la transformación de Boltzmann y *Fronts*. (b) Transformación de la solución a la variable de Boltzmann. (c) Resultados de un ejemplo de aplicación.

3.2. Modelos de flujo no saturado

El estudio de modelos de flujo no saturado hizo uso de *Fronts* para obtener parámetros para los diferentes modelos mencionados (modelos pre-existentes y el modelo LETd propio). Inicialmente, se obtuvieron datos experimentales propios con la configuración de la Figura 3.2. El procesamiento de datos permitió obtener las curvas de la Figura 3.2. Luego, se invocó a *Fronts* en un problema de optimización para obtener los mejores parámetros de ajuste de cada modelo propuesto, los cuales se encuentran volcados en la Tabla 3.1. Los mejores ajustes fueron comparados con el perfil experimental (Figura A.5) y con la difusividad reconstruida de los experimentos (Figura 3.5).

Para más información sobre el procedimiento y los resultados obtenidos, se sugiere la lectura de las secciones correspondientes del Anexo B.

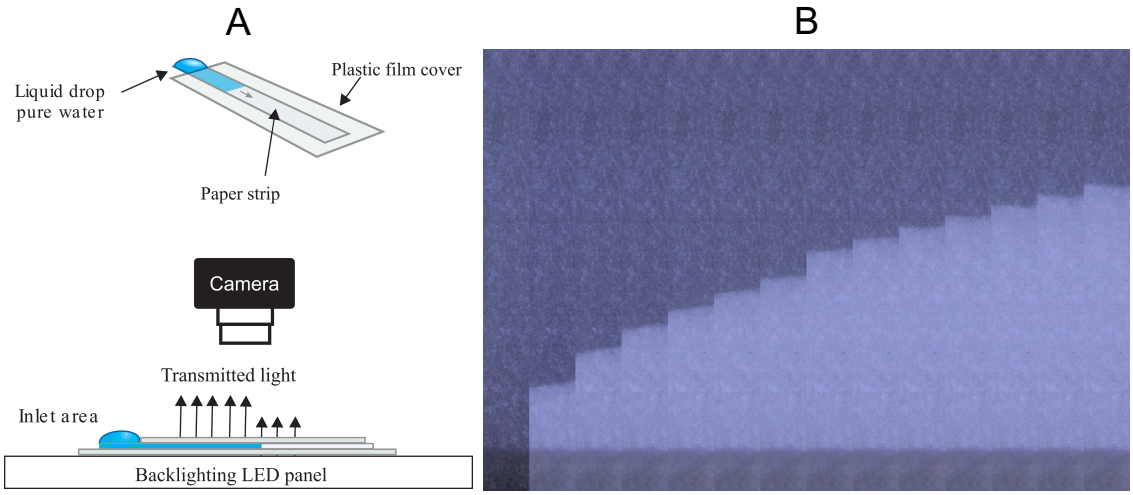

Figura 3.2: (a) Diagrama de los dispositivos de papel y configuración experimental para los experimentos de flujo lateral. (b) Secuencia de imagenes capturadas durante la imbibición de un único dispositivo (imágenes recortadas en ancho).

3.3. Flujo y transporte electroforético en medios porosos saturados

El trabajo en flujo y transporte electroforético derivó en el desarrollo de una nueva versión de la herramienta `electroMicroTransport` [Gerlero et al., 2021a] con soporte para separaciones electroforéticas en medios porosos. Junto con la herramienta, se generaron y se incluyen casos de ejemplo de electroforesis de zona en papel (PZE), electroforesis de frontera móvil (MBE) en papel, e isoelectroenfoque de flujo libre (FFIEF) en papel. Los resultados de estos ejemplos de aplicación

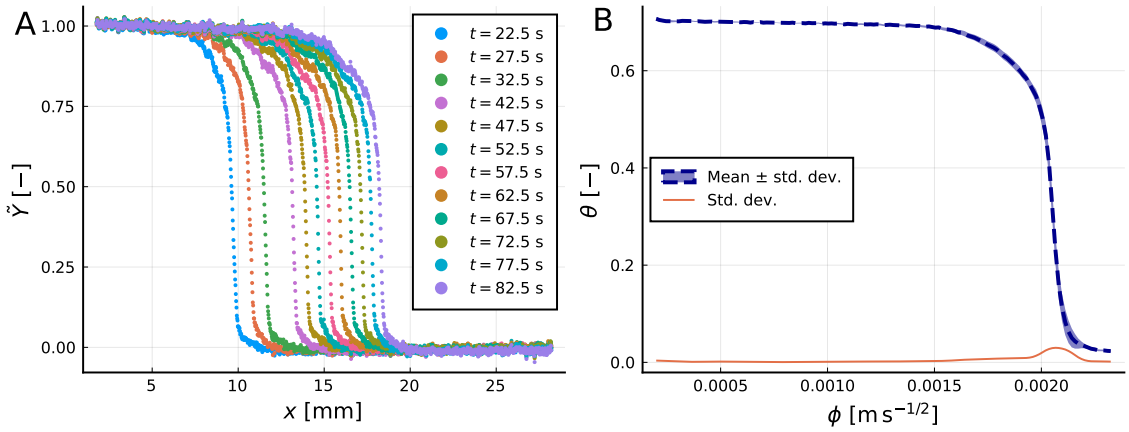

Figura 3.3: (a) Resultados intermedios del procesamiento de datos en un único dispositivo de papel. (b) Resultados finales de procesamiento de datos (contenido de humedad promedio y desvío estándar, versus la variable de Boltzmann). Los bajos valores de desvío estándar son consecuencia de la autosemejanza de los perfiles capturados a tiempos distintos.

se muestran en las Figura 3.6 a Figura 3.8 respectivamente.

Para conocer los detalles, se recomienda referirse a los trabajos originales en los Anexos D y E

3.4. Flujo y transporte reactivo en medios porosos no saturados

El estudio de flujo y transporte reactivo en medios porosos no saturados culminón con el desarrollo de la herramienta se simulación `porousMicroTransport`. Junto con la herramienta, se presentaron dos casos de aplicación en µPADs basados en dispositivos presentados en la literatura. El primer caso consiste en la simulación de un dispositivo de tipo mezclador de Hamidon et al. [2021], en el que se produce una reacción química entre dos especies que ingresan por dos entradas separadas (Figura 3.9).

Para el segundo ejemplo de aplicación, se decidió realizar una simulación completa de un caso paradigmático de µPAD: un dispositivo para la detección de malaria. El dispositivo, de funcionamiento por “entrega secuencial” (Figura 3.9), había sido objeto de estudio en la literatura [Fu et al., 2012, Rath and Toley, 2021], pero nunca había sido simulado de manera comprehensiva y acoplada incluyendo el flujo capilar, efectos dispersivos en papel, y las reacciones químicas que ocurren, para finalmente predecir la lectura de salida del dispositivo. Los resultados de este caso se muestran en la Figura 3.11.

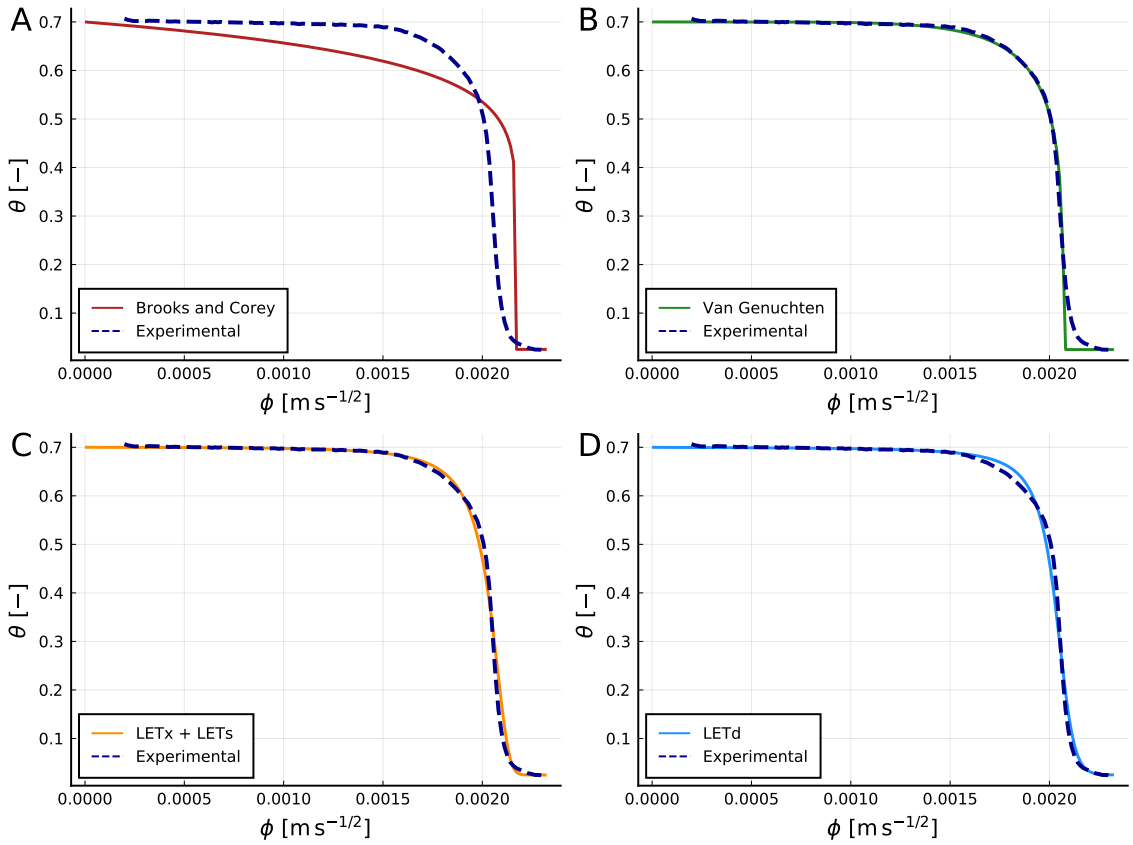

Figura 3.4: Mejores ajustes de los perfiles imbibición versus la variable de Boltzmann para los diferentes modelos considerados.

Los detalles de implementación y de los casos de ejemplo se pueden hallar en el trabajo correspondiente en el Anexo E.

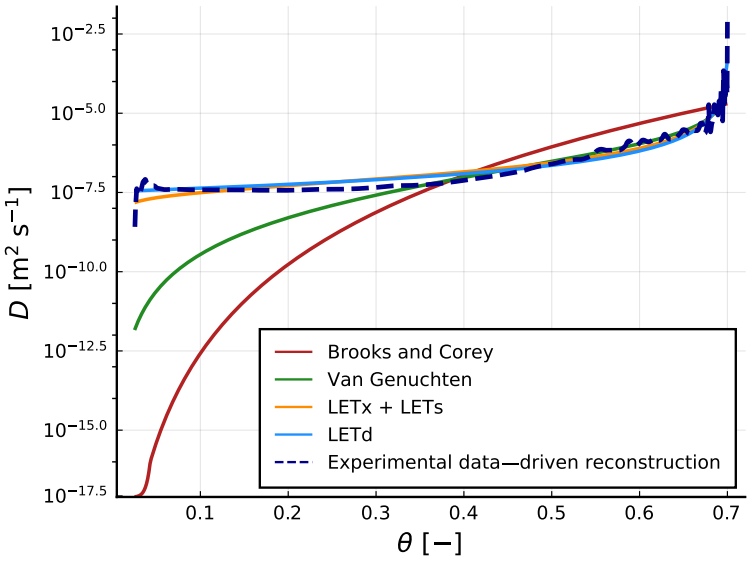

Figura 3.5: Comparación de la función $D(\theta)$ reconstruida experimentalmente y las difusividades de los diferentes modelos con los mejores parámetros de ajuste.

Tabla 3.1: Resultados finales de la estimación de parámetros usando *Fronts* y los datos experimentales.

Modelo	Parámetros		χ^2_ν
Brooks y Corey	n	0,2837	691
	l	4,795	
	θ_r	$2{,}378 \times 10^{-5}$	
	K_s/α	$3{,}983 \times 10^{-6}\,\mathrm{m^2\,s^{-1}}$	
Van Genuchten	n	8,093	1,7
	l	2,344	
	θ_r	0,004 943	
	K_s/α	$2{,}079 \times 10^{-6}\,\mathrm{m^2\,s^{-1}}$	
LETx + LETs	L_w	1,651	1,0
	E_w	230,5	
	T_w	0,9115	
	L_s	0,517	
	E_s	493,6	
	T_s	0,3806	
	S_{wir}	0,016 80	
	$K_s P_{cir}/\gamma$	$8{,}900 \times 10^{-3}\,\mathrm{m^2\,s^{-1}}$	
LETd	L	0,004 569	1,5
	E	12 930	
	T	1,505	
	S_{wir}	0,028 36	
	D_{wt}	$4{,}660 \times 10^{-4}\,\mathrm{m^2\,s^{-1}}$	

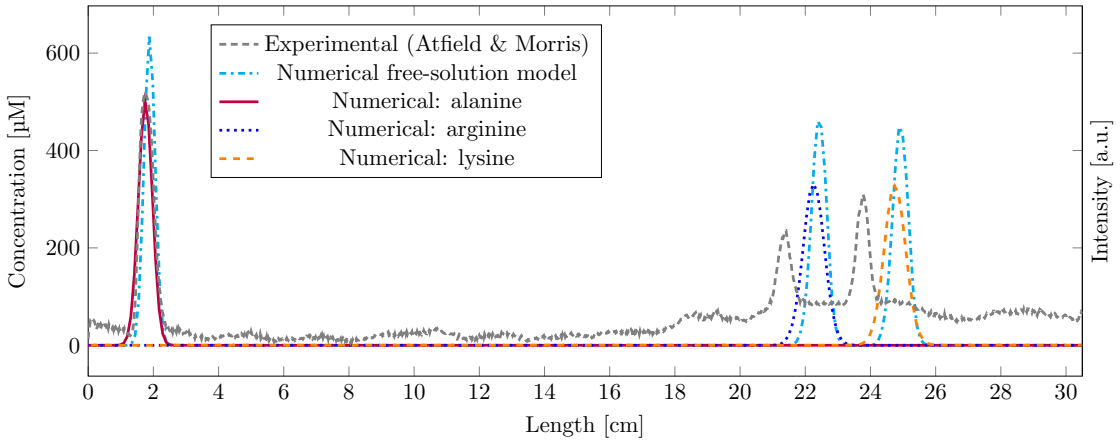

A

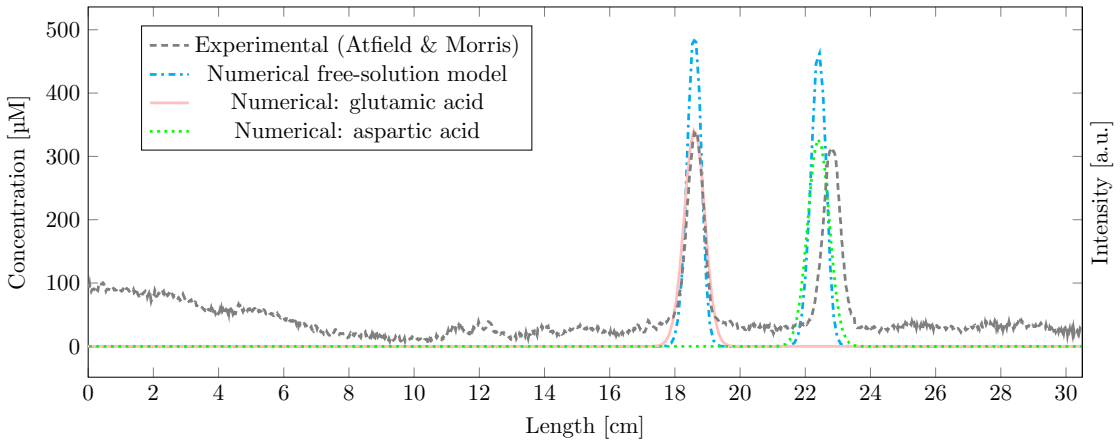

B

Figura 3.6: Ejemplos de aplicación `paperBasedZE1` (a), y `paperBasedZE2` (b) de `electroMicroTransport`. Comparación de concentraciones de aminoácidos experimentales, de solución libre y numéricas medidas longitudinalmente en el sustrato tras de 200 minutos.

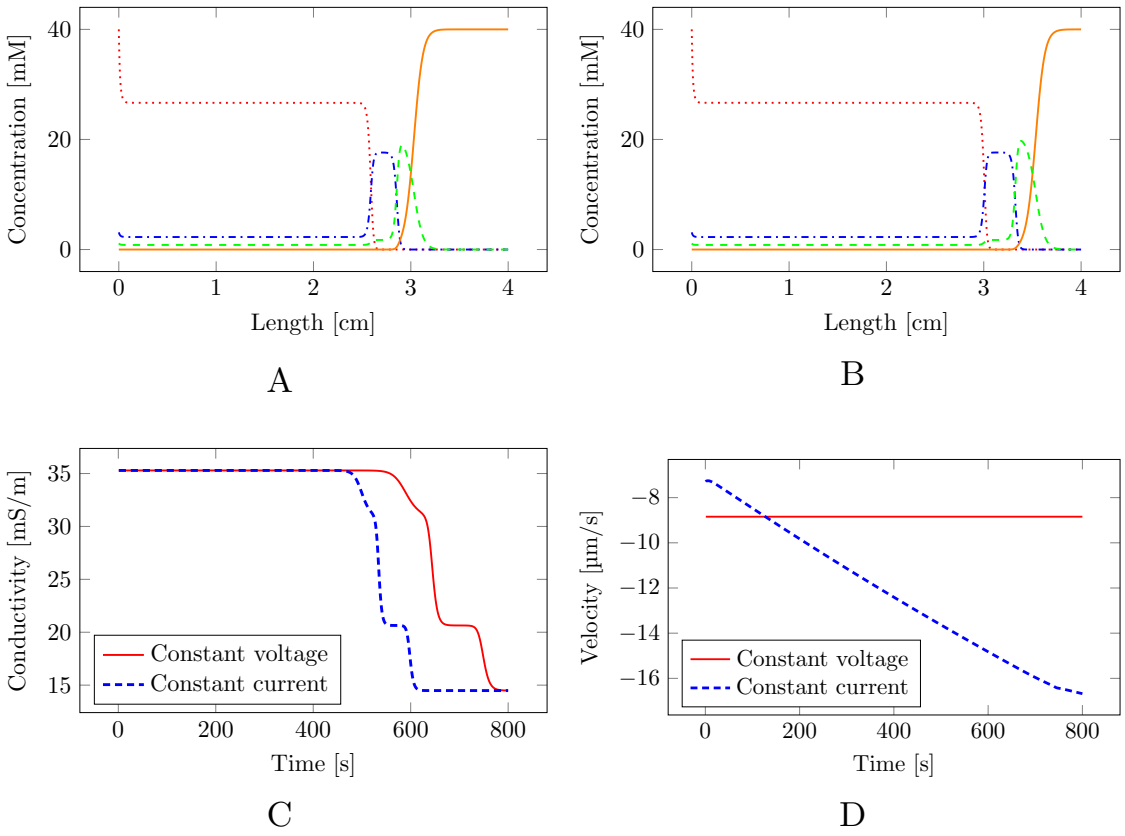

Figura 3.7: Perfiles de concentración de ácido clorhídrico (línea anaranjada sólida), ácido acético (línea puntuada roja), ácido cítrico (línea azul punto y raya) y ácido oxálico (línea rayada verde), luego de 600 s bajo condictiones de voltaje constante (a) y corriente constante (b). (c) Señales de conductividad teórica equivalente medidas en el tiempo por un detector simulado ubicado a 30 mm de la entrada. (d). Velocidades de flujo del fluido por flujo electroosmótico como función del tiempo.

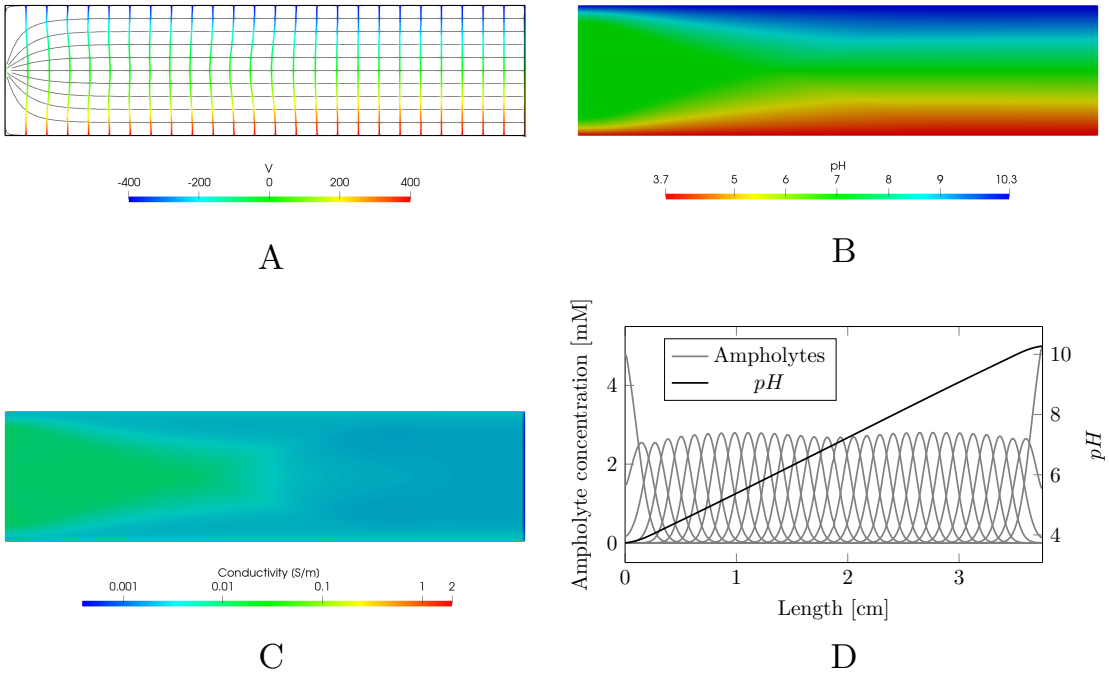

Figura 3.8: Resultados del caso de isoelectroenfoque de flujo libre tras 15 min de simulación. (a) Líneas de flujo de fluido (azul) y de campo eléctrico (color según el potencial eléctrico local). (b) Distribución de pH en la cámara de separación. (c). Distribución de conductividad eléctrica en la cámara de separación. (d) Concentraciones de anfolitos y distribución de pH a lo largo de la sección de salida de la cámara de separación. En (a), (b) y (c), la entrada está a la izquierda y la salida a la derecha de los dominios rectangulares.

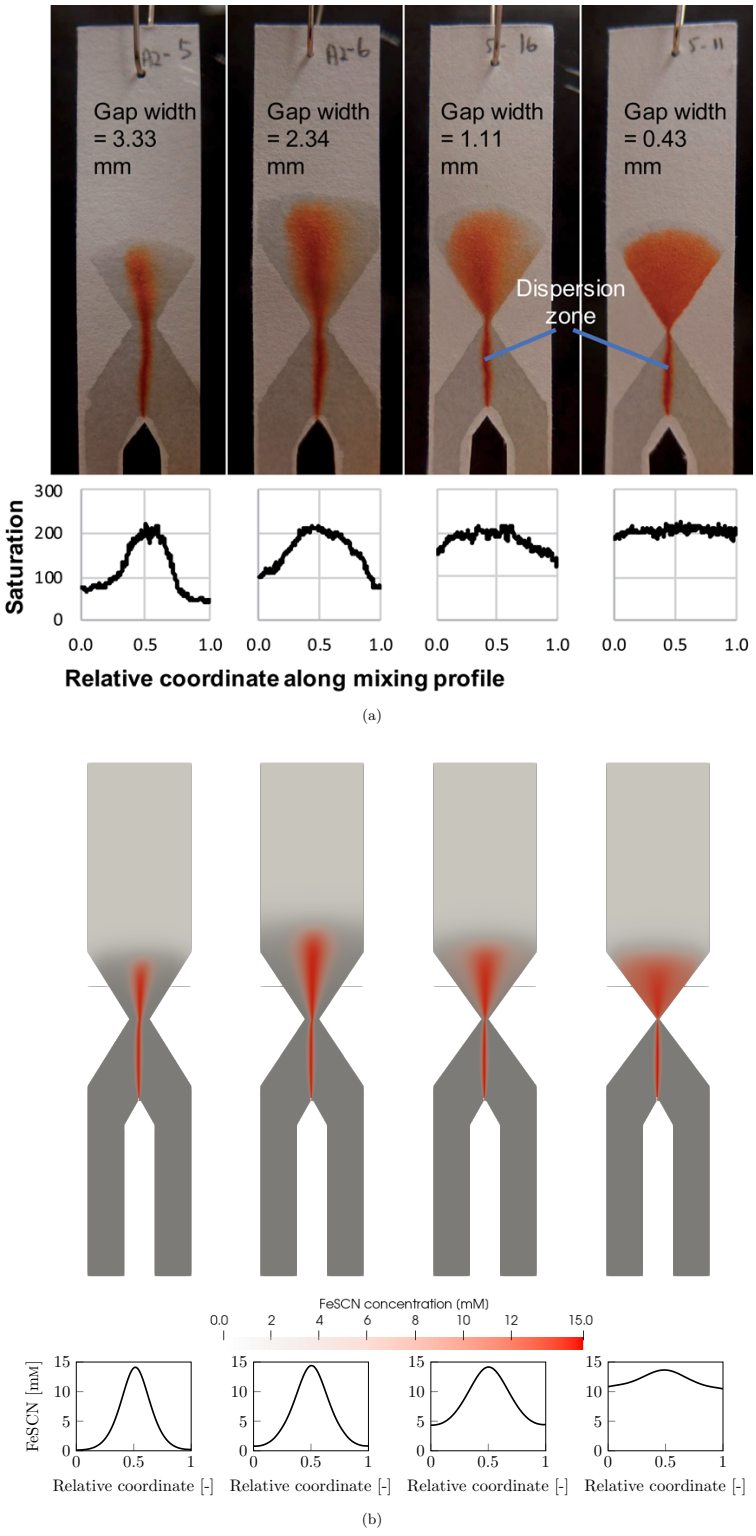

Figura 3.9: (a) Resultados experimentales de Hamidon et al. [2021]; panel superior, imágenes de los cuatro dispositivos probados; panel inferior, distribución del producto de reacción en la zona de mezclado. Adaptada bajo la licencia Creative Commons Attribution 3.0 Unported. (b) Resultados numéricos obtenidos en este trabajo; panel superior, imágenes de las cuatro geometrías; panel inferior, distribución del producto de reacción en la zona de mezclado (línea horizontal). El campo gris indica saturación de fluido.

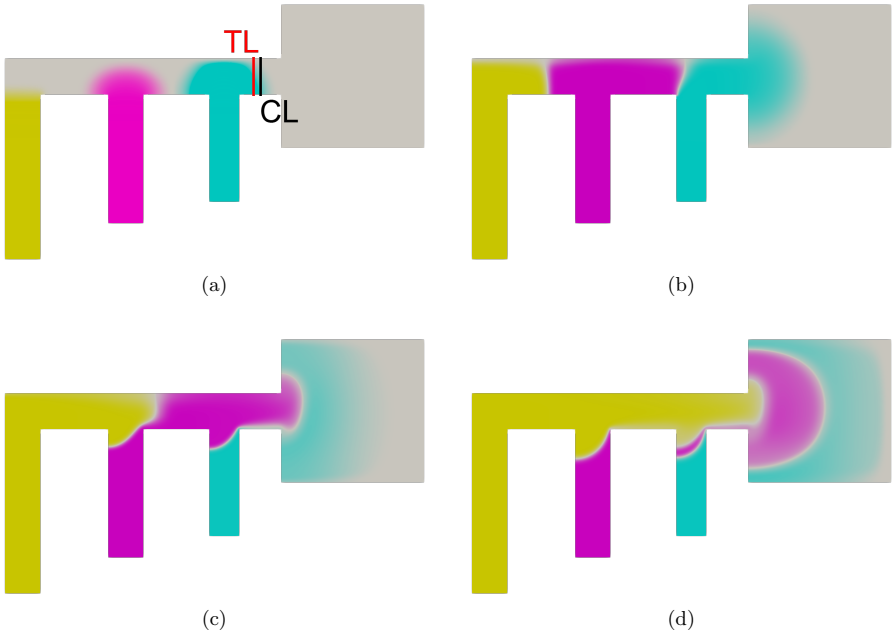

Figura 3.10: Secuencia de entrega automática. (a) Inicio de la secuencia, con las ubicaciones de las líneas de test (TL) y control (CL) resaltadas. (b) El primer soluto pasa por las líneas de test y control. (c) El segundo soluto pasa por las líneas de test y control. (c) Arribo del soluto final.

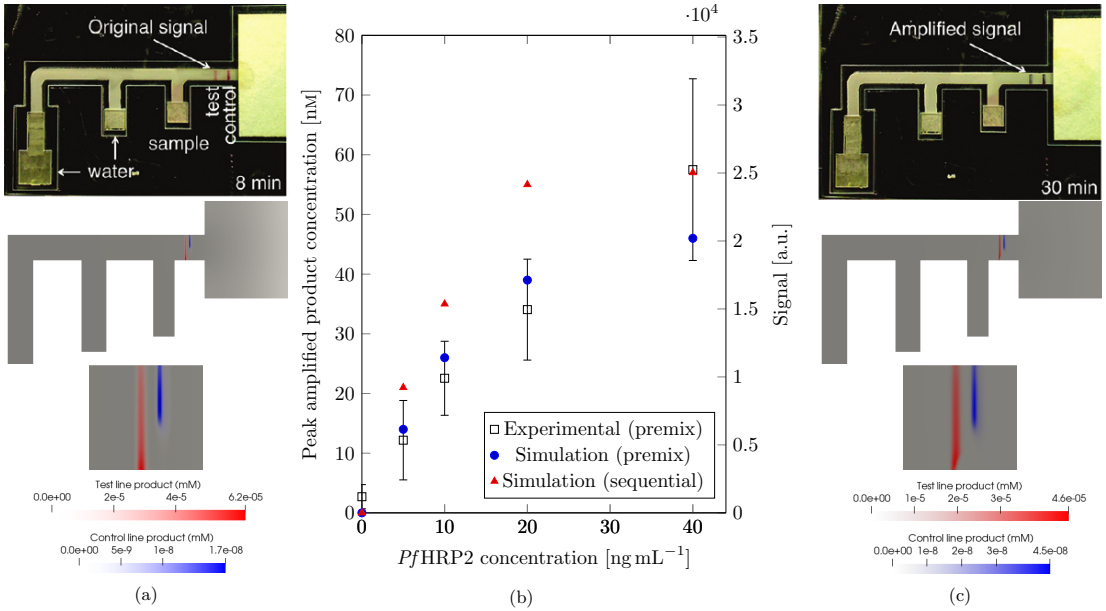

Figura 3.11: (a) y (c) Visualización de resultados sin amplificar y amplificados (respectivamente) para una concentración de analito de 200 ng mL^{-1}. Paneles superiores, resultados experimentales de Fu et al. [2012]. Paneles inferiores, resultados numéricos obtenidos en este trabajo, junto con un acercamiento sobre las líneas de test y control. (b) Comparación de las señales en línea de test y concentraciones entre los resultados experimentales de Fu et al. (señales ópticas) y esta tesis (concentraciones de producto), con una serie adicional que muestra la simulación de un formato secuencial basado en el trabajo de Liang et al. [2016] con esta misma geometría.

Capítulo 4

Conclusiones

En esta sección se desarrollan las conclusiones que se han obtenido a través del desarrollo de cada uno de los cuatro grupos de actividades asociadas a cada objetivo específico mencionado en la sección 1.1.2.

1. Investigar posibles esquemas de modelado y desarrollar y validar herramientas numéricas para simulación de flujo no saturado en sustratos porosos de uso en microfluídica, con enfoque especial en casos de flujo lateral y el tratamiento de problemas inversos de estimación de parámetros.

El estudio en particular del flujo lateral llevó al desarrollo de *Fronts*, un conjunto de herramientas de software para resolver problemas de tipo de difusión no lineal a través de la transformación de Boltzmann. Esta herramienta de código abierto se encuentra disponible como paquetes de Julia y Python. Las implementaciones fueron validadas tanto en sus capacidades para resolver problemas directos como en problemas inversos en los que el objetivo es el ajuste de modelos de flujo capilar. Todo el desarrollo es público, en repositorios de GitHub, con documentación para cada paquete, casos de ejemplo y un conjunto de pruebas de validación automatizadas. El desempeño numérico de *Fronts* superior a otras herramientas con objetivos similares.

2. Proponer y validar experimental y numéricamente modelos de flujo no saturado aplicables a microfluídica en papel.

En lo que respecta a los modelos de flujo no saturado, y utilizando la herramientas mencionadas anteriormente, se realizaron ajustes de modelos conocidos a partir de los resultados de experimentos de flujo lateral para lograr la caracterización de un sustrato poroso de uso en microfluídica mediante experimentos conducidos por el mismo tesista. Asimismo, se presentó un modelo propio, consistente en una modificación de otro modelo de la literatura, que demostró buena capacidad pa-

ra reproducir el comportamiento experimental con una cantidad limitada de parámetros libres. Este nuevo modelo permitió por primera vez una aproximación al comportamiento del flujo no saturado en papel a través de un modelo especialmente concebido desde un punto de vista microfluídico, a diferencia de los anteriores de origen hidrológico.

3. Desarrollar y validar herramientas numéricas para simulaciones de transporte en condiciones de flujo saturado y con presencia de campos eléctricos en sustratos de uso en microfluídica.

En cuando al flujo y transporte electroforético en medios porosos saturados, el trabajo culminó en una nueva versión de la herramienta `electroMicroTransport`, con prestaciones para el prototipado exhaustivo de dispositivos de tipo e-μPAD, incluyendo los fenómenos de flujo electroosmótico y dispersión eléctrica y mecánica. Este software de código abierto brinda a la comunidad una alternativa eficiente para el desarrollo y optimización de dispositivos electroforéticos basados en papel. La herramienta es de libre disponibilidad bajo licencia de código abierto, con facilidades para su instalación bajo cualquier sistema operativo (mediante Docker), casos de ejemplo, una aplicación de soporte para la gestión de propiedades de electrolitos, y con una batería de pruebas de validación de ejecución automática durante el proceso de desarrollo.

4. Desarrollar y validar herramientas numéricas que resuelvan flujo y transporte reactivo acoplados en medios porosos no saturados para prototipado numérico de dispositivos microfluidicos en papel.

Se concretó el desarrollo y validación de `porousMicroTransport`, una herramienta novedosa de software para el modelado y simulación de problemas de flujo y transporte reactivo en medios porosos no saturados orientada a sustratos de uso en la microfluídica en papel, especialmente en aplicaciones analíticas. `porousMicroTransport` es también software de código abierto, cuya disponibilidad tiene el potencial de contribuir a la aceleración de las tareas de prototipado de dispositivos de tipo μPAD. Al igual que `electroMicroTransport`, `porousMicroTransport` también utiliza prácticas de modernas en el desarrollo del software (desarrollo abierto en repositorio Git en línea, modularidad en el modelo de reacciones, alternativa de instalación por Docker, pruebas de validación automatizadas).

Finalmente, y más allá del cumplimiento de los objetivos planteados para la tesis, este trabajo implicó aportes significativos para la comunidad de la microfluídica y de la mecánica computacional, verificado no sólo por las publicaciones presentadas como anexos, sino también a través de los diferentes programas y bibliotecas de software producidos, así como otras publicaciones relacionadas

en revistas [Malỳ et al., 2019, Dovhunová et al., 2020, Schaumburg et al., 2022, Horgue et al., 2022, Macagno et al., 2023, Franck et al., 2023] y una importante cantidad de presentaciones en congresos nacionales e internacionales tanto en el ámbito de la microfluídica como de la mecánica computacional.

4.1. Trabajos futuros

Se identifican las siguientes actividades como posibles trabajos futuros. En primer lugar, se ha comenzado la extensión de *Fronts* para abarcar problemas en los que la aplicabilidad de la transformación de Boltzmann está limitada a ciertas porciones del dominio espacio-temporal. Esta nueva funcionalidad permite la solución de problemas más generales de flujo lateral con mayor eficiencia que los métodos numéricos convencionales, a la vez que se mejoran las capacidades de uso como herramienta de caracterización de sustratos dado que se eliminan restricciones sobre los experimentos cuyos resultados son aplicables a la modalidad de resolución inversa.

En cuanto a los modelos de flujo no saturado, se identifica como una limitación del modelado matemático a partir de la ecuación de Richards "horizontal" la imposibilidad de diferenciar los efectos de la presión capilar con los de la permeabilidad relativa, los cuales se confunden en este tipo de modelado. En el futuro, se podrían diseñar experimentos específicos que luego se traduzcan en nuevos modelos donde se capturen ambos fenómenos por separado, para un modelado más preciso del comportamiento. El modelado computacional para el proceso de ajuste de los modelos podría utilizar nuevas funcionalidades en *Fronts*, o bien las prestaciones más generales de `porousMicroTransport`.

Finalmente, se ha identificado la potencialidad de integración de las herramientas `electroMicroTransport` y `porousMicroTransport`. Esta posibilidad debería ser objeto de estudio, y permitiría, entre otras mejoras, resolver problemas de flujo electroforético en medios no saturados y/o con reacciones, que hoy deben modelarse en etapas desacopladas con las diferentes herramientas.

De manera más abarcativa, todos los conocimientos adquiridos por el tesista en cuanto a la temática de flujo en materiales porosos, transporte en estos medios, modelado de reacciones y campos eléctricos serán de utilidad para su empleo en el modelado y simulación de medios porosos en aplicaciones energéticas, temática para la actividad posdoctoral que se tiene planificada y que se desarrollará en tanto se obtenga el financiamiento.

Bibliografía

K. M. Abou El-Nour, I. M. El-Sherbiny, A. M. Abbas, E. H. Salem, and G. M. Khairy. Applying smartphone camera, spectrophotometry, or ocular analysis-based dipsticks for the detection of glutathione level as a cancer biomarker. *Talanta Open*, 7:100211, 2023. doi: 10.1016/j.talo.2023.100211.

J. I. Aguiar, A. O. Rangel, and R. B. Mesquita. Salivary calcium determination with a specially developed microfluidic paper-based device for point-of-care analysis. *Talanta Open*, 8:100254, 2023. doi: 10.1016/j.talo.2023.100254.

K. Alastal and R. Ababou. Moving multi-front (MMF): A generalized Green-Ampt approach for vertical unsaturated flows. *Journal of Hydrology*, 579:124184, 2019. doi: 10.1016/j.jhydrol.2019.124184.

P. O. Andersen. Insights from Boltzmann transformation in solving 1d counter-current spontaneous imbibition at early and late time. *Advances in Geo-Energy Research*, 7:164–175, 2023. doi: 10.46690/ager.2023.03.03.

Anushka, A. Bandopadhyay, and P. K. Das. Paper based microfluidic devices: a review of fabrication techniques and applications. *The European Physical Journal Special Topics*, 232(6): 781–815, 2023. doi: 10.1140/epjs/s11734-022-00727-y.

H. Asadi, M. Pourjafar-Chelikdani, N. P. Khabazi, and K. Sadeghy. Quasi-steady imbibition of physiological liquids in paper-based microfluidic kits: Effect of shear-thinning. *Physics of Fluids*, 34(12):123111, 2022. doi: 10.1063/5.0131335.

J. Bear and A. H.-D. Cheng. *Modeling groundwater flow and contaminant transport*, volume 23. Springer Science & Business Media, Dordrecht, Netherlands, 2010. doi: 10.1007/978-1-4020-6682-5.

M. Bercovici, S. K. Lele, and J. G. Santiago. Open source simulation tool for electrophoretic

stacking, focusing, and separation. *J. Chromatogr. A*, 1216(6):1008–1018, 2009. doi: 10.1016/j.chroma.2008.12.022.

C. L. A. Berli and P. A. Kler. A quantitative model for lateral flow assays. *Microfluidics and Nanofluidics*, 20(7):104, 2016. doi: 10.1007/s10404-016-1771-9.

H. Berthet, H. Stone, F. Marty, B. Mercier, J. Jundt, and D. E. Angelescu. Design and characterization of a MEMS-microfluidic sensor for rheological applications. *Advanced Materials Research*, 74:81–84, 2009. doi: 10.4028/www.scientific.net/AMR.74.81.

J. Bezanson, A. Edelman, S. Karpinski, and V. B. Shah. Julia: A fresh approach to numerical computing. *SIAM review*, 59(1):65–98, 2017. doi: 10.1137/141000671.

M. Bier, O. Palusinski, R. Mosher, and D. Saville. Electrophoresis: Mathematical modeling and computer simulation. *Science*, 219(4590):1281–1287, 1983. doi: 10.1126/science.6828855.

L. Boltzmann. Zur Integration der Diffusionsgleichung bei variabeln Diffusionscoefficienten (To integrate the diffusion equation with variable diffusion coefficients). *Annalen der Physik*, 289 (13):959–964, 1894. doi: 10.1002/andp.18942891315.

R. Braddock and J.-Y. Parlange. Some accurate numerical solutions of the soil-water diffusion equation. *Soil Science Society of America Journal*, 44(3):656–658, 1980. doi: 10.2136/sssaj1980.03615995004400030047x.

R. Brooks and T. Corey. Hydraulic properties of porous media. *Hydrology Papers, Colorado State University*, 24:37, 1964.

R. Bruce and A. Klute. The measurement of soil moisture diffusivity. *Soil Science Society of America Journal*, 20(4):458–462, 1956. doi: 10.2136/sssaj1956.03615995002000040004x.

D. Caviedes-Voullième, P. García, J. Murillo, et al. Verification, conservation, stability and efficiency of a finite volume method for the 1D Richards equation. *Journal of hydrology*, 480: 69–84, 2013. doi: 10.1016/j.jhydrol.2012.12.008.

C. L. Chagas, F. R. de Souza, T. M. Cardoso, R. C. Moreira, J. A. da Silva, D. P. de Jesus, and W. K. Coltro. A fully disposable paper-based electrophoresis microchip with integrated pencil-drawn electrodes for contactless conductivity detection. *Analytical Methods*, 8(37):6682–6686, 2016. doi: 10.1039/C6AY01963C.

X. Chen and Y. Dai. An approximate analytical solution of Richards' equation. *International Journal of Nonlinear Sciences and Numerical Simulation*, 16(5):239–247, 2015. doi: 10.1186/s13661-017-0893-7.

H. Cremer, A. Tiselius, et al. Electrophoresis of protein on filter paper. *Biochemische Zeitschrift*, 320:273–283, 1950.

B. M. Cummins, R. Chinthapatla, F. S. Ligler, and G. M. Walker. Time-dependent model for fluid flow in porous materials with multiple pore sizes. *Analytical Chemistry*, 89(8):4377–4381, 2017. doi: 10.1021/acs.analchem.6b04717.

S. Das and S. K. Mitra. Different regimes in vertical capillary filling. *Physical Review E*, 87(6): 063005, 2013. doi: 10.1103/PhysRevE.87.063005.

S. Di Fraia, N. Massarotti, and P. Nithiarasu. Modelling electro-osmotic flow in porous media: a review. *International Journal of Numerical Methods for Heat & Fluid Flow*, 28(2):472–497, 2018. doi: 10.1108/HFF-11-2016-0437.

M. Dovhunová, M. Malỳ, P. Dubskỳ, G. S. Gerlero, and P. A. Kler. Generalized model of the linear theory of electromigration and its application to electrokinetic chromatography: Capillary zone electrophoretic systems with complex-forming equilibria. *Journal of Chromatography A*, 1610: 460595, 2020. doi: 10.1016/j.chroma.2019.460595.

E. Elizalde, R. Urteaga, and C. L. A. Berli. Rational design of capillary-driven flows for paper-based microfluidics. *Lab on a Chip*, 15(10):2173–2180, 2015. doi: 10.1039/C4LC01487A.

E. Elizalde, R. Urteaga, and C. L. A. Berli. Precise capillary flow for paper-based viscometry. *Microfluidics and Nanofluidics*, 20(10):1–8, 2016. doi: 10.1007/s10404-016-1800-8.

C. Evangelides, G. Arampatzis, and C. Tzimopoulos. Estimation of soil moisture profile and diffusivity using simple laboratory procedures. *Soil science*, 175(3):118–127, 2010. doi: 10.1097/SS.0b013e3181d53bb6.

M. W. Farthing and F. L. Ogden. Numerical solution of Richards' equation: A review of advances and challenges. *Soil Science Society of America Journal*, 81(6):1257–1269, 2017. doi: 10.2136/sssaj2017.02.0058.

N. Franck, F. Schaumburg, P. A. Kler, and R. Urteaga. Precise electroosmotic flow measurements on paper substrates. *Electrophoresis*, 42(7-8):975–982, 2021. doi: 10.1002/elps.202000271.

N. Franck, L. Vera Candioti, G. S. Gerlero, R. Urteaga, and P. A. Kler. A simple method for the assessment of electrophoretic mobility in porous media. *Electrophoresis*, 45(7-8), 2023. doi: 10.1002/elps.202300180.

E. Fu, T. Liang, P. Spicar-Mihalic, J. Houghtaling, S. Ramachandran, and P. Yager. Two-dimensional paper network format that enables simple multistep assays for use in low-resource settings in the context of malaria antigen detection. *Analytical Chemistry*, 84(10):4574–4579, 2012. doi: 10.1021/ac300689s.

P. Gamazo, L. J. Slooten, J. Carrera, M. W. Saaltink, S. Bea, and J. Soler. PROOST: object-oriented approach to multiphase reactive transport modeling in porous media. *Journal of Hydroinformatics*, 18(2):310–328, 2016. doi: 10.2166/hydro.2015.126.

L. Ge, S. Wang, S. Ge, J. Yu, M. Yan, N. Li, and J. Huang. Electrophoretic separation in a microfluidic paper-based analytical device with an on-column wireless electrogenerated chemiluminescence detector. *Chemical Communications*, 50(43):5699–5702, 2014. doi: 10.1039/c3cc49770d.

G. S. Gerlero, S. M. Damián, and P. A. Kler. electroMicroTransport v2107: Open-source toolbox for paper-based electromigrative separations. *Computer Physics Communications*, 269:108143, 2021a. doi: 10.1016/j.cpc.2021.108143.

G. S. Gerlero, S. Marquez Damián, F. Schaumburg, N. Franck, and P. A. Kler. Numerical simulations of paper-based electrophoretic separations with open-source tools. *Electrophoresis*, 42 (16):1543–1551, 2021b. doi: 10.1002/elps.202000315.

G. S. Gerlero, A. R. Valdez, R. Urteaga, and P. A. Kler. Validity of capillary imbibition models in paper-based microfluidic applications. *Transport in Porous Media*, 141(2):359–378, 2022. doi: 10.1007/s11242-021-01724-w.

G. S. Gerlero, C. L. A. Berli, and P. A. Kler. Open-source high-performance software packages for direct and inverse solving of horizontal capillary flow. *Capillarity*, 6(2):31–40, 2023. doi: 10.46690/capi.2023.02.02.

M. M. Gong and D. Sinton. Turning the page: advancing paper-based microfluidics for broad diagnostic application. *Chem. Rev.*, 117(12):8447–8480, 2017. doi: 10.1021/acs.chemrev.7b00024.

N. N. Hamidon, G. I. Salentijn, and E. Verpoorte. Enhanced passive mixing for paper microfluidics. *RSC advances*, 11(41):25677–25685, 2021. doi: 10.1039/D1RA04916J.

S.-u. Hassan, A. Tariq, Z. Noreen, A. Donia, S. Z. Zaidi, H. Bokhari, and X. Zhang. Capillary-driven flow microfluidics combined with smartphone detection: An emerging tool for point-of-care diagnostics. *Diagnostics*, 10(8):509, 2020. doi: 10.3390/diagnostics10080509.

M. Hayek. An efficient analytical model for horizontal infiltration in soils. *Journal of Hydrology*, 564:1120–1132, 2018. doi: 10.1016/j.jhydrol.2018.07.058.

M. J. Hertaeg, R. F. Tabor, J. D. Berry, and G. Garnier. Radial wicking of biological fluids in paper. *Langmuir*, 36(28):8209–8217, 2020. doi: 10.1021/acs.langmuir.0c01318.

T. Hirokawa, M. Nishino, N. Aoki, Y. Kiso, Y. Sawamoto, T. Yagi, and J.-I. Akiyama. Table of isotachophoretic indices: I. simulated qualitative and quantitative indices of 287 anionic substances in the range ph 3–10. *J. Chromatogr. A*, 271(2):D1–D106, 1983. doi: 10.1016/S0021-9673(00)80225-3.

P. Horgue, F. Renard, G. S. Gerlero, R. Guibert, and G. Debenest. porousMultiphaseFoam v2107: An open-source tool for modeling saturated/unsaturated water flows and solute transfers at watershed scale. *Computer Physics Communications*, 273:108278, 2022. doi: 10.1016/j.cpc.2021.108278.

V. Hruška, M. Jaroš, and B. Gaš. Simul 5 – free dynamic simulator of electrophoresis. *Electrophoresis*, 27(5-6):984–991, 2006. doi: 10.1002/elps.200500756.

H. Jasak. *Error analysis and estimation for the finite volume method with applications to fluid flows*. PhD thesis, Department of Mechanical Engineering, Imperial College of Science, Technology and Medicine, London, UK, 1996.

J. W. Jorgenson and K. D. Lukacs. Zone electrophoresis in open-tubular glass capillaries. *Anal. Chem.*, 53(8):1298–1302, 1981. doi: 10.1016/0165-9936(84)87053-3.

T. H. Kim, Y. K. Hahn, and M. S. Kim. Recent advances of fluid manipulation technologies in microfluidic paper-based analytical devices (μPADs) toward multi-step assays. *Micromachines*, 11(3):269, 2020. doi: 10.3390/mi11030269.

A. Klute. A numerical method for solving the flow equation for water in unsaturated materials. *Soil Science*, 73(2):105–116, 1952. doi: 10.1097/00010694-195202000-00003.

H. G. Kunkel and A. Tiselius. Electrophoresis of proteins on filter paper. *Journal of General Physiology*, 35(1):89–118, 1951. doi: 10.1085/jgp.35.1.89.

A. J. Ladd and P. Szymczak. Reactive flows in porous media: challenges in theoretical and numerical methods. *Annual review of chemical and biomolecular engineering*, 12:543–571, 2021. doi: 10.1146/annurev-chembioeng-092920-102703.

W. Lai and F. L. Ogden. A mass-conservative finite volume predictor–corrector solution of the 1D Richards' equation. *Journal of Hydrology*, 523:119–127, 2015. doi: 10.1016/j.jhydrol.2015.01.053.

T. Liang, R. Robinson, J. Houghtaling, G. Fridley, S. A. Ramsey, and E. Fu. Investigation of reagent delivery formats in a multivalent malaria sandwich immunoassay and implications for assay performance. *Analytical chemistry*, 88(4):2311–2320, 2016. doi: 10.1021/acs.analchem.5b04222.

P. Lichtner, G. Hammond, C. Lu, S. Karra, G. Bisht, B. Andre, R. Mills, and J. Kumar. PFLOTRAN user manual: A massively parallel reactive flow and transport model for describing subsurface processes. https://www.pflotran.org/, 2017.

H. Lim, A. T. Jafry, and J. Lee. Fabrication, flow control, and applications of microfluidic paper-based analytical devices. *Molecules*, 24(16):2869, 2019. doi: 10.3390/molecules24162869.

F. List and F. A. Radu. A study on iterative methods for solving Richards' equation. *Computational Geosciences*, 20(2):341–353, 2016. doi: 10.1007/s10596-016-9566-3.

Y. Liu, L. Sun, H. Zhang, L. Shang, and Y. Zhao. Microfluidics for drug development: from synthesis to evaluation. *Chemical reviews*, 121(13):7468–7529, 2021. doi: 10.1021/acs.chemrev.0c01289.

F. Lomeland. Overview of the LET family of versatile correlations for flow functions. In *Proceedings of the International Symposium of the Society of Core Analysts*, pages SCA2018–056, 2018.

F. Lomeland and E. Ebeltoft. A new versatile capillary pressure correlation. In *Proceedings of the International Symposium of the Society of Core Analysts*, volume 29, pages SCA2008–08, 2008.

F. Lomeland, E. Ebeltoft, and W. H. Thomas. A new versatile relative permeability correlation. In *Proceedings of the International Symposium of the Society of Core Analysts*, volume 112, pages SCA2005–32, 2005.

D. Mabey, R. W. Peeling, A. Ustianowski, and M. D. Perkins. Diagnostics for the developing world. *Nature Reviews Microbiology*, 2(3):231–240, 2004. doi: 10.1038/nrmicro841.

J. Macagno, G. S. Gerlero, M. L. Satuf, and C. L. A. Berli. Field-deployable aptasensor with automated analysis of stain patterns for the detection of chlorpyrifos in water. *Talanta*, 252: 123782, 2023.

M. Malỳ, M. Dovhunová, M. Dvořák, G. S. Gerlero, P. A. Kler, V. Hruška, and P. Dubskỳ. Generalized model of the linear theory of electromigration and its application to electrokinetic chromatography: Theory and software peakmaster 6—next generation. *Electrophoresis*, 40(5): 683–692, 2019. doi: 10.1002/elps.201800400.

S. Márquez Damián, F. Schaumburg, and P. A. Kler. Open-source toolbox for electromigrative separations. *Comput. Phys. Commun.*, 237:244–252, 2019. doi: 0.1016/j.cpc.2018.11.015.

S. A. Mathias and G. C. Sander. Pseudospectral methods provide fast and accurate solutions for the horizontal infiltration equation. *Journal of Hydrology*, 598:126407, 2021. doi: 10.1016/j.jhydrol.2021.126407.

D. Merkel et al. Docker: lightweight linux containers for consistent development and deployment. *Linux Journal*, 239(2):2, 2014.

P. Mesquita, L. Gong, and Y. Lin. Low-cost microfluidics: Towards affordable environmental monitoring and assessment. *Frontiers in Lab on a Chip Technologies*, 1:1074009, 2022. doi: 10.3389/frlct.2022.1074009.

S. Modha, C. Castro, and H. Tsutsui. Recent developments in flow modeling and fluid control for paper-based microfluidic biosensors. *Biosensors and Bioelectronics*, page 113026, 2021. doi: 10.1016/j.bios.2021.113026.

B. Y. Moghadam, K. T. Connelly, and J. D. Posner. Isotachophoretic preconcenetration on paper-based microfluidic devices. *Analytical Chemistry*, 86(12):5829–5837, 2014. doi: 10.1021/ac500780w.

B. Y. Moghadam, K. T. Connelly, and J. D. Posner. Two orders of magnitude improvement in detection limit of lateral flow assays using isotachophoresis. *Analytical Chemistry*, 87(2):1009–1017, 2015. doi: 10.1021/ac504552r.

M. F. Mora, C. D. Garcia, F. Schaumburg, P. A. Kler, C. L. A. Berli, M. Hashimoto, and E. Carrilho. Patterning and modeling three-dimensional microfluidic devices fabricated on a single sheet of paper. *Analytical chemistry*, 91(13):8298–8303, 2019. doi: 10.1021/acs.analchem.9b01020.

G. Ocvirk, M. Munroe, T. Tang, R. Oleschuk, K. Westra, and D. J. Harrison. Electrokinetic control of fluid flow in native poly(dimethylsiloxane) capillary electrophoresis devices. *Electrophoresis*, 21(1):107–115, 2000. doi: 10.1002/(SICI)1522-2683(20000101)21:1<107::AID-ELPS107>3.0.CO;2-Y.

T. Ozer, C. McMahon, and C. S. Henry. Advances in paper-based analytical devices. *Annual Review of Analytical Chemistry*, 13:85–109, 2020. doi: 10.1146/annurev-anchem-061318-114845.

B. Pan, C. R. Clarkson, M. Atwa, X. Tong, C. Debuhr, A. Ghanizadeh, and V. I. Birss. Spontaneous imbibition dynamics of liquids in partially-wet nanoporous media: Experiment and theory. *Transport in Porous Media*, 137(3):555–574, 2021. doi: 10.1007/s11242-021-01574-6.

A. Perez-Cruz, I. Stiharu, and A. Dominguez-Gonzalez. Two-dimensional model of imbibition into paper-based networks using Richards' equation. *Microfluidics and Nanofluidics*, 21(5):98, 2017. doi: 10.1007/s10404-017-1937-0.

J. Philip. Numerical solution of equations of the diffusion type with diffusivity concentration-dependent. *Transactions of the Faraday Society*, 51:885–892, 1955. doi: 10.1039/tf9555100885.

J. Philip. General method of exact solution of the concentration-dependent diffusion equation. *Australian Journal of Physics*, 13:1, 1960. doi: 10.1071/PH600001.

W. H. Press, S. A. Teukolsky, W. T. Vetterling, and B. P. Flannery. *Numerical Recipes 3rd Edition: The Art of Scientific Computing*. Cambridge University Press, New York, NY, USA, third edition, 2007. ISBN 0521880688, 9780521880688.

C. L. Prevedello, J. M. Loyola, K. Reichardt, and D. R. Nielsen. New analytic solution of Boltzmann transform for horizontal water infiltration into sand. *Vadose Zone Journal*, 7(4):1170–1177, 2008. doi: 10.2136/vzj2007.0181.

C. Rackauckas and Q. Nie. DifferentialEquations.jl – a performant and feature-rich ecosystem for solving differential equations in Julia. *Journal of Open Research Software*, 5(1), 2017. doi: 10.5334/jors.151.

D. Rath and B. J. Toley. Modeling-guided design of paper microfluidic networks: A case study of sequential fluid delivery. *ACS sensors*, 6(1), 2021. doi: 10.1021/acssensors.0c01840.

D. Rath, N. Sathishkumar, and B. J. Toley. Experimental measurement of parameters governing flow rates and partial saturation in paper-based microfluidic devices. *Langmuir*, 34(30):8758–8766, 2018. doi: 10.1021/acs.langmuir.8b01345.

L. A. Richards. Capillary conduction of liquids through porous mediums. *Physics*, 1(5):318–333, 1931. doi: 10.1063/1.1745010.

T. Rosenfeld and M. Bercovici. 1000-fold sample focusing on paper-based microfluidic devices. *Lab on a Chip*, 14(23):4465–4474, 2014. doi: 10.1039/C4LC00734D.

T. Rosenfeld and M. Bercovici. Amplification-free detection of dna in a paper-based microfluidic device using electroosmotically balanced isotachophoresis. *Lab on a Chip*, 18(6):861–868, 2018. doi: 10.1039/C7LC01250K.

T. Rosenfeld and M. Bercovici. Dynamic control of capillary flow in porous media by electroosmotic pumping. *Lab on a Chip*, 19(2):328–334, 2019. doi: 10.1039/C8LC01077C.

A. L. Ruoff, D. L. Prince, J. C. Giddings, and G. H. Stewart. The diffusion analogy for solvent flow in paper. *Kolloid-Zeitschrift*, 166(2):144–151, 1959. doi: 10.1007/BF01681187.

A. L. Ruoff, G. H. Stewart, H. K. Shin, and J. C. Giddings. Diffusion of liquids in unsaturated paper. *Kolloid-Zeitschrift*, 173(1):14, 1960. doi: 10.1007/BF01513622.

G. I. Salentijn, M. Grajewski, and E. Verpoorte. Reinventing (bio)chemical analysis with paper. *Anal. Chem.*, 90(23):13815–13825, 2018. doi: 10.1021/acs.analchem.8b04825.

T. Santagata, R. Solimene, G. Aprea, and P. Salatino. Modelling and experimental characterization of unsaturated flow in absorbent and swelling porous media: Material characterization. *Transport in Porous Media*, 134(3):725–753, 2020. doi: 10.1007/s11242-020-01467-0.

N. Scales and R. N. Tait. Modeling electroosmotic and pressure-driven flows in porous microfluidic devices: Zeta potential and porosity changes near the channel walls. *The Journal of Chemical Physics*, 125(9):094714, 2006. doi: 10.1063/1.2335846.

F. Schaumburg and C. L. A. Berli. Assessing the rapid flow in multilayer paper-based microfluidic devices. *Microfluidics and Nanofluidics*, 23(8):98, 2019. doi: 10.1007/s10404-019-2265-3.

F. Schaumburg, P. A. Kler, and C. L. A. Berli. Numerical prototyping of lateral flow biosensors. *Sensors and Actuators B: Chemical*, 259:1099–1107, 2018a. doi: 10.1016/j.snb.2017.12.044.

F. Schaumburg, R. Urteaga, P. A. Kler, and C. L. A. Berli. Design keys for paper-based concentration gradient generators. *Journal of Chromatography A*, 1561:83–91, 2018b. doi: 10.1016/j.chroma.2018.05.040.

F. Schaumburg, P. A. Kler, and C. L. A. Berli. Comprehensive model of electromigrative transport in microfluidic paper based analytical devices. *Electrophoresis*, 41(7-8):598–606, 2020a. doi: 10.1002/elps.201900353.

F. Schaumburg, P. A. Kler, C. S. Carrell, C. L. A. Berli, and C. S. Henry. Usb powered microfluidic paper-based analytical devices. *Electrophoresis*, 41(7-8):562–569, 2020b. doi: 10.1002/elps.201900273.

F. Schaumburg, J. P. Vidocevich, G. S. Gerlero, N. Pujato, J. Macagno, P. A. Kler, and C. L. A. Berli. A free customizable tool for easy integration of microfluidics and smartphones. *Scientific Reports*, 12(1):8969, 2022. doi: 10.1038/s41598-022-13099-z.

M. Shanmugam, G. S. Kumar, B. Narasimhan, and S. Shrestha. Effective saturation-based weighting for interblock hydraulic conductivity in unsaturated zone soil water flow modelling using one-dimensional vertical finite-difference model. *Journal of Hydroinformatics*, 22(2):423–439, 2020. doi: 10.2166/hydro.2019.239.

A. L. Shapiro, E. Viñuela, and J. V. Maizel Jr. Molecular weight estimation of polypeptide chains by electrophoresis in sds-polyacrylamide gels. *Biochemical and Biophysical Research Communications*, 28(5):815–820, 1967. doi: 10.1016/0006-291X(67)90391-9.

A. P. Shapiro and R. F. Probstein. Removal of contaminants from saturated clay by electroosmosis. *Environmental Science and Technology*, 27(2):283–291, 1993. doi: 10.1021/es00039a007.

A. Sharma, B. K. Kashyap, and N. Puranik. *State-of-the-art of paper-based technology and challenges in its commercialization*, pages 11–1–11–20. IOP Publishing Bristol, UK, 2023. doi: 10.1088/978-0-7503-5820-0ch11.

H. A. Silva-Neto, I. V. Arantes, A. L. Ferreira, G. H. do Nascimento, G. N. Meloni, W. R. de Araujo, T. R. Paixão, and W. K. Coltro. Recent advances on paper-based microfluidic devices for bioanalysis. *TrAC Trends in Analytical Chemistry*, 158:116893, 2023. doi: 10.1016/j.trac.2022.116893.

L. Su, Q. Wang, X. Qin, Y. Shan, and X. Wang. Analytical solution of a one-dimensional horizontal-absorption equation based on the brooks–corey model. *Soil Science Society of America Journal*, 81(3):439–449, 2017. doi: 10.2136/sssaj2016.06.0189.

J. Sun, Z. Li, F. Furtado, and S. A. Aryana. A microfluidic study of transient flow states in permeable media using fluorescent particle image velocimetry. *Capillarity*, 4(4), 2021. doi: 10.46690/capi.2021.04.03.

A. Terzis, G. Yang, I. Zarikos, E. Elizalde, B. Weigand, A. Kalfas, and X. Ding. A temperature-based diagnostic approach for paper-based microfluidics. *Microfluidics and Nanofluidics*, 22 (3):1–6, 2018. doi: 10.1007/s10404-018-2054-4.

W. Thormann, J. Caslavska, and R. Mosher. Modeling of electroosmotic and electrophoretic mobilization in capillary and microchip isoelectric focusing. *Journal of Chromatography A*, 1155 (2):154–163, 2007. doi: 10.1016/j.chroma.2007.01.121.

J. Tirapu-Azpiroz, A. F. Silva, M. E. Ferreira, W. F. L. Candela, P. W. Bryant, R. L. Ohta, M. Engel, and M. B. Steiner. Modeling fluid transport in two-dimensional paper networks. *Journal of Micro/Nanolithography, MEMS, and MOEMS*, 17(2):025003, 2018. doi: 10.1117/1.JMM.17.2.025003.

C. J. Toft, R. A. Bourquin, A. E. Sorenson, P. F. Horwood, J. D. Druce, and P. M. Schaeffer. Analytical sensitivity of COVID-19 rapid antigen tests: A case for a robust reference standard. *Talanta Open*, 7:100187, 2023. doi: 10.1016/j.talo.2023.100187.

C. Tzimopoulos, C. Evangelides, and G. Arampatzis. Explicit approximate analytical solution of the horizontal diffusion equation. *Soil Science*, 180(2):47–53, 2015. doi: 10.1097/SS.0000000000000113.

R. Urteaga, E. Elizalde, and C. L. A. Berli. Transverse solute dispersion in microfluidic paper-based analytical devices (μPADs). *Analyst*, 2018. doi: 10.1039/C8AN00149A.

M. T. Van Genuchten. A closed-form equation for predicting the hydraulic conductivity of unsaturated soils. *Soil Science Society of America journal*, 44(5):892–898, 1980. doi: 10.2136/sssaj1980.03615995004400050002x.

P. Virtanen, R. Gommers, T. E. Oliphant, M. Haberland, T. Reddy, D. Cournapeau, E. Burovski, P. Peterson, W. Weckesser, J. Bright, et al. SciPy 1.0: fundamental algorithms for scientific computing in Python. *Nature Methods*, 17(3):261–272, 2020. doi: 10.1038/s41592-019-0686-2.

N. Wang, J. Zhang, B. Xiao, and A. Chen. Microfluidic-assisted integrated nucleic acid test strips for poct. *Talanta*, page 125150, 2023. doi: 10.1016/j.talanta.2023.125150.

H. G. Weller, G. Tabor, H. Jasak, and C. Fureby. A tensorial approach to computational continuum mechanics using object-oriented techniques. *Computers in Physics*, 12(6):620–631, 1998. doi: 10.1063/1.168744.

C. Xu, W. Lin, and L. Cai. Demonstrating electrophoretic separation in a straight paper channel delimited by a hydrophobic wax barrier. *Journal of Chemical Education*, 93(5):903–905, 2016. doi: 10.1021/acs.jchemed.5b00674.

P. Yager, T. Edwards, E. Fu, K. Helton, K. Nelson, M. R. Tam, and B. H. Weigl. Microfluidic diagnostic technologies for global public health. *Nature*, 442(7101):412–418, 2006. doi: 10.1038/nature05064.

K. Yamada, H. Shibata, K. Suzuki, and D. Citterio. Toward practical application of paper-based microfluidics for medical diagnostics: state-of-the-art and challenges. *Lab on a Chip*, 17(7): 1206–1249, 2017. doi: 10.1039/c6lc01577h.

X. Yang, H. Sun, Y. Yang, Y. Liu, and X. Li. Recent progress in multi-scale modeling and simulation of flow and solute transport in porous media. *Wiley Interdisciplinary Reviews: Water*, 8(6): e1561, 2021. doi: 10.1002/wat2.1561.

A. K. Yetisen, M. S. Akram, and C. R. Lowe. Paper-based microfluidic point-of-care diagnostic devices. *Lab on a Chip*, 13(12):2210–2251, 2013. doi: 10.1039/c3lc50169h.

J. Šimůnek, M. T. Van Genuchten, and M. Šejna. Recent developments and applications of the HYDRUS computer software packages. *Vadose Zone Journal*, 15(7), 2016. doi: 10.2136/vzj2016.04.0033.

Anexos

En referencia a los artículos presentados a continuación en los Anexos A a E:

- G. S. Gerlero, C. L. A. Berli, P. A. Kler. Open-source high-performance software packages for direct and inverse solving of horizontal capillary flow. *Capillarity*, 6(2):31–40, 2023.
- G. S. Gerlero, A. R. Valdez, R. Urteaga, P. A. Kler. Validity of capillary imbibition models in paper-based microfluidic applications. *Transport in Porous Media*, 141(2):359–378, 2022.
- G. S. Gerlero, S. Márquez Damián, F. Schaumburg, N. Franck, P. A. Kler. Numerical simulations of paper-based electrophoretic separations with open-source tools. *Electrophoresis*, 42(16):1543–1551, 2021.
- G. S. Gerlero, S. Márquez Damián, P. A. Kler. electroMicroTransport v2107: Open-source toolbox for paper-based electromigrative separations. *Computer Physics Communications*, 269:108143, 2021.
- G. S. Gerlero, C. L. A. Berli, P. A. Kler. Comprehensive numerical prototyping of paper-based microfluidic devices using open-source tools. En revisión.

el tesista asumió en todos ellos el rol de autor principal y declara haber realizado contribuciones esenciales en cada uno de ellos, particularmente en el modelado matemático, desarrollo de software, diseños experimentales, ejecución de los experimentos, validación y escritura de los trabajos; bajo la tutela del director y co-director de tesis y con las contribuciones de los otros co-autores de cada trabajo. El director y co-director de tesis avalan esta declaración.

Dr. Pablo A. Kler	Dr. Claudio L. A. Berli
Director	Co-director

Anexo A

Open-source high-performance software packages for direct and inverse solving of horizontal capillary flow

El artículo presentado a continuación ha sido publicado en la revista **Capillarity**.

G. S. Gerlero, C. L. A. Berli, P. A. Kler. Open-source high-performance software packages for direct and inverse solving of horizontal capillary flow. *Capillarity*, 6(2):31–40, 2023. https://doi.org/10.46690/capi.2023.02.02

Open-source high-performance software packages for direct and inverse solving of horizontal capillary flow

Gabriel S. Gerlero[1], Claudio L. A. Berli[2], Pablo A. Kler[1,3]

[1]Centro de Investigación de Métodos Computacionales (CIMEC, UNL–CONICET), Colectora RN 168 km 472, Santa Fe, Argentina

[2]Instituto de Desarrollo Tecnológico para la Industria Química (INTEC, UNL–CONICET), Colectora RN 168 km 472, Santa Fe, Argentina

[3]Departamento de Ingeniería en Sistemas de Información, Facultad Regional Santa Fe, Universidad Tecnológica Nacional, Lavaisse 610, Santa Fe, Argentina

Abstract

This work introduces *Fronts*, a set of open-source numerical software packages for nonlinear horizontal capillary-driven flow problems in unsaturated porous media governed by the Richards equation. The software uses the Boltzmann transformation to solve such problems in semi-infinite domains. The scheme adopted by *Fronts* allows it to be faster and easier to use than other tools, and provide continuous functions for all involved fields. The software is capable of solving problems that appear in hydrology, but also in other particular domains of interest such as paper-based microfluidics. As the first known open-source implementation to adopt this approach, *Fronts* has been validated against analytical solutions as well as existing software achieving remarkable results in terms of computational costs and numerical precision, and is meant to aid the study and modeling of capillary flow. *Fronts* can be freely downloaded and installed, and offers a friendly environment for new users with its complete documentation and tutorial cases.

Keywords: Richards equation, Horizontal flow, Nonlinear diffusion, Boltzmann transformation, Julia language.

A.1. Introduction

Fluid flow in unsaturated porous media can be modeled with the Richards equation [Richards, 1931]. This is a nonlinear partial differential equation that describes changes in moisture content and/or pressure from the effects of gravity and capillary action. Porous-media flow models provide closed-form expressions for the necessary constitutive relations [Sun et al., 2021]. A special case of the Richards equation occurs where the flow is horizontal or the effect of gravity can be otherwise neglected—where it is also known as the moisture diffusivity equation [Bear and Cheng, 2010].

As a partial differential equation, the Richards equation is commonly solved with numerical methods based on the finite difference, finite element, or finite volume methods, paired with either fixed-point iteration (Picard's method) or Newton–Raphson method to deal with the nonlinear terms [Farthing and Ogden, 2017, List and Radu, 2016, Lai and Ogden, 2015, Caviedes-Voullième et al., 2013]. Software packages that follow these schemes are widely available and used in hydrology, and range from tools designed exclusively for one-dimensional cases [Šimůnek et al., 2016] to others that extend support to arbitrary geometries [Horgue et al., 2022]. However, the aforementioned nonlinear terms included in the equations to be solved imply serious computational challenges for these methods, and hence research on improved numerical schemes for these applications is still ongoing. Such research can consider one-dimensional vertical, or horizontal geometries. In the first group, for instance, List and Radu [2016] proposed a new linearization scheme with better convergence properties; Alastal and Ababou [2019] developed a particular *Moving Multi-Front* method for solving the Richards equation for unsaturated flow in vertical homogeneous porous columns, and Shanmugam et al. [2020] presented a weighting scheme for the computation of hydraulic conductivities that can produce more accurate results. A small snapshot of the different software currently available for solving problems Richards equation is reported in Table A.1.

Alternatively, in the presence of horizontal flow, the Richards equation is susceptible to the Boltzmann transformation [Boltzmann, 1894] [1]. This similarity transformation reduces the nonlinear partial differential equation to an equivalent nonlinear ordinary differential equation, and can be applied to problems of horizontal flow in semi-infinite domains [Bear and Cheng, 2010]. This ap-

[1] The Boltzmann transformation is not compatible with gravitational terms in the general Richards equation. Nevertheless, it is possible to use the solution of a horizontal problem as starting point for the solution to a problem in which gravity is considered [Chen and Dai, 2015].

proach has seen adoption by researchers looking for analytical solutions to problems of unsaturated flow [Philip, 1960, Prevedello et al., 2008, Su et al., 2017]; however, exact solutions are limited to problems with diffusivity functions restricted to a few particular forms, excluding those currently accepted as the most accurate. More recently, the Boltzmann transformation has been applied in the formulation of semi-analytical methods for these problems [Chen and Dai, 2015, Tzimopoulos et al., 2015]. Hayek [2018] presented a general approximate analytical method for the Richards equation in horizontal flow; unfortunately, as discussed in the paper, the method is incompatible with certain constitutive models (notably, the Van Genuchten model). Mathias and Sander [2021] presented a pseudospectral method for direct and inverse solving of horizontal Richards equation based on the proprietary MATLAB® software. The Boltzmann transformation has also been used in inverse problems of horizontal flow where the saturation profile can be approximated with an analytic function [Evangelides et al., 2010].

Here, it must be noted that the Boltzmann transformation can also be useful combined with standard numerical treatment [Klute, 1952, Philip, 1955, Braddock and Parlange, 1980, Andersen, 2023], resulting in a more efficient (and/or more precise) scheme against traditional numerical methods used for the Richards equation. Notably, such a scheme can obviate the need for time-stepping iterations. Furthermore, it is possible to avoid the requirement of a computational mesh as an input to the program, which makes for a solver easier to use. Moreover, when compared to an approximate analytical method, the numerical approach does not suffer from the incompatibility that appears when diffusivity function gradient tends to infinite under limit conditions for saturation as it was outlined by Hayek [2018].

Table A.1: Summary of different characteristics of the currently available software for solving the Richards equation

Software/algorithm	Open source	Vertical/ 2D/3D	Boltz. transf.	Method	Ref.
Hydrus	No(*)	Yes	No	Finite element	Šimůnek et al. [2016]
COMSOL	No	Yes	No	Finite element	Li et al. [2009]
porousMultiphaseFoam	Yes	Yes	No	Finite volume	Horgue et al. [2022]
PFLOTRAN	Yes	Yes	No	Finite volume	Lichtner et al. [2017]
Pseudospectral method	Yes(**)	No	Yes	Chebyshev diff.	Mathias and Sander [2021]
Fronts	Yes	No	Yes	ODE integr.	Gerlero et al. (This work)

(*) 1D-only public-domain variant of this software has been discontinued.

(**) As implemented in the Julia version of *Fronts*. Originally published as a MATLAB script (op. cit.).

This paper introduces *Fronts* [Gerlero et al., 2020], a numerical tool for solving horizontal cases of the Richards equation with the application of the Boltzmann transformation. As such, *Fronts* is designed to handle problems where the flow occurs along a single axis and the domains may be presumed to be semi-infinite. Built with the goal of being open source, and easier to use and faster than the existing tools that can solve these problems, the software has independent implementations in two different programming languages: Python and Julia, with versions uploaded to the official package registry of each ecosystem. Both variants include the solvers that shall be described later, a set of tutorial cases, and online reference documentation that specifies their usage. The choice of environments reflects current usage trends in scientific computing, with Python being a popular environment for this type of application, while Julia is a newer language with special properties favor its adoption for numerical applications where computation times are an important factor [Bezanson et al., 2017]. *Fronts* can be used both to solve problems in which the underlying hydraulic functions are known, selected from a library of built-in constitutive models, or arbitrarily provided by users; as well as inverse problems in which the parameters of an (also arbitrary) constitutive model are to be found. *Fronts* was developed with the broader community in mind. Besides its expected use in hydrology in general, a more specific application field is identified in paper-based microfluidics, where the Richards equation is now being applied in models of lateral flow assays [Schaumburg et al., 2018b, Asadi et al., 2022].

On the development side, *Fronts* is open source and follows modern software development practices, notably including the use of a continuous integration service with automated test suites for validation.

The paper continues with discussions of the mathematical foundations and the numerical algorithms of *Fronts*. Following that, validation of the software in terms of error calculation from well known analytical solutions is presented, as well as the discussion of some of the numerous tutorial cases that are included with the implementations. Finally, an evaluation of the capabilities of *Fronts* in solving challenging parameter estimation problems is presented. The paper finishes with concluding remarks regarding the benefits and perspectives of this new software.

A.2. Mathematical model and numerical method

A.2.1. Governing equation and Boltzmann transformation

Consider the transient nonlinear diffusion equation along a single axis **r**, which may be written as:

$$\frac{\partial \theta}{\partial t} = \nabla \cdot \left[D(\theta) \frac{\partial \theta}{\partial r} \hat{\mathbf{r}} \right] \tag{A.1}$$

In that expression, θ is a function of position r and time t, and D is a positive function of the range of θ. In general, θ may be called the concentration field and D the diffusivity function.

When the equation is used to model capillary flow in porous media, θ is the moisture content field, and D is known as the moisture diffusivity function, a constitutive relation that takes its expression from unsaturated flow models, with adjustable parameters that are fit to the results of certain experiments. Widely adopted constitutive relations for capillary flow are those by Brooks and Corey [1964] and Van Genuchten [1980]—implementations of which are already included in the packages—along with more recently developed models such as the LET correlations [Lomeland, 2018]. Also included as part of the packages is the implementation of the novel LETd model for capillary flow, which is a LET-based simplification specially targeted for paper-based microfluidic applications [Gerlero et al., 2022]. The mathematical expressions of these models are covered in the Supplementary Material.

With an appropriate choice of the unit vector $\hat{\mathbf{r}}$, Eq. (A.1) is susceptible to the Boltzmann transformation.[2] The Boltzmann transformation requires the introduction of a new variable ϕ—also known as the Boltzmann variable—, defined as:

$$\phi = r/\sqrt{t}. \tag{A.2}$$

To apply the transformation to the partial differential equation, the partial derivatives in Eq. (A.1) are replaced using the following chain rules:

$$\frac{\partial}{\partial r} = \frac{\partial \phi}{\partial r} \frac{\partial}{\partial \phi} = \frac{1}{\sqrt{t}} \frac{\partial}{\partial \phi} \tag{A.3}$$

$$\frac{\partial}{\partial t} = \frac{\partial \phi}{\partial t} \frac{\partial}{\partial \phi} = -\frac{\phi}{2t} \frac{\partial}{\partial \phi} \tag{A.4}$$

After performing the substitutions, all occurrences of r and t can either be replaced with ϕ or factored out. Expanding all derivatives using the product rule, and with the final restriction that θ be a univariate function of ϕ, the following ordinary differential equation is obtained:

$$-\frac{\phi}{2} \frac{d\theta}{d\phi} = D(\theta) \frac{d^2\theta}{d\phi^2} + \frac{dD}{d\theta} \left(\frac{d\theta}{d\phi} \right)^2 \tag{A.5}$$

[2] From now on, it shall be assumed that $\hat{\mathbf{r}}$ is a Cartesian unit vector. It is also possible to define $\hat{\mathbf{r}}$ to deal with some problems in cylindrical and spherical coordinates; for more details on these problems and alternative applications of the Boltzmann transformation, refer to the Supplementary Material.

A.2.1.1. Initial and boundary conditions

For compatibility with the Boltzmann transformation, the problems governed by Eq. (A.5) are defined in semi-infinite spatial domains as it is shown in Figure A.1. Consequently, the domains will be deemed unbounded toward positive r, and the uniform initial condition:

$$\theta(r, t = 0) = \theta_i \tag{A.6}$$

transforms into the boundary condition at infinity for Eq. (A.5):

$$\lim_{\phi \to \infty} \theta = \theta_i \tag{A.7}$$

The previous initial condition is commonly combined with a Dirichlet boundary condition at $r = 0$, i.e.:

$$\theta(r = 0, t) = \theta_b \tag{A.8}$$

which by Eq. (A.2) transforms to:

$$\theta(\phi = 0) = \theta_b \tag{A.9}$$

Boundary conditions other than Eq. (A.8) are applicable in some particular situations and are also included within the package; these are covered in the Supplementary Material.

A.2.2. Reconstructing the solution

The transformed equation and initial–boundary conditions together define a two-point boundary value problem. Once a solution to this two-point problem has been found, the solution to the original problem can be reconstructed by applying the Boltzmann transformation in reverse. The univariate function θ can be transformed into a function of r and t with Eq. (A.2) so that:

$$\theta(r, t) = \theta(\phi = r/\sqrt{t}) \tag{A.10}$$

Having the derivative $d\theta/d\phi$, the partial derivatives $\partial\theta/\partial r$ and $\partial\theta/\partial t$ can be reconstructed with Eqs. (A.3) and (A.4) respectively.

In many applications, knowing the diffusive flux is also of interest. In a problem of capillary flow, the diffusive flux measures the Darcy velocity of the fluid; as such, the diffusive flux $\mathbf{q}$ can be used as input for solving transport problems [Gerlero et al., 2022]. This quantity can be recovered as:

$$\mathbf{q} = -D\left(\theta\right) \frac{\partial \theta}{\partial r} \hat{\mathbf{r}} = -D(\theta) \frac{1}{\sqrt{t}} \frac{d\theta}{d\phi} \hat{\mathbf{r}} \tag{A.11}$$

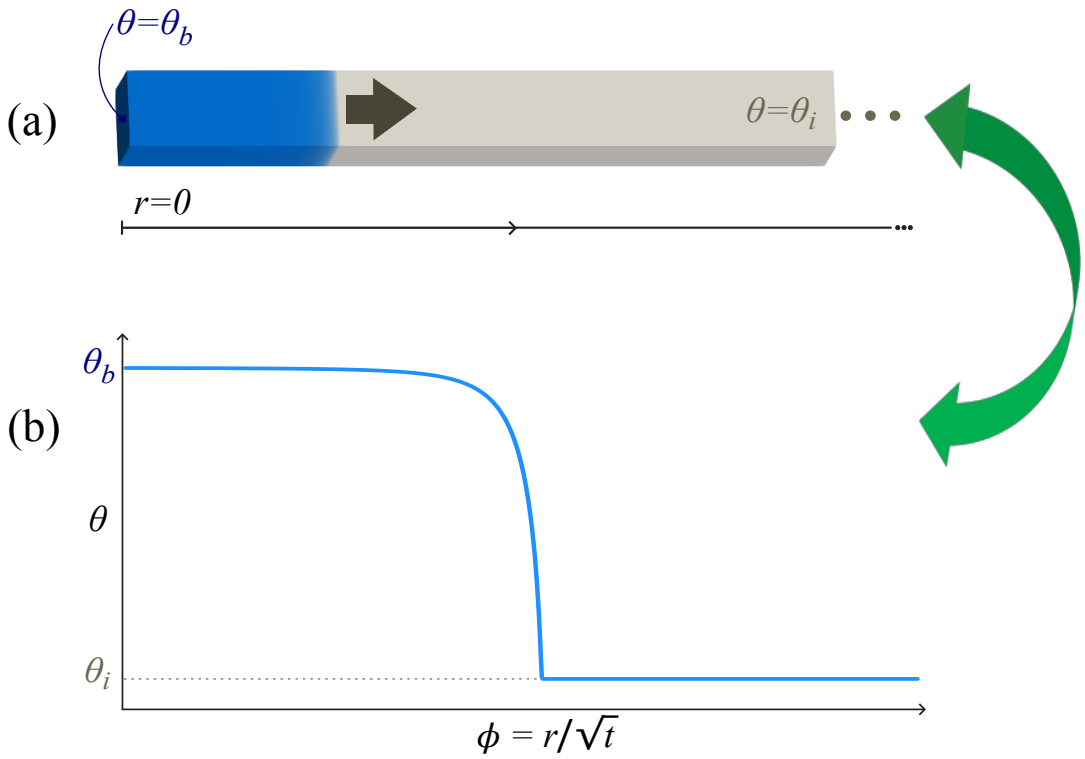

Figure A.1: (a) Initial–boundary value problem in a semi-infinite rectangular domain compatible with the Boltzmann transformation and *Fronts*. (b) Transformation of the solution to the Boltzmann variable.

Another quantity of interest that appears in flow problems is that of sorptivity—defined as the cumulative infiltration per square root of unit time—[Mathias and Sander, 2021], which can also be computed from the solution to the Boltzmann-transformed problem as:

$$S = -2D(\theta)\frac{d\theta}{d\phi} \tag{A.12}$$

where θ and $d\theta/d\phi$ are evaluated at the boundary by convention to obtain a scalar value for the sorptivity S.

A.2.3. Inverse problem

Fronts can also provide solutions to inverse problems of Eq. (A.1) in which the unknown is the function D. This functionality makes use of the integral expression (refer to the Supplementary Material for its derivation):

$$D(\theta) = -\frac{1}{2}\frac{d\phi}{d\theta}\int_{\theta_i}^{\theta}\phi(\theta)\,d\theta \tag{A.13}$$

and may be evaluated without iteration, as long as a sufficiently continuous form of the solution—which appears here as $\phi(\theta)$—is available. In such cases, it can provide a useful $D(\theta)$ function without a dependency on known models. In real cases where the solution is known as discrete data points (with possible uncertainties) and/or under the requirement that D must conform to some known parameterized expression, the practical usefulness of this expression is diminished [Bruce and Klute, 1956], and defining an optimization problem that invokes a direct solver may be a more effective approach.

A.2.4. Numerical implementation

A.2.4.1. Direct solver

In order to solve a problem governed by the moisture diffusion equation, the first step is to convert it into a boundary value problem of Eq. (A.5) using the Boltzmann transformation. Then, the transformed problem is solved numerically with a shooting algorithm in combination with a root finding method.

The default solvers in both the Julia and Python implementations of *Fronts* use Radau IIA implicit numerical integrators of order 5, as implemented by the *DifferentialEquations.jl* [Rackauckas and Nie, 2017] and SciPy [Virtanen et al., 2020] libraries respectively. In practice, this algorithm of numerical integration was found to be the most accurate and robust among the available methods for a variety of tested problems.

It should be noted that derivative evaluations are required in the process of solving Eq. (A.5). In the first place, the derivative $dD/d\theta$ appears directly in such equation and thus will need evaluation. Moreover, the use of an implicit integrator imposes a requirement that derivatives of Eq. (A.5) must also be runtime evaluable (which at the same time implies a second differentiation of D). Derivative calculations are handled differently in each implementation of *Fronts*: in the case of Julia, the package uses forward-mode automatic differentiation [Revels et al., 2016] internally so that required derivatives are evaluated in a manner transparent to the user. However, in the Python package, the required differentiated expressions must be included as part of the implementation, usually obtained with the help of a symbolic engine (except for any function expressions provided by users at runtime, which are differentiated symbolically with the SymPy library [Meurer et al., 2017] just ahead of use). The different approaches reflect the fact that the use of automatic differentiation in Python was determined to be exceptionally expensive in terms of execution times, even after accounting for the overall speed difference that exists across the languages.

At the start of each outer iteration of the solver algorithm, a candidate value needs to be selected for the integrator to use as the free parameter (the derivative at the boundary). With the assumption that this derivative varies continuously with the initial condition, the solver uses the bisection method to select trial values from a search interval. By default, a search interval for the bisection algorithm is found with a heuristic method. This scheme has been found to be very solid in practice; its implementation in *Fronts* adds a few optimizations in order to improve robustness and avoid unnecessary computations. Notably, this rootfinding algorithm is implemented as a coroutine in Julia with the aid of the *ResumableFunctions.jl* package [Lauwens, 2017].

It is important to emphasize that the solvers do not require a starting candidate solution or even a grid of points to be provided by the user as an input. Rather, the discretization of the solution is fully controlled by the automatic step selection of the numerical integrator, which constitutes an advantage in terms of usability and performance.

A.2.4.2. Inverse solver

The inverse solver takes the input function in discrete form, as values of θ on a finite set of points of the Boltzmann variable. Such information can be experimental data of moisture content as a function of time and space [Villarreal et al., 2019]. It first constructs a continuous function ϕ of θ by interpolating the input data as a cubic spline using the PCHIP method [Fritsch and Carlson, 1980]. Subsequently, the diffusivity function D is defined by applying the integral expression of Eq. (A.13).

Whenever the returned diffusivity function is invoked, it computes the values of the required

expressions by evaluating the interpolating spline accordingly—making use of its integral and derivatives when required, so as to conform to the same requirements that the software imposes on built-in and user-defined diffusivity functions. As a result, an inverse solver invocation can be expected to be faster than a direct solver call, as it does not rely on an iterative algorithm. However, it bears the disadvantages of the approach mentioned in Appendix A.2.3.

A.2.4.3. Parameter estimation

Alternatively, an optimization-based parameter estimation strategy can be employed to find values for parameters (including initial and boundary values) for particular expressions of the diffusivity D, as provided for instance by any established (or newly developed) model for capillary flow. This scheme implies the definition of an objective function that itself invokes the direct solver and compares against the desired results. The objective function can then be passed to any optimization package to obtain estimates for the free parameters. Given the substantial performance advantage, the Julia version of *Fronts* is preferred for this type of usage. Indeed, to facilitate this mode of usage, an optimization support module is included in that implementation, which assists the user in creating an appropriate objective function for a particular model, set of free parameters, solver configuration, and arbitrary target data pesults of the first application exampleoints with possible uncertainties. Anticipating the fact that the objective functions will be repeatedly invoked by any chosen optimizer, computational efficiency is of particular relevance in the implementation of this functionality; notably, objective functions constructed from this module are able to fit constant factors in D as part of an inner intermediate stage, which avoids otherwise unnecessary solver invocations [Gerlero et al., 2022] in estimating this common type of parameter.

A.3. Results and discussion

In this section, different cases as validation or application examples are discussed. It is relevant to note that many more example cases are included as part of the packages—due to space constrains, it will cover a subset of those that are considered the most significant for showcasing the broad range of applications of *Fronts*. All reported execution times were measured with the Julia version of the software running on an M1 MacBook Air (Apple Inc., Cupertino, Calif., USA) notebook computer. In order to run *Fronts*, the single requirement is a standard installation of either Julia (version 1.6 or newer) or Python (version 3.7 or newer).

A.3.1. Software validation

In order to validate the software implementation, two particular cases that admit exact analytical solutions—due to the special forms of their diffusivity functions [Philip, 1960]—were solved with *Fronts*. The results show both remarkable numerical precision and low computational costs.

A.3.1.1. Case 1

For the first case, the proposed diffusivity function is:

$$D(\theta) = \frac{m\theta^m}{2}\left(1 - \frac{\theta^m}{m+1}\right), \qquad m > 0. \tag{A.14}$$

where the initial and boundary conditions are $\theta_i = 0$ and $\theta_b = 1$ respectively.

An unusual feature of this case is that, although the wetting front is finite, its derivative at $\phi = 1$ is discontinuous and infinite when approaching from the left. As was demonstrated by Philip [1960], the exact solution for this case is:

$$\theta = (1 - \phi)^{\frac{1}{m}}; \qquad \phi \in [0, 1]. \tag{A.15}$$

For the solution of this case three different values of m are considered, i.e. $m = \{1, 2, 5\}$. Fig. A.2 gathers the results of this case for the different values of m. Fig. A.2 (a) shows the comparison of the analytical solution from Eq. (A.15) and the solution computed with *Fronts*. Fig. A.2 (b) and (c) show the behavior of the error (mean deviation from analytical solution) for the moisture content and sorptivity as a function of solver tolerance (absolute tolerance for θ_i). In both cases, a strong linear dependence can be inferred up to a limit value of the tolerance that was found to be around 10^{-4}; for lower values of such tolerance, the errors behave asymptotically. Finally, Fig. A.2 (d) shows the number of iterations required by solver to obtain a solution within the prescribed tolerance; the log-linear trend shows the clear advantage of the adopted computational implementation. For a fixed tolerance of 10^{-3} (default value in the software), the measured execution times were $m = 1$: 0.4012 ms, $m = 2$: 0.9641 ms, $m = 5$: 2.096 ms; which are comparable to similar results reported by Mathias and Sander [2021] for a pseudospectral method implemented on a proprietary platform.

A.3.1.2. Case 2

In this second case also proposed by Philip [1960] and used for validation of the implementation, the diffusivity function is written as:

$$D(\theta) = \frac{m}{2(m+1)}\left[(1-\theta)^{m-1} - (1-\theta)^{2m}\right], \qquad m > 0. \tag{A.16}$$

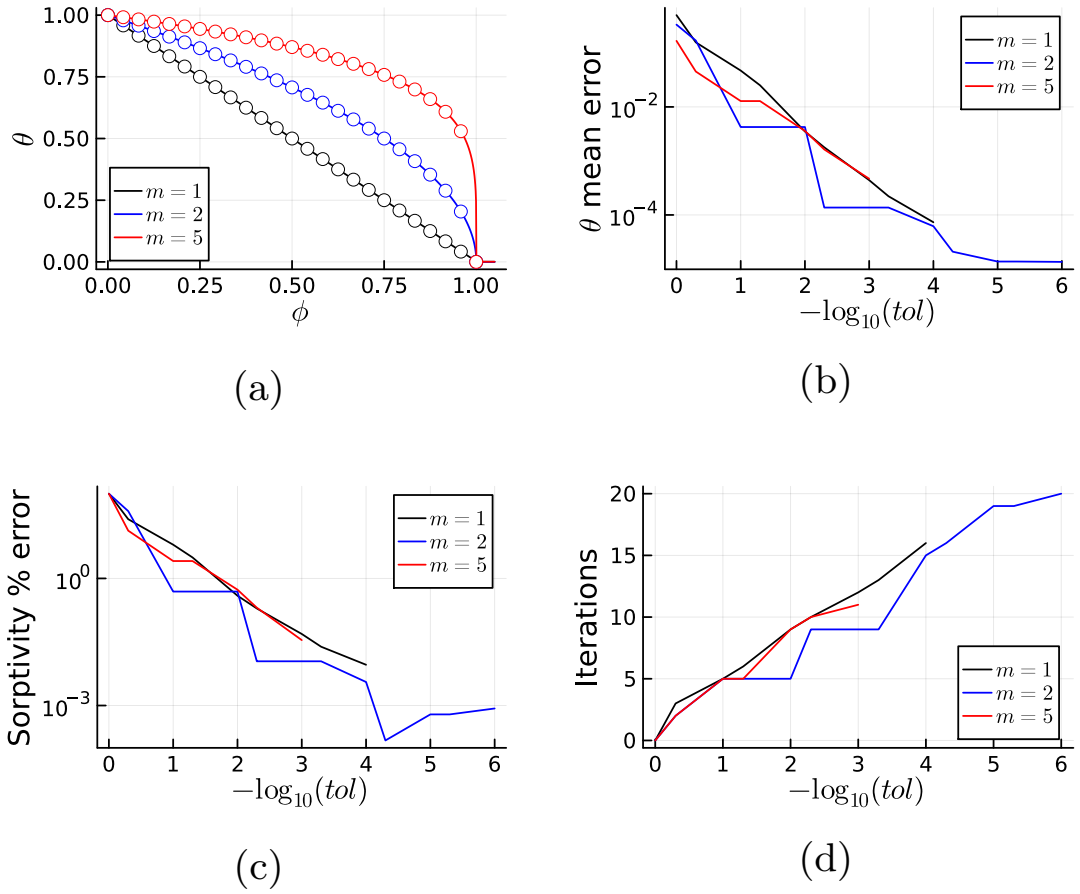

Figure A.2: Validation results of Case 1. (a) Comparison of numerical (circles) and analytical (solid line) solutions; (b) and (c) moisture content (mean absolute) and sorptivity (percent) errors as function of solver tolerance; (d) number of solver iterations as a function of solver tolerance.

where the initial and boundary conditions are once again $\theta_i = 0$ and $\theta_b = 1$.

The particular feature of this case is that the solution θ exhibits an infinite derivative at $\phi = 0$. The exact solution for this case is:

$$\theta = 1 - \phi^{\frac{1}{m}}; \qquad \phi \in [0, 1]. \tag{A.17}$$

For the solution of this second case, four different values of m are considered; i.e. $m = \{1, 2, 5, 10\}$. Fig. A.3 shows the results of the second validation case for the different values of m. Figure A.3 (a) shows the comparison of the analytical solution calculated from equation (A.17) and the numerical solution produced by *Fronts*. Once more, a remarkable agreement between the numerical and analytical solution is observed. Fig. A.3 (b) and (c) show the behavior of the mean error for the moisture content and percent error for sorptivity as a function of the solver tolerance. In both instances, a strong linear dependence can be inferred up to a limit tolerance value that, in

this case, shows a dependency on m for the moisture content error, where a higher m coincides with a greater irreducible error. As for sorptivity, the stagnation error is higher than in Case 1, as was also observed with other methods (Parlange and Braddock [1980], Parlange et al. [1994], as evaluated by Mathias and Sander [2021])—yet notably not with Mathias and Sander [2021]'s own method. Finally, Fig. A.3 (d) shows the number of iterations required to solve the case following the prescribed tolerance. As also occurred with Case 1, the trend here is log-linear, showing once again the advantages of the solver implementation. For the default tolerance of 10^{-3}, the measured computation times were $m = 1$: 0.4147 ms, $m = 2$: 1.778 ms, $m = 5$: 2.725 ms, $m = 10$: 1.877 ms, which are also comparable to those previously reported.

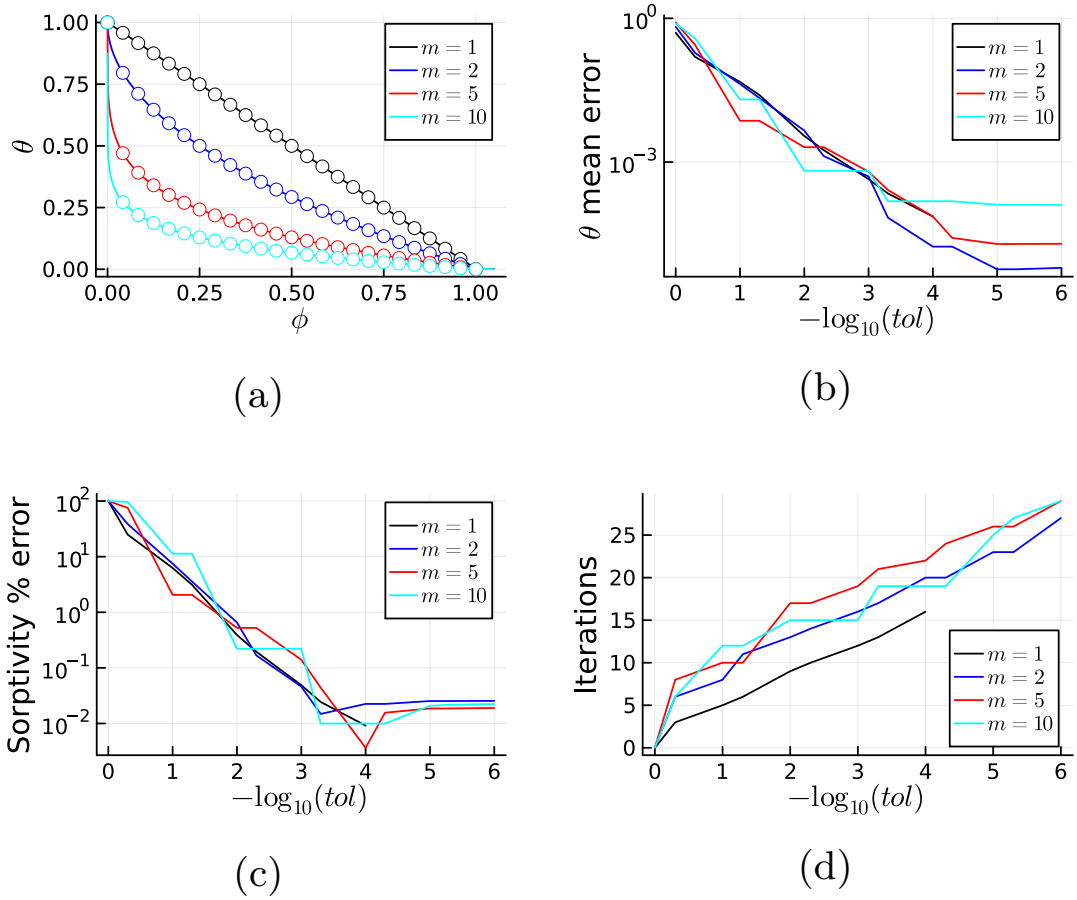

Figure A.3: Validation results of Case 2. (a) Comparison of numerical (circles) and analytical (solid line) solutions; (b) and (c) moisture content (mean absolute) and sorptivity (percent) errors (respectively) as function of solver tolerance; (d) number of solver iterations as a function of solver tolerance.

A.3.2. Application examples

Application examples two of the eight tutorial cases that are included with the implementations of *Fronts* are discussed here. The first is an archetypal example of capillary imbibition with severe ill-conditioning that is known to not be solvable by other methods based on the Boltzmann transformation. Finally, a parameter estimation example based on previously published experimental data of imbibition in filter paper is presented.

A.3.2.1. Direct solving example

For the first application example, a case of capillary imbibition into a porous material with properties described with the Van Genuchten model was selected. It is important to note that no analytical solutions exist for this widely adopted flow model in general nor in this particular example [Hayek, 2018].

This case adopts the parameters for *Grenoble sand* [Fuentes et al., 1992] as listed in Table A.2 along with the initial and boundary conditions, which are set to θ_r (i.e., completely dry medium) and θ_s (fully saturated) respectively. Given that the Van Genuchten diffusivity increases without limit as θ approaches θ_s and evaluates to zero when θ is equal to θ_r, the problem of infiltration into a fully dry medium with this model is intrinsically ill-conditioned and both the initial and boundary conditions have to be treated as asymptotic. Indeed, this case was previously presented by Hayek [2018] as one that could not be correctly solved by application of his approximation method. For its part, *Fronts* is able to produce an accurate solution for this problem within the default tolerance for the initial value and a very small (10^{-7}) absolute tolerance for the boundary value.

Fig. A.4 shows the solution produced by *Fronts* for this case, with the x-axis showing the Boltzmann variable normalized by the constant $\sqrt{D_0}$, where $D_0 = (1 - m)K_s/(\alpha m\theta_s)$. For comparison, also included is the solution obtained for the same problem with a classical numerical approach that considers the full partial differential equation, as implemented in the open-source *porousMultiphaseFoam* toolbox that uses the finite-volume method [Horgue et al., 2022]. Even with this scheme, a tolerance for the initial condition needs to be introduced in order to avoid the ill-conditioning at the limit value. With these allowances, it can be observed that both tools predict equivalent solutions to this problem, with *Fronts* being superior in terms of execution times (a more than tenthousandfold difference) due to its more specialized algorithm.

A.3.2.2. Parameter estimation example

For the final case to cover, experimental data from Gerlero et al. [2022] was used, which studied the capillary imbibition process in Whatman No. 1 paper, a material that is broadly accepted

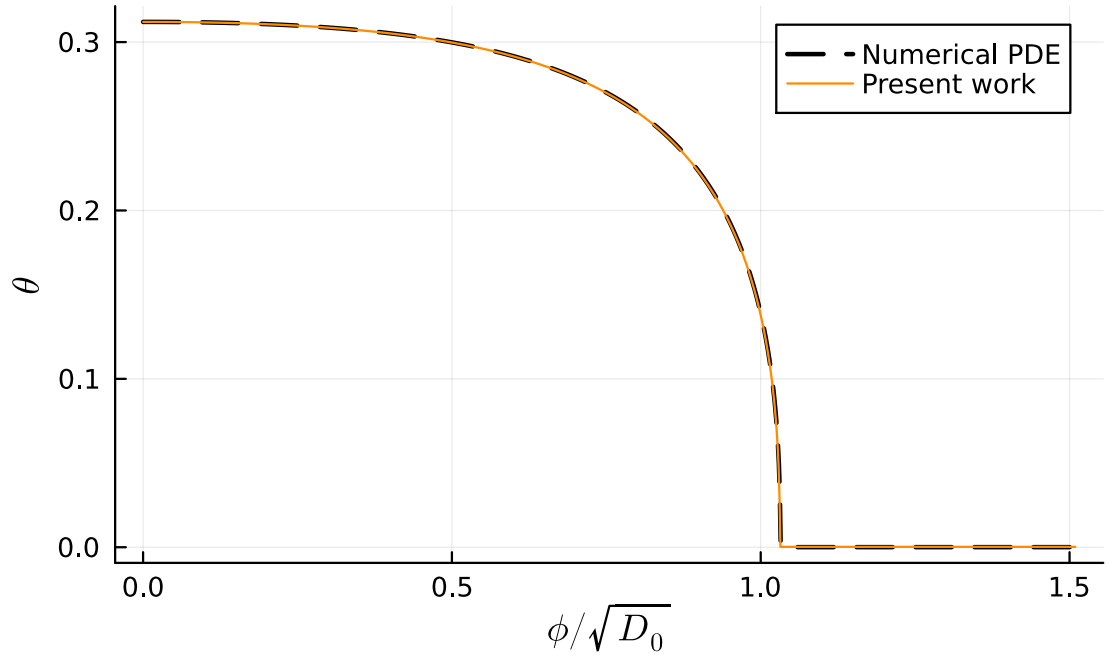

Figure A.4: Results of the first application example. The solid line is the solution produced by *Fronts*, while the dashed line shows the solution obtained with other software (*porousMultiphaseFoam*) that uses a classical numerical approach for the partial differential equation.

Table A.2: Initial–boundary conditions and model parameters for the *Grenoble sand* application example [Fuentes et al., 1992]

Initial condition (asymptotic)	θ_i	0.3120
Boundary condition (asymptotic)	θ_b	0
Van Genuchten parameters	K_s	$15.37\,\mathrm{cm\,h^{-1}}$
	α	$432\,\mathrm{h^{-1}}$
	m	0.5096
	l	0.5
	θ_r,θ_s	$\theta_r = \theta_i$, $\theta_s = \theta_b$

as the most important substrate for paper-based microfluidics. The dataset contains 141 datapoints of moisture content at different values of the Boltzmann variable, each contemplating the experimental uncertainty, that represent the observed wetting profile for this material.

The example cases of parameter estimation included with the package consider two different flow models: Van Genuchten and LETd. It is important to note that this two models were selected for this substrate due to their known potential for describing the imbibition process in this substrate with few parameters; yet a user can arbitrarily choose any of the other implemented models (described in the Supplementary Material) or propose a different one based on their own needs.

The cases follow a similar strategy than in Gerlero et al. [2022], but here adopting the new parameter estimation support module provided by *Fronts*. That module is used to generate an appropriate cost function that is subsequently minimized with an optimizer of the differential evolution family as implemented in the *BlackBoxOptim.jl* [Feldt, 2019] package for Julia.

Table A.3 lists the search intervals and found values of the free parameters for each of the models after allowing the optimization to run for 60 seconds on a single thread, with the fitness measured with the reduced chi-square statistic (χ^2_ν) [Taylor, 1997], which considers the uncertainty in the experimental data (the constant factor parameters fitted by the parameter estimation module as described in Section A.2.4.3). Fig. A.5 (a) compares the solutions found by parameter estimation. Fig. A.5 (b) shows the diffusivity functions corresponding to the fitted models and the diffusivity predicted by the inverse solver (Section A.2.4.2). Both flow models show good agreement with the experimental data in terms of the moisture content profiles, with errors $\chi^2_\nu = 1.6$ and $\chi^2_\nu = 0.9$ for the Van Genuchten and LET models respectively.For their part, the moisture diffusivity curves deviate from each other at low values of θ. The diffusivities estimated via the inverse method are purportedly more representative of the experimental data in this region due to not being constrained by any particular model. Nevertheless, the large discrepancies in the diffusivities

translate to only minor differences in the predicted profiles, which validates the implementation of parameter estimation that considers the predicted profiles in lieu of what would be a far less expensive fitting of the diffusivity models to the results of the inverse solver.

Table A.3: Results of parameter estimation using *Fronts* and the experimental data

Van Genuchten

Parameter	Search interval	Value
K_s/α	(constant factor)	$2.105 \times 10^{-6}\,\mathrm{m^2\,s^{-1}}$
m	$[0.001, 0.999]$	0.8861
l	$[-50, 50]$	2.331
θ_r	$[0, \theta_i]$	$0.005\,623$

LETd

Parameter	Search interval	Value
D_{wt}	(constant factor)	$1.004 \times 10^{-3}\,\mathrm{m^2\,s^{-1}}$
L	$[0, 10]$	1.356
E	$[0, 10^5]$	$10\,010$
T	$[0, 10]$	1.224
θ_r	$[0, \theta_i]$	$0.006\,25$

A.4. Conclusions

This paper introduced *Fronts*, a new software tool for solving nonlinear diffusion problems numerically. To our knowledge, it is the first instance of open-source software that adopts a scheme based on the Boltzmann transformation to solve such problems. Distributed as Julia and Python packages, the implementations includes tutorial cases and reference documentation for the entire set of features. *Fronts* is openly available under the MIT License (Julia) and BSD 3-clause license (Python).

The implementations have been validated in two well-known and challenging cases with analytical solutions. The robustness and capabilities of *Fronts* have also been demonstrated in solving a case with no possible solution when using other methods. At the same time, *Fronts* was shown to also be simpler to use: the main solver has no parameters of numerical origin that need to be set

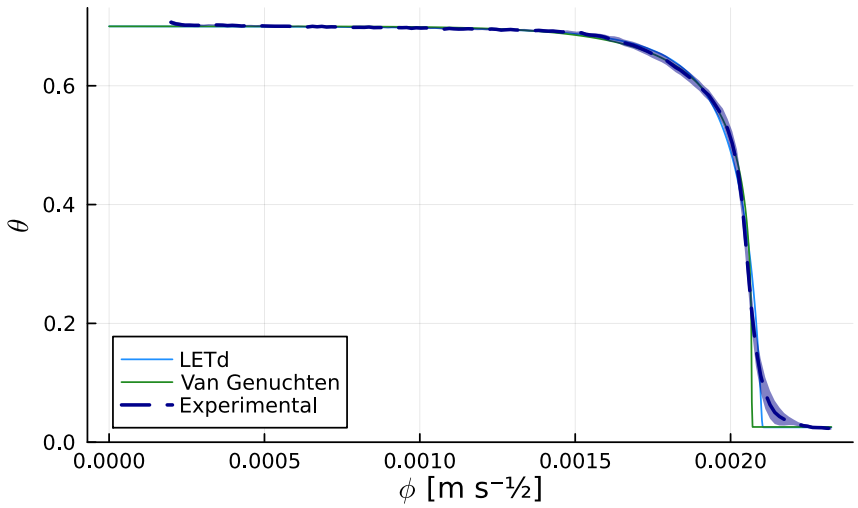

(a)

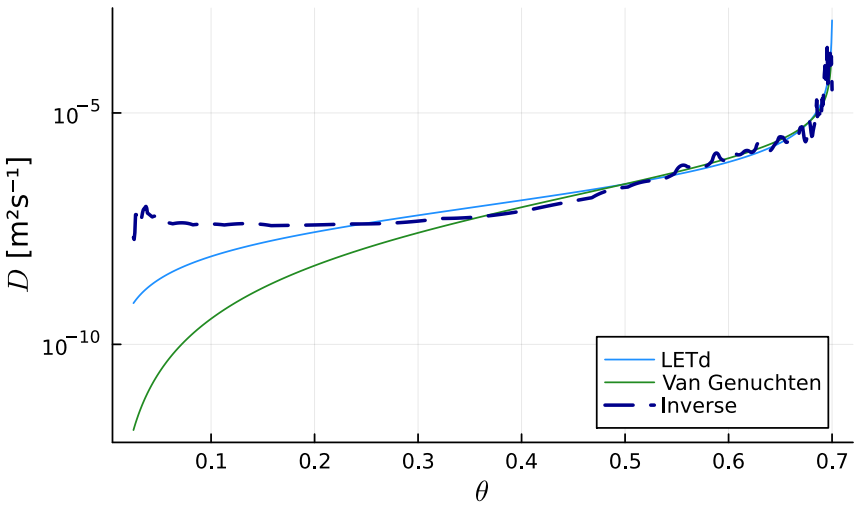

(b)

Figure A.5: Results of the parameter estimation examples considering the Van Genuchten and LETd models. (a) Results of fitting the experimental data with either model (shaded area behind the experimental curve represents the uncertainty in the data); (b) comparison of diffusivities predicted by the fitted models with the results of calling the inverse solver with the experimental data.

or tuned when attempting to solve a case. These facts are once more restated as clear advantages of the approach adopted in *Fronts*.

Direct (predictive) use of the toolbox notwithstanding, *Fronts* has proven to be useful in solving parameter estimation problems through optimization runs—made practicable due its speed, included functionality and ease of automation, as was demonstrated in the imbibition-based characterization of Whatman No. 1 paper.

Moreover, *Fronts* can easily apply arbitrary diffusivity functions defined by users in infiltration problems. The fact that the partial derivatives and diffusive flux of the solution are obtained in continuous form is also notable when reconstructing velocity fields. Furthermore, there is also potential for the toolbox to help with coupled transport problems, in which the diffusive flux from a problem compatible with *Fronts* forms an advection velocity in a different problem. While advection problems obviously fall outside of the scope of the toolbox, having access to *Fronts* in this scenario means that the diffusion problem needs to be solved just once, and the continuous solution passed on to a different solver that itself only needs to deal with the (usually linear) transport problem.

With the release of this work, a positive impact is foreseen in the field of fluid flow in porous media at different scales, ranging from applications in hydrology to paper-based microfluidics, where *Fronts* is expected to help in the study of capillary flow and the development of new processes, techniques and devices.

Acknowledgments

This work was supported by CONICET, Agencia I+D+i [grant number PICT-2018-02920] and UTN [grant numbers PID8132, PID8685], Argentina. The authors acknowledge Prof. Raúl Urteaga and PhD. Andrés R. Valdez for fruitful discussions on the topic of parameter estimation in capillary flow in porous media. The authors declare no competing interest.

Supplementary Material

Supplementary Material is available for this work.

References

K. Alastal and R. Ababou. Moving multi-front (MMF): A generalized Green-Ampt approach for vertical unsaturated flows. *Journal of Hydrology*, 579:124184, 2019.

P. O. Andersen. Insights from Boltzmann transformation in solving 1d counter-current spontaneous imbibition at early and late time. *Advances in Geo-Energy Research*, 7:164–175, 2023.

H. Asadi, M. Pourjafar-Chelikdani, N. P. Khabazi, and K. Sadeghy. Quasi-steady imbibition of physiological liquids in paper-based microfluidic kits: Effect of shear-thinning. *Physics of Fluids*, 34(12):123111, 2022.

J. Bear and A. H.-D. Cheng. *Modeling groundwater flow and contaminant transport*, volume 23. Dordrecht, Netherlands, Springer Science & Business Media, 2010.

J. Bezanson, A. Edelman, S. Karpinski, and V. B. Shah. Julia: A fresh approach to numerical computing. *SIAM review*, 59(1):65–98, 2017.

L. Boltzmann. To integrate the diffusion equation with variable diffusion coefficients. *Annalen der Physik*, 289(13):959–964. (In German), 1894.

R. Braddock and J.-Y. Parlange. Some accurate numerical solutions of the soil-water diffusion equation. *Soil Science Society of America Journal*, 44(3):656–658, 1980.

R. Brooks and T. Corey. Hydraulic properties of porous media. *Hydrology Papers, Colorado State University*, 24:37, 1964.

R. Bruce and A. Klute. The measurement of soil moisture diffusivity. *Soil Science Society of America Journal*, 20(4):458–462, 1956.

D. Caviedes-Voullième, P. García, J. Murillo, et al. Verification, conservation, stability and efficiency of a finite volume method for the 1D Richards equation. *Journal of hydrology*, 480:69–84, 2013.

X. Chen and Y. Dai. An approximate analytical solution of Richards' equation. *International Journal of Nonlinear Sciences and Numerical Simulation*, 16(5):239–247, 2015.

C. Evangelides, G. Arampatzis, and C. Tzimopoulos. Estimation of soil moisture profile and diffusivity using simple laboratory procedures. *Soil Science*, 175(3):118–127, 2010.

M. W. Farthing and F. L. Ogden. Numerical solution of Richards' equation: A review of advances and challenges. *Soil Science Society of America Journal*, 81(6):1257–1269, 2017.

R. Feldt. BlackBoxOptim.jl. `https://github.com/robertfeldt/BlackBoxOptim.jl`, 2022.

F. N. Fritsch and J. Butland. A method for constructing local monotone piecewise cubic interpolants. *SIAM journal on scientific and statistical computing*, 5(2):300–304, 1984.

C. Fuentes, R. Haverkamp, and J.-Y. Parlange. Parameter constraints on closed-form soilwater relationships. *Journal of hydrology*, 134(1-4):117–142, 1992.

G. S. Gerlero, P. A. Kler, and C. L. A. Berli. Fronts.jl. `https://github.com/gerlero/Fronts.jl`, 2022a.

G. S. Gerlero, A. R. Valdez, R. Urteaga, and P. A. Kler. Validity of capillary imbibition models in paper-based microfluidic applications. *Transport in Porous Media*, 141(2):359–378, 2022b.

M. Hayek. An efficient analytical model for horizontal infiltration in soils. *Journal of Hydrology*, 564:1120–1132, 2018.

P. Horgue, F. Renard, G. S. Gerlero, R. Guibert, and G. Debenest. porousMultiphaseFoam v2107: An open-source tool for modeling saturated/unsaturated water flows and solute transfers at watershed scale. *Computer Physics Communications*, 273:108278, 2022.

A. Klute. A numerical method for solving the flow equation for water in unsaturated materials. *Soil Science*, 73(2):105–116, 1952.

W. Lai and F. L. Ogden. A mass-conservative finite volume predictor–corrector solution of the 1D Richards' equation. *Journal of Hydrology*, 523:119–127, 2015.

B. Lauwens. ResumableFunctions: C# sharp style generators for Julia. *Journal of Open Source Software*, 2(18):400, 2017.

Q. Li, K. Ito, Z. Wu, C. S. Lowry, and S. P. Loheide II. COMSOL Multiphysics: A novel approach to ground water modeling. *Groundwater*, 47(4):480–487, 2009.

P. Lichtner, G. Hammond, C. Lu, S. Karra, G. Bisht, B. Andre, R. Mills, and J. Kumar. PFLOTRAN a massively parallel reactive flow and transport model for describing subsurface processes. https://www.pflotran.org/, 2017.

F. List and F. A. Radu. A study on iterative methods for solving Richards' equation. *Computational Geosciences*, 20(2):341–353, 2016.

F. Lomeland. Overview of the LET family of versatile correlations for flow functions. In *Proceedings of the International Symposium of the Society of Core Analysts*, pages SCA2018–056, 2018.

S. A. Mathias and G. C. Sander. Pseudospectral methods provide fast and accurate solutions for the horizontal infiltration equation. *Journal of Hydrology*, 598:126407, 2021.

A. Meurer, C. P. Smith, M. Paprocki, O. Čertík, S. B. Kirpichev, M. Rocklin, A. Kumar, S. Ivanov, J. K. Moore, S. Singh, T. Rathnayake, S. Vig, B. E. Granger, R. P. Muller, F. Bonazzi, H. Gupta, S. Vats, F. Johansson, F. Pedregosa, M. J. Curry, A. R. Terrel, v. Roučka, A. Saboo, I. Fernando, S. Kulal, R. Cimrman, and A. Scopatz. SymPy: symbolic computing in Python. *PeerJ Computer Science*, 3:e103, 2017.

J.-Y. Parlange and R. Braddock. An application of brutsaert's and optimization techniques to the nonlinear diffusion equation: The influence of tailing. *Soil Science*, 129(3):145–149, 1980.

J.-Y. Parlange, D. A. Barry, M. Parlange, D. A. Lockington, and R. Haverkamp. Sorptivity calculation for arbitrary diffusivity. *Transport in porous media*, 15(3):197–208, 1994.

J. Philip. Numerical solution of equations of the diffusion type with diffusivity concentration-dependent. *Transactions of the Faraday Society*, 51:885–892, 1955.

J. Philip. General method of exact solution of the concentration-dependent diffusion equation. *Australian Journal of Physics*, 13:1, 1960.

C. L. Prevedello, J. M. Loyola, K. Reichardt, and D. R. Nielsen. New analytic solution of Boltzmann transform for horizontal water infiltration into sand. *Vadose Zone Journal*, 7(4):1170–1177, 2008.

C. Rackauckas and Q. Nie. DifferentialEquations.jl – a performant and feature-rich ecosystem for solving differential equations in Julia. *The Journal of Open Research Software*, 5(1), 2017.

J. Revels, M. Lubin, and T. Papamarkou. Forward-mode automatic differentiation in Julia. *arXiv:1607.07892 [cs.MS]*, 2016. URL `https://arxiv.org/abs/1607.07892`.

L. A. Richards. Capillary conduction of liquids through porous mediums. *Physics*, 1(5):318–333, 1931.

F. Schaumburg, R. Urteaga, P. A. Kler, and C. L. A. Berli. Design keys for paper-based concentration gradient generators. *Journal of Chromatography A*, 1561:83–91, 2018.

M. Shanmugam, G. S. Kumar, B. Narasimhan, and S. Shrestha. Effective saturation-based weighting for interblock hydraulic conductivity in unsaturated zone soil water flow modelling using one-dimensional vertical finite-difference model. *Journal of Hydroinformatics*, 22(2):423–439, 2020.

L. Su, Q. Wang, X. Qin, Y. Shan, and X. Wang. Analytical solution of a one-dimensional horizontal-absorption equation based on the brooks–corey model. *Soil Science Society of America Journal*, 81(3):439–449, 2017.

J. Sun, Z. Li, F. Furtado, and S. A. Aryana. A microfluidic study of transient flow states in permeable media using fluorescent particle image velocimetry. *Capillarity*, 4(4), 2021.

J. Taylor. *Introduction to error analysis, the study of uncertainties in physical measurements*. University Science Books, Sausalito, US., 1997.

C. Tzimopoulos, C. Evangelides, and G. Arampatzis. Explicit approximate analytical solution of the horizontal diffusion equation. *Soil Science*, 180(2):47–53, 2015.

M. T. Van Genuchten. A closed-form equation for predicting the hydraulic conductivity of unsaturated soils. *Soil Science Society of America journal*, 44(5):892–898, 1980.

R. Villarreal, L. A. Lozano, E. M. Melani, M. P. Salazar, M. F. Otero, and C. G. Soracco. Diffusivity and sorptivity determination at different soil water contents from horizontal infiltration. *Geoderma*, 338:88–96, 2019.

P. Virtanen, R. Gommers, T. E. Oliphant, M. Haberland, T. Reddy, D. Cournapeau, E. Burovski, P. Peterson, W. Weckesser, J. Bright, et al. SciPy 1.0: fundamental algorithms for scientific computing in Python. *Nature methods*, 17(3):261–272, 2020.

J. Šimůnek, M. T. Van Genuchten, and M. Šejna. Recent developments and applications of the HYDRUS computer software packages. *Vadose Zone Journal*, 15(7), 2016.

Anexo B

Validity of capillary imbibition models in paper-based microfluidic applications

El artículo presentado a continuación ha sido publicado en la revista **Transport in Porous Media**.

G. S. Gerlero, A. R. Valdez, R. Urteaga, P. A. Kler. Validity of capillary imbibition models in paper-based microfluidic applications. *Transport in Porous Media*, 141(2):359–378, 2022. `https://doi.org/10.1007/s11242-021-01724-w`

Validity of capillary imbibition models in paper-based microfluidic applications

Gabriel S. Gerlero[1], Andrés R. Valdez[2], Raúl Urteaga[3], Pablo A. Kler[1,4]

[1]Centro de Investigación en Métodos Computacionales (CIMEC, UNL–CONICET), Colectora RN 168 km 472, S3000GLN Santa Fe, Argentina

[2]Computational Modeling Graduate Program, Federal University of Juiz de Fora, Juiz de Fora, MG, Brazil

[3]Instituto de Física del Litoral (IFIS Litoral, UNL–CONICET), Güemes 3450, S3000GLN Santa Fe, Argentina

[4]Departamento de Ingeniería en Sistemas de Información, FRSF-UTN, Lavaise 610, S3004EWB Santa Fe, Argentina

Abstract

Paper-based microfluidics has grown continuously over the last few years. One of the most important characteristics of paper-based microfluidic devices is the ability to pump fluids with the single action of capillary forces. However, fluid flow control in paper-based microfluidic devices has been studied primarily through empirical approaches; and as paper-based microfluidic devices have become more complex, more general and precise models of fluid flow are required. Particularly difficult to model are unsaturated flow conditions, which are critical to the overall performance of paper-based analytical devices, which may contain pre-adsorbed reagents such as indicator particles or antibodies. In this work we propose an objective test and a discussion on the suitability of different models (including a novel model derived here from LET-based models) that represent fluid imbibition dynamics in paper substrates. We reproduce experimental fluid fronts with the best parameter fits of the different models to show their actual capabilities to represent the moisture content function and present an analysis of propagation of uncertainties to obtain a

final objective quantification of the quality of model fits. This objective analysis will endow the paper-based microfluidics community with objective information about modeling tools to improve the designs and performance of these devices.

Keywords: Unsaturated flow, Paper based microfluidics, Imbibition models, Boltzmann transformation, Whatman filter paper.

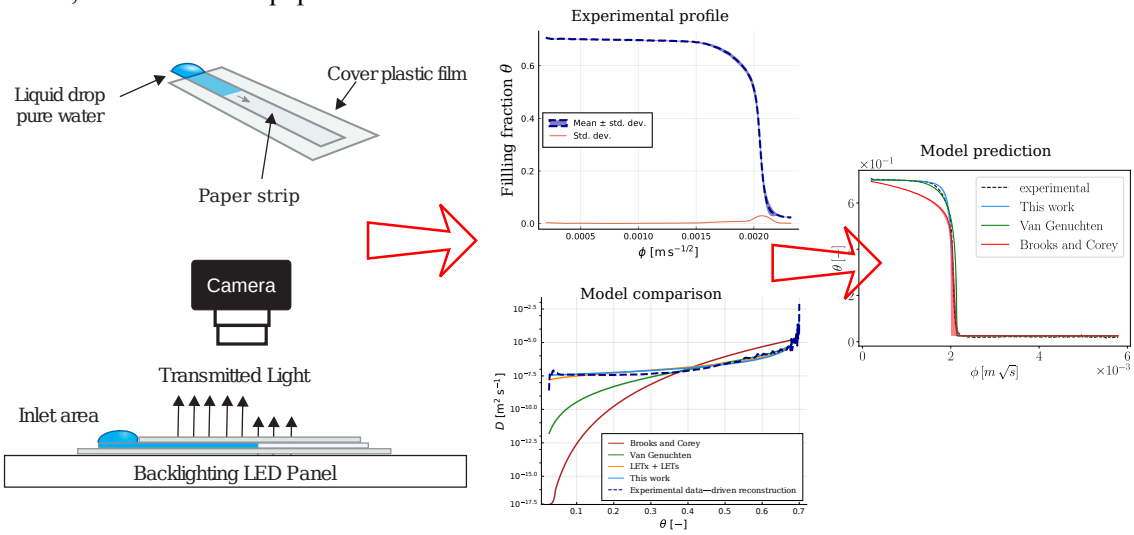

B.1. Introduction

Paper-based microfluidics has grown continuously over the last decade, mainly due to its capabilities for the implementation of portable chemical and biochemical assays [Salentijn et al., 2018]. The advantages offered by paper-based analytical devices have been extensively reported in the literature [Ozer et al., 2020], yet they may be summarized as: low costs of manufacturing, transport, operation (due to small reactant volumes), and final disposal; along with compatibility with different detection methods (sometimes involving mobile devices [Hassan et al., 2020]) that make them easy-to-use by untrained personnel [Kim et al., 2020]. The most important and attractive of all the characteristics of paper-based microfluidic devices is the ability to pump fluids without any external power supply, with the single action of capillary forces due to the wicking nature of cellulose fibers [Modha et al., 2021]. Capillary flow in paper-based microfluidic devices has been exploited since the first works at the beginning of 20th century [Yetisen et al., 2013], later on with the widespread use of lateral flow assays [Berli and Kler, 2016], and recently in more complex applications [Mora et al., 2019]. Especially when considering these recent developments that involve complex multi-layer, multi-step, experimental layouts [Schaumburg and Berli, 2019], an accurate and precise control of the fluid flow is critical.

Unfortunately, fluid flow control in paper-based microfluidic devices has been studied mainly

through empirical approaches due to the following two reasons [Franck et al., 2021]: (i) as mentioned before, manufacturing processes are affordable, and multiple experiments with different layouts and operational conditions can be conducted simultaneously within reasonable timeframes [Yamada et al., 2017]; and (ii), as far as paper is an intricate porous structure of intertwined fibers, predictions of flow behaviors are particularly challenging and, presently, no robust and validated mathematical models are available [Schaumburg et al., 2018b]. This empirical approach has certainly been effective for lateral flow assay configurations and simple devices, but as paper-based microfluidic devices have become more complex, more general and precise models of fluid flow are required [Lim et al., 2019].

At this point, we can discriminate between saturated and unsaturated flow conditions. It is frequent in the paper-based microfluidics community to employ simplified mathematical models of devices operating under saturated flow conditions, i.e. when all the operational domain of the device is completely wet [Schaumburg et al., 2018a]. When saturated flow conditions are assumed, Darcy's Law is sufficient for modeling the flow, with the permeability remaining constant, only pressure boundary conditions are enough to obtain a valid solution for the velocity field [Gerlero et al., 2021]. However, considering a fully saturated domain precludes the local effects of capillarity. Moreover, unsaturated flow conditions are those that are actually critical for the analytical performance of paper-based devices in general, which in many practical cases contain pre-adsorbed reactants such as reporter particles or antibodies (among others) that are transported by the infiltrating fluid front [Rath and Toley, 2020].

Unsaturated flow conditions during imbibition processes are extremely complex and were initially studied by using models based on the Lucas–Washburn Equation [Elizalde et al., 2016, Pan et al., 2021]. Such models are appropriate to determine the position of the wetting front in an averaged manner in the presence of one-dimensional infiltration, but are not capable at all of describing the observable shapes of such fronts, nor can they be applied in two- or three-dimensional domains [Bear and Cheng, 2010]. In order to precisely describe fluid fronts during imbibition processes, the dependence of capillary pressure and permeability with saturation must be adequately accounted for [Santagata et al., 2020]. It is worth noting that it is not only saturation that is important for these applications: the flow velocity field, itself obtained from derivatives of saturation, enables further modeling of scalar transport with convection–diffusion–reaction equations [Gamazo et al., 2016], crucial for the design of paper-based microfluidic analytical devices.

The Richards Equation [Richards, 1931] is the most accepted for describing fluid flow in unsaturated porous media [Hertaeg et al., 2020]. When paper-based microfluidic devices are considered, a special case of the Richards Equation occurs in which gravity can be neglected (due to the usual

positioning of devices and/or the negligible effect of gravity verified through the extremely low Bond numbers andextremely large wetting lengths [Das and Mitra, 2013]. For spontaneous capillary flow, we can reduce the Richards Equation in terms of the volumetric moisture content (θ) to obtain:

$$\frac{\partial \theta}{\partial t} = \nabla \cdot (D(\theta) \nabla \theta) \,. \tag{B.1}$$

This equation is known as the moisture diffusivity equation, and the key condition for the success of this equation as a valid model for imbibition flow is the moisture diffusivity function $D(\theta)$ [Bear and Cheng, 2010]. Hydraulic models for $D(\theta)$ such as those by Brooks and Corey [1964] and by Van Genuchten [1980] provide parametrized closed-form expressions for such function. Details about these models can be found on their original works cited here as well as in the supporting information for this paper.

Adequately solving eq. B.1 can provide an outstanding tool for sensible improvements on the design of complex paper-based microfluidic devices. The success of this numerical process is subject to the usage of a robust and correct model for $D(\theta)$ and the implementation of an efficient numerical tool for solving eq. B.1 with different $D(\theta)$ functions. When defining a robust and correct model for $D(\theta)$, it is important to mention here that the most recognized models (the already mentioned Brooks and Corey [1964] and Van Genuchten [1980] models) were originally developed considering common soil components (e.g. sand, rocks, clay) as substrates. Clearly, the microscopic structure of paper differs from these soil components, so that special considerations may need to be made in order to obtain adequate results from such models. A limited amount of work has been done trying to characterize paper substrates by following these classical soil-oriented models, without reaching consistent and reproducible results [Perez-Cruz et al., 2017, Rath et al., 2018, Rath and Toley, 2020]. The same situation occurred when using other alternative models [Cummins et al., 2017, Ruoff et al., 1959, 1960, Philip, 1955]. An objective test of the suitability of these models for paper-based microfluidic applications is still missing [Terzis et al., 2018].

More recently, an alternative set of correlations has been presented by Lomeland et al. [2005]. These phenomenologically driven models with the name “LET” are targeted towards multiphase fluid flow in soils as well, but also particularly for applications in enhanced oil recovery [Lomeland and Ebeltoft, 2008, Lomeland, 2018]. The large amount of parameters present in the LET models allows for simplifications to produce a new model with fewer parameters compatible with paper-based microfluidic applications. We introduce here a model based on such simplification called “LETd”, whose mathematical foundations can be found in the next section.

In this work, we propose objective testing and a discussion on the suitability of different contemporary $D(\theta)$ models for representing the fluid flow imbibition dynamics in paper substrates. First, we conducted careful experiments to obtain an accurate measure of the imbibition process under controlled conditions. Then, we attempt reproduce these experimental fluid fronts by finding the best parameter fits of the models, showing the actual capabilities of each model to represent the moisture content function $\theta(x,t)$ as a function of space and time. Additionally, an experimental data–driven reconstruction of the $D(\theta)$ function is presented and compared with the $D(\theta)$ function obtained for each model, providing more information about the suitability of the methods for the whole range of θ and the correctness of the assumptions made for the LETd model. Afterwards, we present an analysis on the propagation of uncertainties to characterize the robustness of the models in representing the experimental data under different experimental conditions, and finally we provide an objective quantification of the effect of such uncertainties in the quality of the model fit through an exhaustive (local) error estimation.

Experimental conditions to match the most frequently used in paper-based microfluidics—lateral flow in Whatman No. 1 paper—were chosen. The main result of this work is the confirmation that the LETd model can effectively represent fluid flow imbibition front in the whole range of θ, obtaining more consistent results when compared with classical models, but also offering a more suitable mathematical expression for further modeling of capillary imbibition in more complex domains, including use of the flow velocity field for coupled scalar transport problems. Through this confirmation, the paper-based microfluidics community has new tools to improve designs of contemporary devices as well as to adequately face new challenges in this key technology field.

B.2. Mathematical background

B.2.1. Mathematical description of lateral flow.

For our model problem, we adopt lateral flow conditions[1] in an unsaturated flow problem governed by eq. B.1 as follows: for any coordinate x defined on a semi-infinite one-dimensional spatial domain $(0,\infty)$, find for any instant t in the temporal domain $[0,\infty)$ the moisture content

[1] The set of physicochemical hypotheses of this model is described in the supporting information.

profile $\theta := (x, t) \mapsto \mathbb{R}$ that satisfies the initial–boundary value problem:

$$\begin{cases} \dfrac{\partial\theta}{\partial t} = \dfrac{\partial}{\partial x}\left(D(\theta)\dfrac{\partial\theta}{\partial x}\right), & \text{in } (0,\infty)\times[0,\infty), \\ \theta - \theta_i = 0, & \text{on } t = 0, \quad \text{for any } x \in (0,\infty), \\ \theta - \theta_b = 0, & \text{on } x = 0, \quad \text{for any } t \in [0,\infty). \end{cases} \tag{B.2}$$

By considering θ_i as the initial moisture content and θ_b equal to the porosity θ_s, this problem models the imbibition of a rectangular strip of material in contact with liquid at $x = 0$, i.e. the configuration known as lateral flow in paper-based microfluidics. In practice, θ_b cannot be exactly equal to θ_s because the expressions used for $D(\theta)$ are usually singular at $\theta = \theta_s$ [Bear and Cheng, 2010]. Hence, $\theta_b = \theta_s - \epsilon$ with $\epsilon = 1 \times 10^{-7}$.

B.2.2. Boltzmann transformation.

A convenient property of eq. B.2 is that its solutions are self-similar, and the problem as a whole is susceptible to a similarity transformation known as the Boltzmann transformation [Boltzmann, 1894, Bear and Cheng, 2010]. The transformation means that a solution θ, which is a function of x and t, can also be expressed in terms of a single new variable ϕ—known as the Boltzmann variable—instead, defined as:

$$\phi = \frac{x}{\sqrt{t}}. \tag{B.3}$$

The Boltzmann transformation is useful in many ways. First, it can be applied to experimental observations of lateral flow to reduce the dimensionality of the data. Furthermore, it serves as a verification that eq. B.1 is sufficient for a thorough description of unsaturated flow in the studied material. Finally, it can be leveraged to solve eq B.2 more easily, as it is the case with the numerical tool purposely selected for our analysis [Gerlero et al., 2020].

An additional property of the Boltzmann transformation is that it allows one to obtain $D(\theta)$ from a known differentiable solution to eq. B.2 via the integral expression, effectively solving the inverse problem:

$$D(\theta) = -\frac{1}{2}\frac{d\phi}{d\theta}\int_{\theta_i}^{\theta} \phi \, d\theta. \tag{B.4}$$

This method was first proposed for fluid flow in porous media by Bruce and Klute [1956] and is known as Boltzmann–Matano analysis in the general study of diffusion [Tumidajski and Chan, 1996]. It must be noted that the use of this method alone to solve an inverse problem is generally

limited in precision when θ is known as discrete experimental data [Bruce and Klute, 1956, Cummins et al., 2017] unless the solution is also approximated with an closed-form expression [Espejo et al., 2014, Evangelides et al., 2010, 2005].

B.2.3. Description of the LETd model

Based on the LET family of correlations for special core analysis [Lomeland, 2018], we propose a similar expression to approximate the experimental diffusivity. We define the LETd model as:

$$D(\theta) = D_{wt} \frac{S_{wp}^L}{S_{wp}^L + E(1 - S_{wp})^T}, \tag{B.5}$$

where $S_{wp} = \frac{S_w - S_{wir}}{1 - S_{wir}} = \frac{\theta - \theta_s S_{wir}}{\theta_s - \theta_s S_{wir}}$. D_{wt} (re-scaling factor), L, E, T and S_{wir} are parameters in the LETd model and S_w is defined as the moisture content divided by the material's porosity (see the supporting information for more details).

B.3. Materials and methods

B.3.1. Imbibition experiments

Measurement of initial moisture content. Solving eq. B.2 requires one to know the initial condition in the medium. The initial moisture content in the paper can be estimated by comparing the air-dry and oven-dry weights of the material. For this, paper discs of Whatman No. 1 paper (Whatman grade No. 1, 120 mm discs, Cityva, Marlborough, USA) were initially weighed in ambient conditions. Afterwards, the discs were heated in an oven (KO-30CRS, Buenos Aires, Argentina) at 105 °C. The paper was left to dry overnight and weighed again immediately following removal from the oven. Finally, the discs were weighed once again after 24 hours of being left under ambient conditions.

Lateral flow experiments. Paper-based devices were fabricated using craft-cutting and hot lamination (DASA LM330, DASA SRL, Buenos Aires, Argentina). Rectangular (30 mm × 10 mm) strips of Whatman No. 1 paper were cut along the machine direction. Paper strips were laminated in film pouches (150 µm thick, Binderplus, Santa Fe, Argentina) at 135 °C, at a speed of 3.5 mm s^{-1}. A small section 3 mm in length was left exposed on one side to act as the reservoir for the imbibition. When comparing this lamination strategy with similar setups based on wax printing, the former provides remarkably higher stability for the fluid front flow, avoiding distortions in the shape of

the front caused by the hydrophobic boundaries created in wax-printed channels; as discussed, for example, by Hong and Kim [2015].

The devices were placed horizontally on a surface illuminated with a white backlighting LED panel akin to the one used by Urteaga et al. [2018]. Transmitted light was captured from above by using a high-resolution digital camera (Canon EOS Rebel T5, Canon Inc., Tokyo, Japan) connected to a PC. The camera was positioned vertically 20 cm over the surface and manually focused. Images of the strips with a spatial resolution of about 20 µm per pixel were captured in intervals of 5 seconds.

Deionized water (from an inverse osmosis purifier Osmoion, Apema SRL, Villa Domínico, Argentina) was then deposited on the reservoir of each strip. We took note of the time of start of imbibition on each device to the nearest half second. The devices were then left untouched until the steady state was reached with the paper fully saturated everywhere. In all cases, the first image was captured 5 seconds after the start of imbibition. This time is considerably larger than the timescale involved in the early imbibition regimes reported in the literature [Das et al., 2012]; consequently, such regimes are excluded from the analysis.

Figure B.1**A** shows a diagram of the paper-based devices and experimental setup used for the imbibition experiments. Figure B.1**B** is a composite of images captured during the imbibition of a strip—each 5 seconds apart—, where the effect of moisture content on light transmission can be observed.

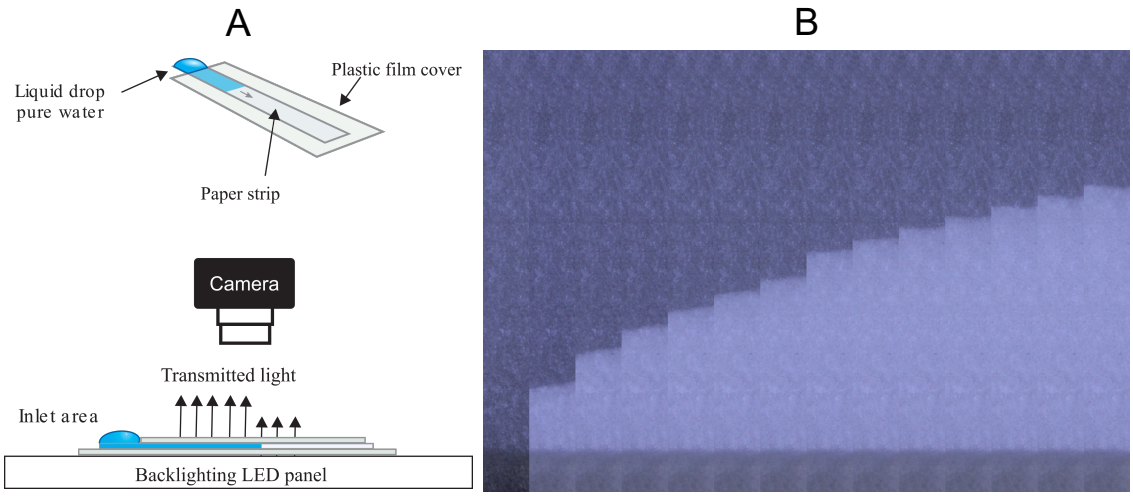

Figure B.1: **A** Diagram of the paper-based devices and experimental setup for the lateral flow experiments. **B** Sequence of images captured during imbibition of single device (images are cropped in width).

Porosity measurements To estimate the porosity, the paper-based devices used in the lateral flow experiments were weighed both before the imbibition and immediately after the experiments—i.e., when still fully saturated and after carefully drying the leftover water in the reservoirs.

Data processing of lateral flow experiments We developed a Python program to analyze the images and extract the equivalent water content profile. To approximate the distribution in moisture content in each strip, we assume a linear relationship between a normalized intensity of transmitted light $\tilde{Y}$ and water uptake in the paper [Urteaga et al., 2019, Vincent et al., 2017]. The experimentally observed moisture content can then be expressed as:

$$\theta^{exp} = \theta_i + (\theta_s - \theta_i)\tilde{Y}, \tag{B.6}$$

so that $\tilde{Y} = 0$ at air-dry conditions ($\theta = \theta_i$) and $\tilde{Y} = 1$ when the paper is fully saturated with water ($\theta = \theta_s$). $\tilde{Y}$ is further defined as:

$$\tilde{Y} = \frac{Y - Y_i}{Y_s - Y_i}, \tag{B.7}$$

where Y represents the intensity of each pixel on the strip as captured in a certain image, Y_i the intensity of that same point in the initial condition, and Y_s is the intensity when fully saturated. All these values are previously normalized by the average intensity of a strip that remains always dry to control any change in ambient lighting between images.

Values of $\tilde{Y}$ in the captured images are then averaged in the direction perpendicular to the flow. Subsequently, and being careful to consider only those images where the wetting front is yet to reach the end of the strip—so that the semi-infinite definition of eq. B.2 holds—, we apply the transformation eq. B.3. We verified that $\tilde{Y}$ values extracted from different images of each strip approximately coincide when expressed in terms of Boltzmann variable ϕ. This observed self-similarity serves as a further confirmation that eq. B.2 can model the physical phenomenon under observation.

We repeated this processing step using the data from lateral flow in three different paper-based devices. We then combined the data from the three experiments, while allowing for a correction factor in ϕ to control for small differences in the overall speed of the imbibition across the different devices [Elizalde et al., 2016] while still capturing the overall shape of the water distribution profiles. In the final step we grouped the datapoints in 141 windows of $15\,\mu\text{ms}^{-1/2}$ in ϕ and used the averages from the three devices to compute the final observed values and standard deviations, the latter after being passed through a uniform filter spanning ten windows.

Experimental data–driven diffusivity reconstruction. The Bruce and Klute method was used to obtain an approximation of the diffusivity function $D(\theta)$ that would explain the experimental data. For this, the experimental average curve was passed through an isotonic regression [Chakravarti, 1989] and subsequently interpolated with a PCHIP [Fritsch and Carlson, 1980] monotonic spline to enable the evaluation of eq. B.4.

B.3.2. Numerical solver and parameter estimation

Parameter estimation was performed by iteratively solving eq. B.2 whilst varying the desired parameters, with the goal of obtaining the best fit to the experimental data as measured with least squares weighted by the uncertainties in the experimental data. Problems were solved with *Fronts* [Gerlero et al., 2020], a specialized numerical package able to find the required solutions to eq. B.2 by taking advantage of the Boltzmann transformation.

The *BlackBoxOptim* [Feldt, 2019] package was used to find values for the unknown parameters by repeatedly invoking the solver and assessing the solutions. For this, a method of the differential evolution family was run in parallel. The optimization is configured to finish after $10\,000$ steps of the differential evolution algorithm, where each step will cause *Fronts* to be invoked at least once.

Exploiting the diffusive nature of the problem, parameters that are constant factors in D (e.g. K_s/α in Brooks and Corey and Van Genuchten, and D_{wt} in LETd) are not explored by the same optimizer. Instead, an intermediate optimization layer is introduced in the process that finds the best constant factor by scaling the solutions in ϕ, which can be done without additional solver calls.

Overall, the scheme turned out to be very efficient, with the entire process of fitting the parameters for the models we examined taking only between 10 and 40 minutes on a MacBook Pro (Apple Inc., Cupertino, Calif., USA) notebook computer equipped with a Core i7-3615QM (Intel Corporation, Santa Clara, Calif., USA) processor and 8 GB of system RAM.

After the optimizer finishes, values of the parameters are rounded to four significant figures for easier reporting and fed again to the solver before computing the reported value of the reduced chi-square (χ^2_ν) statistic [Taylor, 1997].

B.3.3. Estimation and propagation of uncertainties

MCMC for Bayesian Inference. To estimate the uncertainty in the parameters $\mathbf{x} \in \mathbb{R}^{Np}$, a Bayesian framework was employed. More specifically the Markov Chain Monte Carlo (MCMC) method [Brooks, 1998, Brooks et al., 2011] was used to compute the Bayes' rule,

$$\mathbb{P}(\mathbf{x}|D) = \frac{\mathbb{P}(D|\mathbf{x})\,\mathbb{P}(\mathbf{x})}{\mathbb{P}(D)}, \tag{B.8}$$

where for simplicity we consider $D := \theta^{exp}$ obtained from Equation B.6. $\mathbb{P}(D) := \boldsymbol{\sigma}^{exp}$ is referred to as evidence quantifying the variability of the observed data D. $\mathbb{P}(\mathbf{x})$ represents the prior "knowledge" for each model parameter (independently from the data D). $\mathbb{P}(D|\mathbf{x})$ is the likelihood function (revealing the discrepancies between the observed data D and a function of the solution to eq. B.2 evaluated in a fixed sample taken from the distribution of $\mathbf{x}$). Successive computations of eq. B.8 result in a Markov chain that asymptotically converges to the kernel of the density distribution of the uncertain parameter $\mathbf{x}$ that best fit the data D, in other words $\mathbb{P}(\mathbf{x}|D)$. In this manuscript the MCMC was implemented using the Python library `PyMC3`, and adopting the `SLICE` sampler presented in the work of Salvatier et al. [2016].

Emulators vs. simulators. Surrogate models (or emulators) were employed to replace the simulator calls when the number of execution turns not feasible to be performed. In this work Polynomial Chaos Expansions (PCEs) [Nagel and Sudret, 2016, Gratiet et al., 2016] were tailored to obtain the same responses that a simulator can return. In general, PCE emulators map the parameters' uncertainty $\mathbb{P}(\mathbf{x}|D)$, to different Quantities of Interest (QoI) adopting a polynomial structure. For any output quantity $\mathcal{Y}$ the associated PCE emulator is written in terms of a truncated polynomial expansion, yielding the next definition:

$$\mathcal{Y}^{PC} := \sum_{i=0}^{N-1} \boldsymbol{\psi}_i(\mathbf{x})\, y_i, \tag{B.9}$$

where $\boldsymbol{\psi}_i(\mathbf{x})$ represents the orthonormal basis and $\mathcal{Y}^{PC}$ is the approximation of the random response of the QoI. The number of terms N considered in the expansion is a function of the number of uncertain inputs and the polynomial degree P_d given by $N = \frac{(N_p+P_d)!}{P_d!N_p!}$. The coordinates y_i that fix the polynomial expansion written in eq. B.9 are obtained minimizing the difference between $\mathcal{Y}$ and $\mathcal{Y}^{PC}$. The uncertainty quantification will be materialized in the evaluation of statistical moments like the expected value and variance of the QoI. They are computed as:

$$\mathbb{E}[\mathcal{Y}] := \int \mathcal{Y}\, \pi(\mathbf{x}) = y_0, \tag{B.10}$$

$$\mathbb{V}[\mathcal{Y}] := \int (\mathcal{Y} - \mathbb{E}[\mathcal{Y}])^2\ \pi(\mathbf{x}) = \sum_{i>0} {y_i}^2, \tag{B.11}$$

where $\pi(\mathbf{x}) = \prod_i^{N_p} \pi_i(x_i)$, and $\pi_i(x_i)$ is the marginal probability distribution functions (i.e. $\pi_i(x_i) := \mathbb{P}(x_i|D)$). The evaluation of expected value and variance results in simple polynomial operations.

Uncertainty decomposition. Global (variance based) Sensitivity analysis was used to assess how the input parameters $x_i \in \mathbf{x}$ and also interactions between them contribute to a particular output quantity $\mathcal{Y}$, adopting the Sobol sensitivity indices [Sobol, 2001, Saltelli et al., 2008]. The first order Sobol index (also known as main Sobol index), expresses how a certain uncertain input x_i

directly contributes to the variance of the output $\mathcal{Y}$. It is given by the following expression:

$$S_i := \frac{\mathbb{V}[\mathbb{E}[\mathcal{Y}|x_i]]}{\mathbb{V}[\mathcal{Y}]}. \tag{B.12}$$

The first order Sobol index neglects eventual interactions between two or more different uncertain inputs. To estimate the changes on $\mathbb{V}[\mathcal{Y}]$ considering first and high-order interactions of the *i-th* uncertain input, the total Sobol index [Saltelli et al., 2008] is used, which is given by:

$$S_{Ti} := 1 - \frac{\mathbb{V}[\mathbb{E}[\mathcal{Y}|x_{-i}]]}{\mathbb{V}[\mathcal{Y}]}, \tag{B.13}$$

where x_{-i} denotes the set of all inputs except x_i.

In this paper, the computational implementation of the PCE emulators was performed using the Python library `ChaosPy` presented in the work of Feinberg and Langtangen [2015].

B.4. Results and discussion

B.4.1. Experimental results

Initial moisture content. From the oven-drying experiments, we were able to estimate the air-dry volumetric moisture content θ_i of Whatman No. 1 paper at 0.025 ± 0.002. The stability of the obtained results was verified for θ_i within the reported range of uncertainty (0.023–0.027). We note that, in the absence of this consideration, an initial condition of $\theta = 0$ would appear to be a sensible assumption. However, with all of the hydraulic models under study, this condition will result in zero diffusivity and therefore no flow in the domain, a fact that is obviously unrealistic—unless one also accepts negative values for θ_r or S_{wir}, which is unconventional, or is willing to introduce other assumptions [Rath et al., 2018]. By measuring the actual moisture content in air-dry condition, we do not require any of these workarounds.

Porosity. By comparing the initial (air-dry) and saturated weights of the paper-based devices, we measured a porosity of $0.70(6)$. The general methodology of this measurement and its result are in line with those reported by others [Rath et al., 2018, Cummins et al., 2017] for Whatman No. 1 paper, and we will therefore adopt the value $\theta_s = 0.7$.

Lateral flow wetting profile. Experimental data were processed as previously described. Intermediate and final results of data processing appear in Figure B.2. Figure B.2**A** shows the intensity profiles at different times for a single device. Figure B.2**B** displays the final results in water

content versus the Boltzmann variable, plotting the average across the three devices and the standard deviation. The observed self-similarity of profiles at different times is subsequently reflected in the low standard deviations along the final profile.

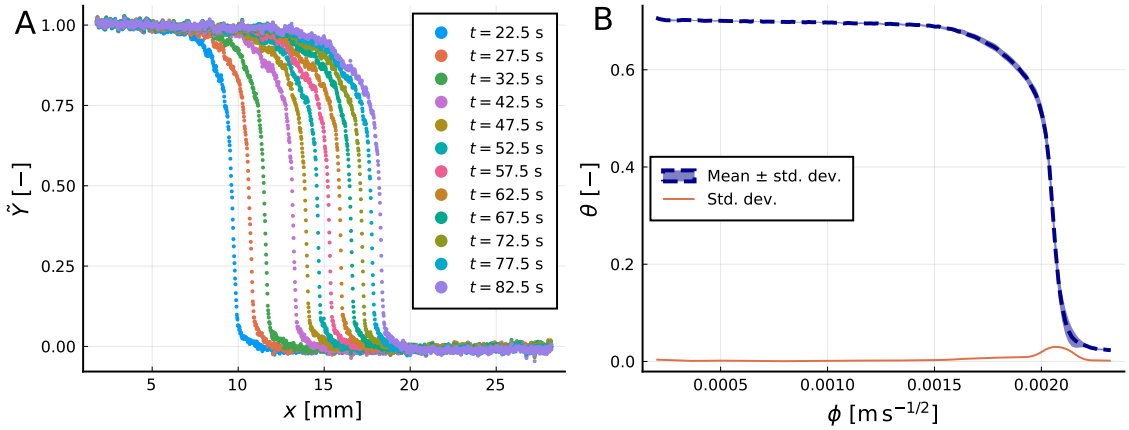

Figure B.2: **A** Intermediate results of data processing in a single paper-based device. **B** Final results of data processing (average water content and standard deviation, expressed in the Boltzmann variable). The low values of standard deviations are a consequence of the self-similarity of the profiles taken at different times.

Parameter estimation. With the experimental wetting profile as the objective, we ran our parameter estimation study to find the best fits that can be obtained with each of the candidate models. These results are reported in Table B.1 and in Figures B.3 and B.4. The figures show, respectively, the wetting profiles and diffusivity functions of the different fitted models compared to the experimental data.

From Figure B.3 it is straightforward to infer that the Brooks and Corey model was unable to match the experimental curve, while the Van Genuchten model is able to reproduce most of the expected profile—but the approximation breaks down with a sharp corner at the transition to initial conditions. In contrast, the LET-based models—both the one based on existing LET correlations as well as our own LETd function with fewer parameters—can approximate the experimental profile very closely at all points.

The reduced chi-square values shown in Table B.1 confirm that Brooks and Corey model is not acceptable, and that LET models yield results that are somewhat better than those obtained with the Van Genuchten model.

The comparison of the diffusivity functions $D(\theta)$ obtained for each model is presented in Figure B.4. These results verify the observations made in Figure B.3, i.e. the LET-based models appear to be better match the reconstructed $D(\theta)$ in the entire domain of θ. For its part, the Brooks

and Corey model only matches the curve twice, and the Van Genuchten model increasingly strays from the experimental $D(\theta)$ as θ goes below 0.4. Analyzing these results, we find it remarkable how LET-based models are able to reproduce $D(\theta)$ well across its whole range of validity. It is also important to note that the differences between the LETx + LETs and LETd models are minor, demonstrating the validity of the considerations made when proposing the LETd model. In light of this, for further analysis we will disregard the LETx + LETs model and consider only LETd, which uses three fewer parameters. Additionally, we used the four obtained $D(\theta)$ functions to predict the flow velocity profiles at different times. The smoothness of the LETd velocity curves should make this model is better posed for coupled scalar transport models with convection–diffusion–reaction equations. These results are reported in the supporting information.

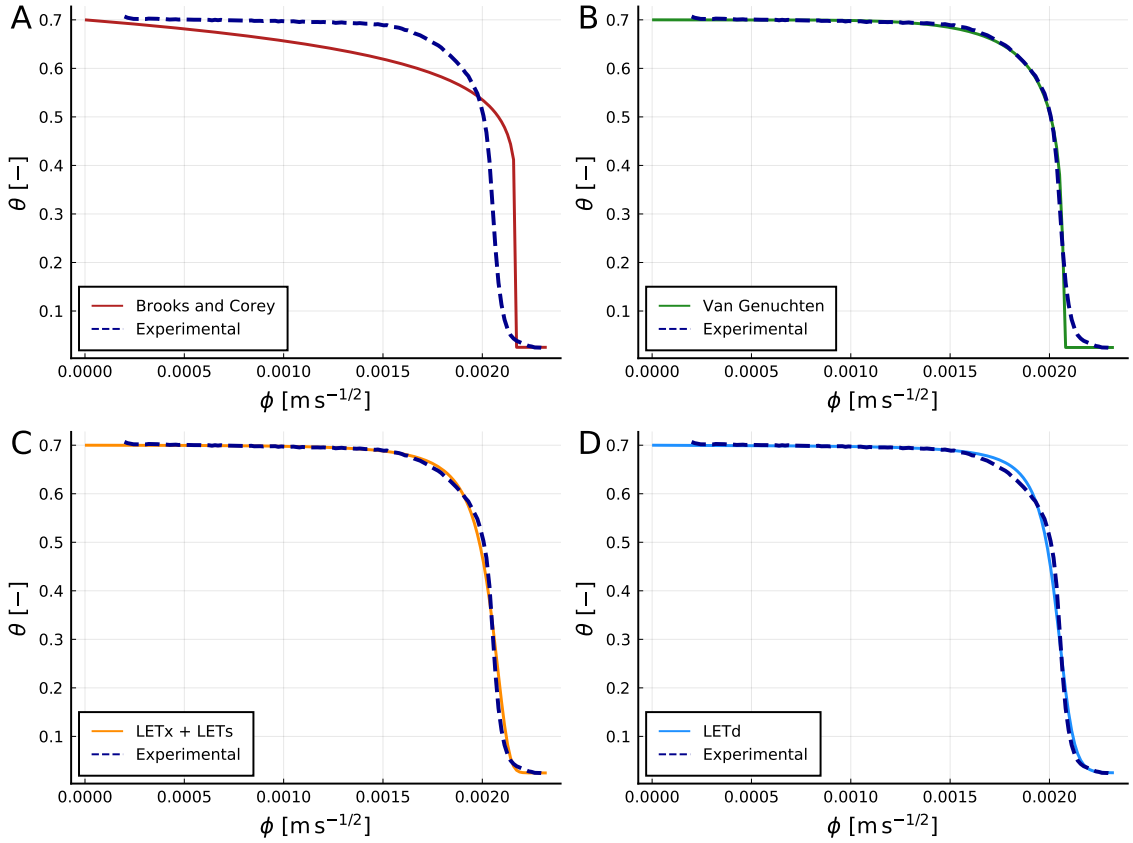

Figure B.3: Best fits of the imbibition profiles represented with the Boltzmann variable for the different models considered in this work.

Finally, in order to demonstrate the applicability of these results in the design and manufacturing of paper-based microfluidic devices, we perform a cross validation experiment on different geometries [Tirapu-Azpiroz et al., 2018]. We constructed different numerical prototypes based on OpenFOAM® [Horgue et al., 2015] using the model parameter sets reported in Table B.1. These numerical prototypes were compared with the experimental results obtained for each geometry.

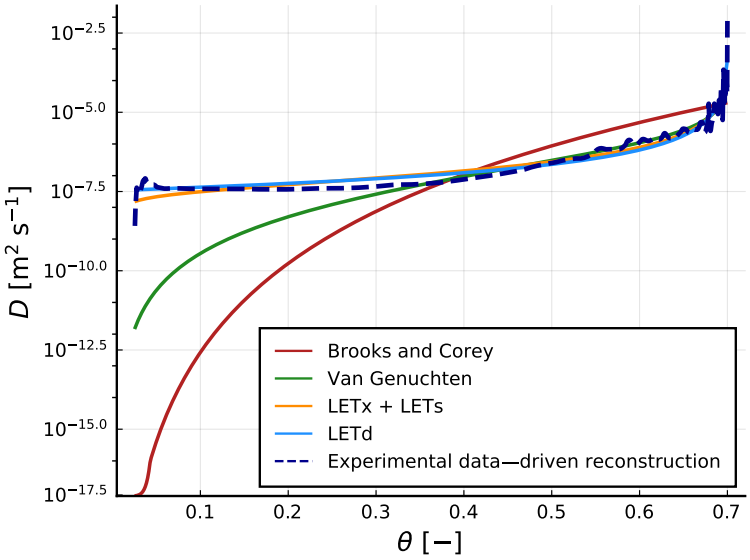

Figure B.4: Comparison of the experimental reconstructed $D(\theta)$ and the diffusivities of the different models with the best fit parameters.

Details and results of this validation step can be found in the supporting information.

B.4.2. Model adjustment considering uncertainty in observed data

Each diffusion model contains parameters with (and without) an associated physical meaning. The uncertain response of the diffusion models is analyzed considering variability on the parameters without physical meaning. In a more general case, we are interested in exposing the difficulties to obtain unique values for the parameters n and l for the Brooks and Corey, and Van Genuchten models. As well as the L, E, T tuple for the LETd model. Taking into account the experimental variability, the MCMC was executed adopting uniform priors for each uncertain input. These uniform priors were upper and lower bounded taking the best fit values reported in Table B.1 allowing total variations of 70% with respect to their nominal value. The execution of the MCMC provided a 20000-long Markov chain for each uncertain parameter. The kernel density estimates are shown in Figures B.5, B.6, and B.7, for the Brooks and Corey, Van Genuchten and LETd models, respectively. The density distribution associated to the Brooks and Corey model presented for both non-physical parameters multi-modal shapes revealing the strong limitations of the model to determine a unique stable pair of n and l, that best fits the experimental data. In particular, we can note that the best fit values reported in Table B.1 have a very small frequency for the n parameter and its rejected in the l density estimate, as shown in Figure B.5.

The Van Genuchten model presented a mixture of density distribution functions, n has a more symmetric distribution than the l parameter. In both cases the best fit values reported in Table B.1

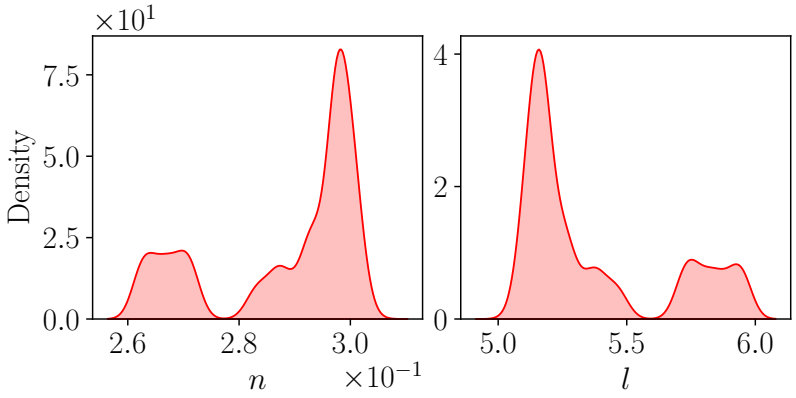

Figure B.5: Posterior distributions for each *Brooks and Corey* non-physical parameters.

were excluded from the posterior density estimates as depicted in Figure B.6. In both cases, the best fit rejection, suggests that the there are many other local minimums that satisfies the fitting requests.

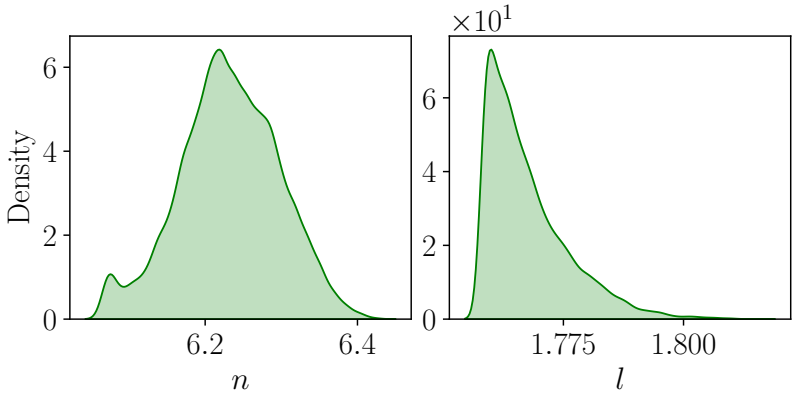

Figure B.6: Posterior distributions for each *Van Genuchten* non-physical parameters.

The samples obtained from the Markov chains considering the LETd model presented asymmetric shapes for the three parameters, and exposed multi-modal density distributions for the E and T parameters. In Figure B.7 the LETd model reduces the probability to recover the best fit value shown in Table B.1 only for the L parameter, while (in contrast to the previous models) for parameters E and T best fit values are contained by the density distributions.

B.4.3. Effects of uncertainties in QoIs

Here, the QoI studied was the $L^2(\Omega)$ error between the experimental observation and the numerical model evaluation performed with *Fronts*, i.e.:

$$L^2(\Omega) = \|\theta^{exp}(\phi) - \theta(\phi)\|_2. \tag{B.14}$$

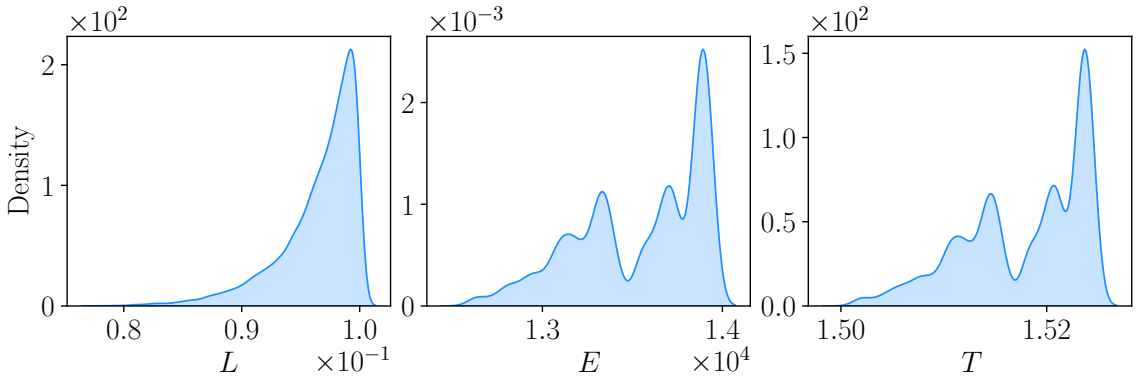

Figure B.7: Posterior distributions for each *LETd* non-physical parameters.

We performed a similar analysis for the absolute error between the experimental observation and the *Fronts* model evaluation, employing the three diffusion models. However, the results are not included here, since they are equivalent to the findings exposed for the $L^2(\Omega)$ error.

The QoI was chosen to evaluate the capabilities of different hydraulic models to reproduce the experimental imbibition fronts in paper substrates. As expected, if a model evaluation returns values near zero for the QoI means that such model have a good capability to recover the experimental observation. Whereas, non-negligible values for the QoI, exposes its limitations. In this manuscript, the PCE emulators were calibrated considering third order polynomials for the Brooks and Corey and Van Genuchten models and a second order polynomial for the LETd model. Additionally, the emulators were adjusted with 300 successful deterministic evaluations. These PCE settings ensure that the error between the simulators and the emulators are small enough to use the emulators. During the calibration of the PCE emulators several failures happened when solving eq. B.2 by drawing samples from the MCMC posterior density distributions. The LETd model had a degree of success of 100%, the Van Genuchten reported an 88% success rate, and the Brooks and Corey had a 43% rate of success. In this context, the LETd model demanded 300 model evaluations to fit the PCE. Whereas, the Van Genuchten and the Brooks and Corey models requested 340 and 693 deterministic evaluations to fit the PCE emulators, respectively.

Figure B.8 shows the estimated uncertainty for each model analyzing the $L^2(\Omega)$ error. The kernel distribution estimate for the analyzed QoI reveals the same non-symmetric and proper shapes for the Brooks and Corey and LETd models certifying that the error estimates are always upper bounded with an abrupt lower threshold. In particular, the Brooks and Corey model had inferior quality response in terms of accuracy and uncertainty propagation. Whereas, the LETd model had better performance in terms of accuracy and uncertainty propagation; the Van Genuchten model presented $L^2(\Omega)$ errors clustered around a unique value revealing almost no uncertain behavior. Yet, the error values where clustered near the worst cases that the LETd model can achieve. In

addition to this, the estimated uncertainty adopting the Van Genuchten model shows a sharp upper-bound with a smooth decay towards smaller values of the $L^2(\Omega)$. This fact exposes that the parametric uncertainty shifted the best fit settings mentioned in Table B.1 to a different minimal configuration.

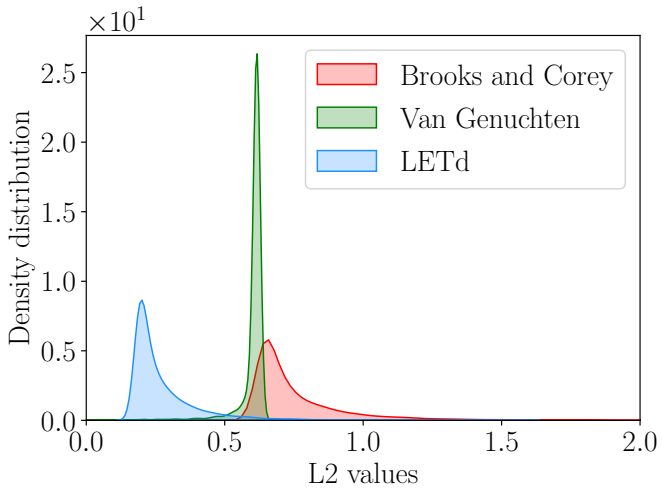

Figure B.8: Comparison between the uncertain response of *Fronts*, considering the Brooks and Corey, Van Genuchten and LETd models with the experimental data

The Table B.2 shows the Sobol indices analyzing the variability of the $L^2(\Omega)$ error, considering the non-physical parameters of each diffusion model. The Brooks and Corey sensitivity analysis states clearly that the variability of the QoI can be reduced by only improving the estimation of the l parameter. A similar sensitivity pattern is recognized on the Van Genuchten Sobol indices. Although the $L^2(\Omega)$ error has small variability adopting the Van Genuchten diffusion model, the Sobol indices reveals that variance reductions are exclusively conditioned to improving the estimation of l. In the case of the LETd model, the $L^2(\Omega)$ variability can be reduced minimizing the fluctuations of the E and T parameters. Moreover, the LETd model presents interactions between the parameters E and T, constraining the variability reduction to appropriate results of E and T.

B.5. Summary and Conclusions

An objective testing and a discussion about the suitability of different contemporary $D(\theta)$ models for representing fluid flow dynamics in paper substrates was presented. We obtain experimental data from carefully designed lateral flow experiments in Whatman #1 paper. The extent and quality of these measurements are evidenced by the excellent results in self-similarity of the profiles, with a very low standard deviation obtained for all the collected data. We reproduced

those experimental fluid fronts with the best parameter fits of the models showing the limitations and capabilities of each model to represent the moisture content function $\theta(\phi)$. We used the *Fronts* solver, which showed remarkable efficiency in solving eq. B.2: over ten thousand invocations for model fitting and twenty thousand invocations for uncertainty quantification, for each model, in less than an hour of total computing time.

Additionally, we presented an adapted model targeted to paper-based microfluidic applications based on LET model, with a reduced number of parameters yet still showing an excellent performance in terms of accuracy and robustness. We demonstrated the favorable characteristics of the LETd model through a data-driven reconstruction of $D(\theta)$ and its comparison with different models. From this study, we conclude that the simplifications made to obtain the LETd model from the original LET-based models do not affect the ability to accurately represent the experimental $D(\theta)$ in the whole domain of θ. This situation cannot be reproduced with the Van Genuchten model for $\theta > 0.4$, nor with the Brooks and Corey model for almost the entire domain of θ. Additional studies were performed with different geometries in order to confirm the validity of the reported model parameters beyond lateral flow, yet also establishing the suitability of the LET-based models to adequately model both fluid front profiles and flow velocity profiles.

An analysis on the propagation of uncertainties allowed us to characterize the robustness of the models for representing the experimental data under different experimental conditions. With the exception of E and T, all deterministic best fit parameters obtained with *Fronts* were not included into the different density distribution associated to the models. Additionally, non-trivial uncertainty propagation was found only with the LETd model. These facts reflect the lack of robustness of the classical models under variations of the experimental data. In other words, when using classical models to fit experimental imbibition data, a small variation of the measured values will produce completely different tuples of ideal parameters, and maybe several of them will show similar fit performances.

Finally, after the presented analysis, it is possible to confirm that LETd model can effectively represent fluid flow imbibition front in the whole range of θ, yielding more robust and reproducible results than classical models when complex contemporary paper-based microfluidic devices are studied.

Declarations

Funding

This research was supported by CONICET, ANPCyT (Grant PICT 2018-02920), UTN (Grant PID ASUTNFE0005525) UNL(Grant CAI+D 50620190100114LI), Argentina and by the Coordenação de Aperfeiçoamento de Pessoal de Nível Superior - Brasil (CAPES) - Finance Code 001.

Conflict of interest

All authors declare complete absence of financial/commercial conflicts of interest.

Data availability

The datasets generated during and/or analysed during the current study are available from the corresponding author on reasonable request.

Supporting information

Supporting information providing formal hypothesis and mathematical definitions for different hydraulic models, as well as results of validation experiments and numerical simulations using the obtained parameter sets on different geometries, can be found in the on-line version of the article.

References

J. Bear and A. H.-D. Cheng. *Modeling groundwater flow and contaminant transport*, volume 23. Springer Science & Business Media, Dordrecht, Netherlands, 2010.

C. L. A. Berli and P. A. Kler. A quantitative model for lateral flow assays. *Microfluidics and Nanofluidics*, 20(7):104, 2016.

L. Boltzmann. Zur Integration der Diffusionsgleichung bei variabeln Diffusionscoefficienten (to integrate the diffusion equation with variable diffusion coefficients). *Annalen der Physik*, 289 (13):959–964, 1894.

R. Brooks and T. Corey. Hydraulic properties of porous media. *Hydrology Papers, Colorado State University*, 24:37, 1964.

S. Brooks. Markov chain Monte Carlo method and its application. *Journal of the royal statistical society: series D (the Statistician)*, 47(1):69–100, 1998.

S. Brooks, A. Gelman, G. Jones, and X. Meng. *Handbook of Markov chain monte carlo*. CRC press, 2011.

R. Bruce and A. Klute. The measurement of soil moisture diffusivity. *Soil Science Society of America Journal*, 20(4):458–462, 1956.

N. Chakravarti. Isotonic median regression: a linear programming approach. *Mathematics of operations research*, 14(2):303–308, 1989.

B. M. Cummins, R. Chinthapatla, F. S. Ligler, and G. M. Walker. Time-dependent model for fluid flow in porous materials with multiple pore sizes. *Analytical Chemistry*, 89(8):4377–4381, 2017.

S. Das and S. K. Mitra. Different regimes in vertical capillary filling. *Physical Review E*, 87(6): 063005, 2013.

S. Das, P. R. Waghmare, and S. K. Mitra. Early regimes of capillary filling. *Physical Review E*, 86(6):067301, 2012.

E. Elizalde, R. Urteaga, and C. L. A. Berli. Precise capillary flow for paper-based viscometry. *Microfluidics and Nanofluidics*, 20(10):1–8, 2016.

A. Espejo, J. V. Giráldez, K. Vanderlinden, E. Taguas, and A. Pedrera. A method for estimating soil water diffusivity from moisture profiles and its application across an experimental catchment. *Journal of Hydrology*, 516:161–168, 2014.

C. Evangelides, C. Tzimopoulos, and G. Arampatzis. Flux-saturation relationship for unsaturated horizontal flow. *Soil science*, 170(9):671–679, 2005.

C. Evangelides, G. Arampatzis, and C. Tzimopoulos. Estimation of soil moisture profile and diffusivity using simple laboratory procedures. *Soil science*, 175(3):118–127, 2010.

J. Feinberg and H. P. Langtangen. Chaospy: An open source tool for designing methods of uncertainty quantification. *Journal of Computational Science*, 11:46–57, 2015. ISSN 1877-7503.

R. Feldt. BlackBoxOptim.jl. `https://github.com/robertfeldt/BlackBoxOptim.jl`, 2019.

N. Franck, F. Schaumburg, P. A. Kler, and R. Urteaga. Precise electroosmotic flow measurements on paper substrates. *Electrophoresis*, 42(7-8):975–982, 2021.

F. N. Fritsch and R. E. Carlson. Monotone piecewise cubic interpolation. *SIAM Journal on Numerical Analysis*, 17(2):238–246, Apr. 1980.

P. Gamazo, L. J. Slooten, J. Carrera, M. W. Saaltink, S. Bea, and J. Soler. Proost: object-oriented approach to multiphase reactive transport modeling in porous media. *Journal of Hydroinformatics*, 18(2):310–328, 2016.

G. S. Gerlero, P. A. Kler, and C. L. A. Berli. Fronts.jl. `https://github.com/gerlero/Fronts.jl`, 2020.

G. S. Gerlero, S. Márquez Damián, F. Schaumburg, N. Franck, and P. A. Kler. Numerical simulations of paper-based electrophoretic separations with open-source tools. *Electrophoresis*, 42: 1543–1551, 2021.

L. L. Gratiet, S. Marelli, and B. Sudret. Metamodel-based sensitivity analysis: polynomial chaos expansions and gaussian processes. *Handbook of Uncertainty Quantification*, pages 1–37, 2016.

S.-u. Hassan, A. Tariq, Z. Noreen, A. Donia, S. Z. Zaidi, H. Bokhari, and X. Zhang. Capillary-driven flow microfluidics combined with smartphone detection: An emerging tool for point-of-care diagnostics. *Diagnostics*, 10(8):509, 2020.

M. J. Hertaeg, R. F. Tabor, J. D. Berry, and G. Garnier. Radial wicking of biological fluids in paper. *Langmuir*, 36(28):8209–8217, 2020.

S. Hong and W. Kim. Dynamics of water imbibition through paper channels with wax boundaries. *Microfluidics and Nanofluidics*, 19(4):845–853, 2015.

P. Horgue, C. Soulaine, J. Franc, R. Guibert, and G. Debenest. An open-source toolbox for multiphase flow in porous media. *Computer Physics Communications*, 187:217–226, 2015.

T. H. Kim, Y. K. Hahn, and M. S. Kim. Recent advances of fluid manipulation technologies in microfluidic paper-based analytical devices (μpads) toward multi-step assays. *Micromachines*, 11(3):269, 2020.

H. Lim, A. T. Jafry, and J. Lee. Fabrication, flow control, and applications of microfluidic paper-based analytical devices. *Molecules*, 24(16):2869, 2019.

F. Lomeland. Overview of the LET family of versatile correlations for flow functions. In *Proceedings of the International Symposium of the Society of Core Analysts*, pages SCA2018–056, 2018.

F. Lomeland and E. Ebeltoft. A new versatile capillary pressure correlation. In *Proceedings of the International Symposium of the Society of Core Analysts*, volume 29, pages SCA2008–08, 2008.

F. Lomeland, E. Ebeltoft, and W. H. Thomas. A new versatile relative permeability correlation. In *Proceedings of the International Symposium of the Society of Core Analysts*, volume 112, pages SCA2005–32, 2005.

S. Modha, C. Castro, and H. Tsutsui. Recent developments in flow modeling and fluid control for paper-based microfluidic biosensors. *Biosensors and Bioelectronics*, page 113026, 2021.

M. F. Mora, C. D. Garcia, F. Schaumburg, P. A. Kler, C. L. Berli, M. Hashimoto, and E. Carrilho. Patterning and modeling three-dimensional microfluidic devices fabricated on a single sheet of paper. *Analytical chemistry*, 91(13):8298–8303, 2019.

J. Nagel and B. Sudret. Spectral likelihood expansions for bayesian inference. *Journal of Computational Physics*, 309:267–294, 2016.

T. Ozer, C. McMahon, and C. S. Henry. Advances in paper-based analytical devices. *Annual Review of Analytical Chemistry*, 13:85–109, 2020.

B. Pan, C. R. Clarkson, M. Atwa, X. Tong, C. Debuhr, A. Ghanizadeh, and V. I. Birss. Spontaneous imbibition dynamics of liquids in partially-wet nanoporous media: Experiment and theory. *Transport in Porous Media*, 137(3):555–574, 2021.

A. Perez-Cruz, I. Stiharu, and A. Dominguez-Gonzalez. Two-dimensional model of imbibition into paper-based networks using Richards' equation. *Microfluidics and Nanofluidics*, 21(5):98, 2017.

J. Philip. Numerical solution of equations of the diffusion type with diffusivity concentration-dependent. *Transactions of the Faraday Society*, 51:885–892, 1955.

D. Rath and B. J. Toley. Modeling-guided design of paper microfluidic networks: A case study of sequential fluid delivery. *ACS sensors*, 2020.

D. Rath, N. Sathishkumar, and B. J. Toley. Experimental measurement of parameters governing flow rates and partial saturation in paper-based microfluidic devices. *Langmuir*, 34(30):8758–8766, 2018.

L. A. Richards. Capillary conduction of liquids through porous mediums. *Physics*, 1(5):318–333, 1931.

A. L. Ruoff, D. L. Prince, J. C. Giddings, and G. H. Stewart. The diffusion analogy for solvent flow in paper. *Kolloid-Zeitschrift*, 166(2):144–151, 1959.

A. L. Ruoff, G. H. Stewart, H. K. Shin, and J. C. Giddings. Diffusion of liquids in unsaturated paper. *Kolloid-Zeitschrift*, 173(1):14, 1960.

G. I. Salentijn, M. Grajewski, and E. Verpoorte. Reinventing (bio) chemical analysis with paper. *Anal. Chem.*, 90(23):13815–13825, 2018.

A. Saltelli, M. Ratto, T. Andres, F. Campolongo, J. Cariboni, D. Gatelli, M. Saisana, and S. Tarantola. *Global sensitivity analysis. The primer*, volume 304. John Wiley & Sons Ltd., 01 2008.

J. Salvatier, T. Wiecki, and C. Fonnesbeck. Probabilistic programming in python using pymc3. *PeerJ Computer Science*, 2:e55, 2016.

T. Santagata, R. Solimene, G. Aprea, and P. Salatino. Modelling and experimental characterization of unsaturated flow in absorbent and swelling porous media: Material characterization. *Transport in Porous Media*, 134(3):725–753, 2020.

F. Schaumburg and C. L. A. Berli. Assessing the rapid flow in multilayer paper-based microfluidic devices. *Microfluidics and Nanofluidics*, 23(8):98, 2019.

F. Schaumburg, P. A. Kler, and C. L. A. Berli. Numerical prototyping of lateral flow biosensors. *Sensors and Actuators B: Chemical*, 259:1099–1107, 2018a.

F. Schaumburg, R. Urteaga, P. A. Kler, and C. L. A. Berli. Design keys for paper-based concentration gradient generators. *Journal of Chromatography A*, 1561:83–91, 2018b.

I. Sobol. Global sensitivity indices for nonlinear mathematical models and their Monte Carlo estimates. *Mathematics and computers in simulation*, 55(1-3):271–280, 2001.

J. Taylor. *Introduction to error analysis, the study of uncertainties in physical measurements*. 1997.

A. Terzis, G. Yang, I. Zarikos, E. Elizalde, B. Weigand, A. Kalfas, and X. Ding. A temperature-based diagnostic approach for paper-based microfluidics. *Microfluidics and Nanofluidics*, 22(3): 1–6, 2018.

J. Tirapu-Azpiroz, A. F. Silva, M. E. Ferreira, W. F. L. Candela, P. W. Bryant, R. L. Ohta, M. Engel, and M. B. Steiner. Modeling fluid transport in two-dimensional paper networks. *Journal of Micro/Nanolithography, MEMS, and MOEMS*, 17(2):025003, 2018.

P. J. Tumidajski and G. W. Chan. Boltzmann-Matano analysis of chloride diffusion into blended cement concrete. *Journal of Materials in Civil Engineering*, 8(4):195–200, 1996.

R. Urteaga, E. Elizalde, and C. L. A. Berli. Transverse solute dispersion in microfluidic paper-based analytical devices (μPADs). *Analyst*, 143(10):2259–2266, 2018.

R. Urteaga, M. Mercuri, R. Gimenez, M. G. Bellino, and C. L. Berli. Spontaneous water adsorption-desorption oscillations in mesoporous thin films. *Journal of colloid and interface science*, 537:407–413, 2019.

M. T. Van Genuchten. A closed-form equation for predicting the hydraulic conductivity of unsaturated soils. *Soil Science Society of America journal*, 44(5):892–898, 1980.

O. Vincent, B. Marguet, and A. D. Stroock. Imbibition triggered by capillary condensation in nanopores. *Langmuir*, 33(7):1655–1661, 2017.

K. Yamada, H. Shibata, K. Suzuki, and D. Citterio. Toward practical application of paper-based microfluidics for medical diagnostics: state-of-the-art and challenges. *Lab on a Chip*, 17(7): 1206–1249, 2017.

A. K. Yetisen, M. S. Akram, and C. R. Lowe. Paper-based microfluidic point-of-care diagnostic devices. *Lab on a Chip*, 13(12):2210–2251, 2013.

Table B.1: Final results of parameter estimation using *Fronts* and the experimental data.

Model	Parameters		χ^2_ν
Brooks and Corey	n	0.2837	691
	l	4.795	
	θ_r	2.378×10^{-5}	
	K_s/α	$3.983 \times 10^{-6}\,\mathrm{m^2\,s^{-1}}$	
Van Genuchten	n	8.093	1.7
	l	2.344	
	θ_r	0.004 943	
	K_s/α	$2.079 \times 10^{-6}\,\mathrm{m^2\,s^{-1}}$	
LETx + LETs	L_w	1.651	1.0
	E_w	230.5	
	T_w	0.9115	
	L_s	0.517	
	E_s	493.6	
	T_s	0.3806	
	S_{wir}	0.016 80	
	$K_s P_{cir}/\gamma$	$8.900 \times 10^{-3}\,\mathrm{m^2\,s^{-1}}$	
LETd	L	0.004 569	1.5
	E	12 930	
	T	1.505	
	S_{wir}	0.028 36	
	D_{wt}	$4.660 \times 10^{-4}\,\mathrm{m^2\,s^{-1}}$	

Table B.2: Sensitivity analysis results considering the three diffusion models.

Sobol index	Brooks and Corey		Van Genuchten	
Main	$n : 1.29 \times 10^{-3}$	$l : 9.96 \times 10^{-1}$	$n : 7.03 \times 10^{-17}$	$l : 1.00$
Total	$n : 3.26 \times 10^{-3}$	$l : 9.98 \times 10^{-1}$	$n : 3.83 \times 10^{-11}$	$l : 1.00$

Sobol index	LETd		
Main	$L : 1.97 \times 10^{-5}$	$E : 7.76 \times 10^{-1}$	$T : 2.23 \times 10^{-1}$
Total	$L : 2.19 \times 10^{-3}$	$E : 7.75 \times 10^{-1}$	$T : 7.14 \times 10^{-1}$

Anexo C

Numerical simulations of paper-based electrophoretic separations with open-source tools

El artículo presentado a continuación ha sido publicado en la revista **Electrophoresis**.

G. S. Gerlero, S. Márquez Damián, F. Schaumburg, N. Franck, P. A. Kler. Numerical simulations of paper-based electrophoretic separations with open-source tools. *Electrophoresis*, 42(16):1543–1551, 2021. https://doi.org/10.1002/elps.202000315

Numerical simulations of paper-based electrophoretic separations with open-source tools

Gabriel S. Gerlero[1], Santiago Márquez Damián[1,2], Federico Schaumburg[3], Nicolás Franck[1], Pablo A. Kler[1,4]

[1]Centro de Investigación en Métodos Computacionales (CIMEC, UNL–CONICET), Colectora RN 168 Km 472, S3000GLN Santa Fe, Argentina

[2]Departamento de Ingeniería Mecánica, FRSF-UTN
Lavaise 610, S3004EWB Santa Fe, Argentina

[3]Instituto de Desarrollo Tecnológico para la Industria Química (INTEC, UNL–CONICET)
Colectora RN 168 Km 472, S3000GLN Santa Fe, Argentina

[4]Departamento de Ingeniería en Sistemas de Información, FRSF-UTN
Lavaise 610, S3004EWB Santa Fe, Argentina

List of abbreviations:

Keywords: Electroosmotic flow; Electrophoresis; Numerical simulations; Paper-based microfluidics; Finite volume method; High performance computing.

Abstract

A new tool for the solution of electromigrative separations in paper-based microfluidics devices is presented. The implementation is based on a recently published complete mathematical model for describing these kind of separations and was developed on top of the open source toolbox `electroMicroTransport`, based on OpenFOAM®, inheriting all its features as native 3D

EDMSD	Electrophoretically driven mechanical solute dispersion
e-μPADs	Electrophoretic microfluidic paper-based analytical devices
FFIEF	Free-flow isoelectric focusing
FVM	Finite volume method
LE	Leading electrolyte
TE	Trailing electrolyte
pI	Isoelectric point
LFA	Lateral flow analysis
IEF	Isoelectric focusing
ITP	Isotachophoresis
MBE	Moving boundary electrophoresis
PZE	Paper-based zone electrophoresis

problem handling, support for parallel computation, and a GNU GPL license. The presented tool includes full support for paper-based electromigrative separations (including electroosmotic flow and the novel mechanical and electrical dispersion effects), compatibility with a well-recognized electrolyte database, and a novel algorithm for computing and controlling the electric current in arbitrary geometries. Additionally, the installation on any operating system is available due to its novel installation option in the form of a Docker image. A validation example with data from literature is included, and two extra application examples are provided, including a 2D free-flow isoelectric focusing problem, that demonstrates the capabilities of the toolbox for dealing with computational and physicochemical modeling challenges simultaneously. This tool will enable efficient and reliable numerical prototypes of paper-based electrophoretic devices to accompany the contemporary fast growth in paper-based microfluidics.

C.1. Introduction

Electrophoretic microfluidic paper-based analytical devices (e-μPADs) have gained relevance in the last years due to the rise of paper-based microfluidic devices, used mainly in point-of-care diagnostics but also in other analytical applications [Salentijn et al., 2018]. The reasons behind this exponential growth of paper-based technologies are extensively discussed in contemporary literature [Gong and Sinton, 2017]—but briefly summarized, the low costs and high potential for their utilization by lowly trained workers in low-resource settings and with remote populations, along with the integration with smartphones and mobile devices, among others, set the right scenario

for this expansion [Schaumburg et al., 2020b]. Paradoxically, paper-based electrophoretic separations were first studied 70 years ago, with the pioneer works from Arne Tiselius on serum protein separation [Cremer and Tiselius, 1950, Kunkel and Tiselius, 1951]. Afterwards, electrophoresis evolved to gel and fused-silica capillaries, and lately to microfluidic chips [Shapiro et al., 1967, Jorgenson and Lukacs, 1981, Ocvirk et al., 2000].

The evolution of contemporary fused-silica capillary-based electrophoresis was accompanied by proper mathematical descriptions of the phenomena involved [Bier et al., 1983], and consequently enriched with consistent numerical methods for a rational prediction of the outcome of experiments and the optimization of operational conditions [Hruška et al., 2006, Thormann et al., 2007, Bercovici et al., 2009]. Such numerical methods were naturally expanded to microfluidic chip applications, offering 3D and high-performance parallel implementations [Márquez Damián et al., 2019, Dovhunová et al., 2020] which still preserve the same mathematical models that describe the physicochemical phenomena: they have not changed any intrinsic experimental condition, but only the geometry of the computational domain.

Despite the aforementioned fact that paper-based electrophoretic separations were already studied 70 years ago, their development was quickly abandoned for two reasons: (i) gel- and capillary-based separations provided more robustness and reproducibility; and (ii) modeling the phenomena on stochastic porous media such as paper was still not possible, and therefore e-µPAD developers lacked a rational tool for the the optimization of devices and experimental conditions [Schaumburg et al., 2018]. The mathematical complexity of these models and the poor reproducibility of the experiments to validate them delayed this process.

With the advent of the new wave of paper-based microfluidics, this scenario has notably changed. On one hand, paper substrates have become industrially more reproducible and some substrates were adopted as standards by the scientific community, such as Whatman #1 paper and nitrocellulose [Mora et al., 2019]. Several electrophoretic separations were reported in the recent literature: for example, paper-based zone electrophoresis (PZE) for amino-acids [Ge et al., 2014] and small inorganic molecules [Xu et al., 2016, Chagas et al., 2016], as well as isotachophoresis (ITP) for increased efficiency of lateral flow analysis (LFA) [Moghadam et al., 2014, Rosenfeld and Bercovici, 2014]. On the other hand, paper substrates have undergone systematic studies in order to obtain reliable mathematical models for a comprehensive description of all of the coupled phenomena that govern the different transport processes [Schaumburg et al., 2020]. Consequently, a reliable numerical tool for numerically prototyping e-µPADs in order to obtain robust models for separation techniques and modes of operation became crucial but strongly attached to the applicability of these mathematical models [Rosenfeld and Bercovici, 2019].

Only a few analytical models of paper-based electrophoretic separations have been reported, limited to one-dimensional channels and the transport of a single chemical compound [Rosenfeld and Bercovici, 2014, 2018], or the binding of an ITP-focused analyte to the reaction zone [Moghadam et al., 2015] on LFA. Regarding more fundamental aspects, mechanical dispersion produced by the fiber network were modeled and experimentally validated [Urteaga et al., 2018]. Other authors derived methodological descriptions for fluid flow [Scales and Tait, 2006, Di Fraia et al., 2018], or transport of chemical species [Shapiro and Probstein, 1993] in porous materials. Recently, a comprehensive model that collects all of these results, but also describes a new effect called electrophoretically driven mechanical solute dispersion (EDMSD), was presented and validated against results from the literature. This model offered the first comprehensive description of the different phenomena and their coupling for porous/tortuous media, such as paper substrates [Schaumburg et al., 2020]. Based on this recent mathematical model, a reliable numerical model of e-μPADs is now possible for the first time. Consequently, this work presents an open-source numerical toolbox with full support for numerical simulations of e-μPADs, based on the aforementioned model [Schaumburg et al., 2020]. To the authors' knowledge this is the first software being able to produce these kind of numerical simulations precisely, as far as it was experimentally validated, but also efficiently due to its computing performance for both serial and parallel runs.

This open-source numerical toolbox is built on top of the existent software `electroMicroTransport` [Márquez Damián et al., 2019], which preserves all its original features for simulating capillary and microchip-based electrophoretic separations, but adds full support for the numerical prototyping of e-μPADs. The `electroMicroTransport` numerical toolbox is based on the OpenFOAM® (*Open-source Field Operation and Manipulation*) platform, a free open-source project for the solution of multiphysics problems based on the finite volume method (FVM) [OpenFOAM. The open source CFD tool, 2019]. OpenFOAM® is developed in the multi-paradigm C++ programming language, and the platform provides key features such as native support for 3D domains, automatic compatibility with parallel computation (which can scale up to supercomputing), a programming syntax for the definition of partial differential equations that resembles their mathematical expressions, and the availability of source code under a GNU GPL license. This latter property has prompted its community to engage in collaborative efforts to extend and improve the software with new models (as is the case with this work) as well as more efficient numerical approaches [Weller et al., 1998].

Besides the novel full support for numerical prototyping of e-μPADs, this extension of `electroMicroTransport` also offers new global features such as a complete electrolyte database

based on the work of Prof. Hirokawa [Hirokawa et al., 1983] (in effect taken from the Simul software [Hruška et al., 2006]), a new algorithm for constant control of the electric current in 2D and 3D domains, and a Docker installation option that enables `electroMicroTransport` to run on any computer regardless of its operating system [Docker. Docker Inc., 2020]. In the next sections, a condensed version of the mathematical model is presented, followed by a description of the scientific contributions of `electroMicroTransport`. Finally, e-μPAD-based application examples are presented with a discussion of their results.

C.2. Mathematical model

The capability of `electroMicroTransport` for numerical prototyping of e-μPADs is based on the mathematical model recently presented by Schaumburg et al. [Schaumburg et al., 2020]. Here, we introduce all the relevant equations in a compact manner, in order to summarize the mathematical fundamentals of the numerical model in terms of partial differential equations, which are the basis of the FVM implementation.

The numerical model shares the physicochemical hypotheses of the original model, i.e.: (i) the porous matrix is modeled as a bundle of tortuous capillaries with variable cross sectional area which are fully saturated; (ii) the geometric dimensions of the substrate are constant throughout the experiments (swelling effects are not taken into account); (iii) evaporation effects are neglected; (iv) a constant temperature is assumed; and (v) retention effects such as adsorption, electrostatic wall forces or hydrophobic/hydrophilic interactions are neglected in the transport of molecules.

After considering the scaling laws for porous media [Scales and Tait, 2006], the equations for the fluid flow can be written as:

$$\begin{aligned} \frac{\tau}{\phi}\frac{\partial \mathbf{u}}{\partial t} + \frac{\tau}{\phi}\mathbf{u}\cdot\nabla\left(\frac{\mathbf{u}}{\phi}\right) &= \frac{\mu}{\rho\tau}\nabla^2\left(\frac{\mathbf{u}}{\phi}\right) - \frac{1}{\rho\tau}\nabla p - [\frac{\rho_e}{\rho\tau}\nabla\Phi + \frac{\mu}{\rho}\frac{\mathbf{u}}{K}]\theta(\Phi) \\ \nabla\cdot\mathbf{u} &= 0 \end{aligned} \tag{C.1}$$

where μ is the fluid viscosity, ρ is the fluid density, ρ_e is the charge density of the electrolyte solution, K is the Darcy's permeability, τ tortuosity, and ϕ the porosity of the medium; while $\theta(\phi)$ is a left Heaviside step function centered at $\phi < 1$. $\mathbf{u}$, p and Φ are the velocity, pressure and electric potential fields respectively. This atypical presentation of the Navier–Stokes equations matches what is actually implemented in the FVM solver. However, it is worth mentioning that not all terms are necessarily different from zero at the same time. For example, in a simple paper strip where boundary conditions on the walls are set to `slip`—and consequently, the inertial and viscous terms are zero—, then eq. (C.1) simplifies to a modified Darcy formulation with the addition of

EOF:

$$\begin{aligned} \frac{\tau\rho}{\phi}\frac{\partial \mathbf{u}}{\partial t} + \frac{1}{\tau}\nabla p + \frac{\rho_e}{\tau}\nabla\Phi = \frac{\mu}{K}\mathbf{u} \\ \nabla\cdot\mathbf{u} = 0 \end{aligned} \tag{C.2}$$

in which the pressure-driven term represents any pressure source, such as capillarity or an external pump that must be included as a boundary condition[1]. When $\theta(\phi) = 0$ (i.e., when $\phi = 1$), eq. (C.1) recovers it usual form for non-porous media and can be used to account for both pressure-driven flow, and/or EOF via the `SmoluchowskyWallVelocity` boundary condition.

In eqs. (C.1) and (C.2), ρ_e is the averaged charge distribution that produces an effective electrically driven fluid flow. The adopted model for such charge density is:

$$\rho_e^p = \frac{\phi\epsilon\zeta}{\tau K} \tag{C.3}$$

where ζ is an equivalent fiber electrokinetic potential, and ϵ is the electrical permittivity of the fluid [Scales and Tait, 2006].

In the case of electrolyte transport, when considering all the different dispersion effects (mechanical and electrical) due to the porous and tortuous nature of paper, the modified transport equation for the concentration of the $j-$electrolyte (c^j) can be written as:

$$\frac{d(c^j\phi)}{dt} = -\nabla\cdot\left(\left(\frac{\mathbf{u}}{\phi} + \frac{\Omega^j}{\tau^2}\nabla\Phi\right)(c^j\phi) - \left(\frac{D^j}{\tau^2} + s_f|\frac{\mathbf{u}}{\phi}| + s_e|\frac{\Omega^j}{\tau^2}\nabla\Phi|\right)\nabla\left(c^j\phi\right)\right) \tag{C.4}$$

where Ω^j represents the electrophoretic mobility of the $j-$electrolyte at the specific (local) pH conditions, D^j is the diffusivity of the $j-$electrolyte, s_f is the mechanical dispersion coefficient, and s_e is the dispersivity of the medium due to EDMSD—i.e., the dispersion produced in the concentration field of a charged species when an electric field is applied.

Finally, determined by the same transport mechanisms, the charge conservation equation that enables the computation of the electric potential Φ is implemented as follows:

$$\nabla\cdot\left(-\frac{\phi}{\tau^2}\sigma\nabla\Phi - F\sum_{j=1}^{N}|z_j|\left(\frac{D^j}{\tau^2} + s_f|\frac{\mathbf{u}_f}{\phi}| + s_e|\frac{\Omega^j}{\tau^2}\nabla\Phi|\right)\nabla(c^j\phi)\right) = 0 \tag{C.5}$$

where F is the Faraday constant, z_j the charge number of the $j-$electrolyte, and N the number of electrolytes. The electrical conductivity σ is calculated as:

$$\sigma = F\sum_{j=1}^{N} z_j^2\frac{\Omega^j}{\tau^2}c^j\phi + \sigma_0 \tag{C.6}$$

[1]When pure EOF is considered, the magnitude of the pressure gradient is negligible, as is the time derivative when the steady state is reached. This yields an even simpler equation with only two terms in total, which represents a Darcy-like formulation for pure EOF.

in which σ_0 accounts for the bias conductivity of the paper substrate through its solid hydrated structure. Experimentally, σ_0 is measured on a paper strip fully saturated with pure water.

C.3. Computational methods

In this section, we summarize all novel computational methods that were developed and included in this new version of `electroMicroTransport` focusing in the numerical prototyping of e-µPADs. We also recount new global features of the software, including Hirokawa's database, and the 3D-compatible constant current algorithm. Technical details about download, installation (traditional and via Docker), and the use of all these new features as well as a step-by-step guide to set up new cases can be found in the user guide presented as supporting information of this paper.

C.3.1. Paper-based electrophoretic separations and electroosmotic flow

As was discussed in previous sections, `electroMicroTransport` offers full support for e-µPADs numerical prototyping. In order to obtain a proper representation of EOF in porous substrates, following the model presented in [Schaumburg et al., 2020], a new body force term in the momentum equation for fluid flow (eq. (C.1)) was introduced. Computationally, the FVM implementation of this term implied the development of new strategies to account for this electrical force in both pressure and velocity formulations. More details on this implementation can be obtained from the source code in `UEqn.H` and `pEqn.H` files.

In order to activate these features, users must set a value for the porosity lower than its default value $\phi = 1$. In practice, this is achieved by setting the `phip` parameter accordingly in the final section of the `constant/ampholyteProperties` file. When `phip` $= 1$, the software will simulate non-porous separations, like classical capillary- or microchannel-based electrophoresis.

In the same file, users can provide different substrate properties, used by `electroMicroTransport` in its implementations of eqs. (C.4–C.6), which require values for physical properties such as tortuosity, Darcy permeability, bias conductivity, and electrokinetic potential. Additionally, mechanical and electrophoretically driven dispersion terms require setting values for the coefficients s_f and s_e. When the user cannot provide reliable values for these parameters, default values are used which match the physical characteristics of Whatman #1 paper [Franck et al., 2021] (summarized in Table C.1), with the aforementioned exception of porosity which must be set to a value lower than 1 (0.7 for Whatman #1) to trigger all e-µPAD features of `electroMicroTransport`.

Physical property	Symbol	Value
Porosity	ϕ	0.7
Tortuosity	τ	2.9
Darcy permeability	K	$0.78\,\mu\text{m}^2$
Mechanical dispersivity	s_f	$50\,\mu\text{m}$
Electrical dispersivity	s_e	$50\,\mu\text{m}$
Electrokinetic potential	ζ	$-15\,\text{mV}$
Bias conductivity	σ_0	$0.2\,\text{mS/m}$

Table C.1: Physical properties of Whatman #1 paper used as defaults in `electroMicroTransport`, with the exception of porosity as described in section C.3.1

C.3.2. Database compatibility and management

The toolbox includes direct access to the electrolyte database originally developed by Prof. Hirokawa [Hirokawa et al., 1983]. It is worth noting that the database included in `electroMicroTransport` is a Python-based adaptation of the database distributed with the Simul and PeakMaster applications [Hruška et al., 2006, Dovhunová et al., 2020].

Consequently, the core of `electroMicroTransport` was modified accordingly in order to take advantage of the additional information contained in this database. The software has been extended to support cases of electrolytes for which the mobility Ω_n of their n-charged state is not exactly the product $n\Omega_{+1}$, where Ω_{+1} is the mobility of the $+1$ charge state of the electrolyte; `electroMicroTransport` accepts different mobility values for different charge states ranging from $+3$ to -3.

The use of this database in the application examples provided along with the code, as well as for setting up new cases, is described in detail in the supporting information.

C.3.3. Constant current support for complex domains

Typically for quantitative ITP, but also in other applications, the applied electric current or current density must be fixed, instead of the electric potential. Because e-μPADs can be arbitrarily shaped, a new algorithm was implemented to handle problems with a constant electric current (or current density), which supersedes other implementations that are valid only for one-dimensional cases.

By using the `uniformCurrentDensity` boundary condition it is possible to prescribe a value for constant current drained from an arbitrary 3D shaped electrode. Consequently, such drained

current I will be calculated as the sum of all the individual currents flowing through all cells adjacent to the electrode surface ($f \in S_e$); i.e.:

$$I = \sum_{f \in S_e} \sigma_f \mathbf{E}_f \cdot \mathbf{S}_f \tag{C.7}$$

where σ_f and $\mathbf{E}_f$ are the conductivity and the electric field at the center of the cell, and $\mathbf{S}_f$ is the (vector) area of the face of the cell in contact with the electrode surface S_e. Hence, by computing the drained current with eq. (C.7), it is possible to iteratively adjust the applied electric potential in order to obtain a proper value of the electric field $\mathbf{E}_f$ that satisfies the prescribed current value. More detailed information about the use of this boundary condition can be found in the supporting information.

C.4. Results and discussion

Three application examples are included to demonstrate software capabilities by covering different e-µPAD applications and computational challenges. This section will discuss such examples in detail. Unless mentioned otherwise, `electroMicroTransport` assumes by default that all the physical properties listed in Table C.1 hold. All these properties were already experimentally [Urteaga et al., 2018, Franck et al., 2021], and numerically validated [Schaumburg et al., 2020]. Pysicochemical properties of all electrolyte components were taken from the database included within the code. Such numerical values are listed in Table C.2. Detailed information on running, modifying, and setting up new cases, can be found in the supporting information.

In order to report computation times, all the presented example cases were run on an Intel® Xeon® CPU E5-1620 v2 3.70GHz (1 CPU x 4 cores), 16 GB (2) Micron 8GB - DDR3 - 1600 Mhz; by using one core for serial simulations and four cores for parallel simulations.

C.4.1. Paper-based zone electrophoresis

The e-µPAD-related features of `electroMicroTransport` were validated against experimental data found in the literature. The experiment, reported in [Atfield and Morris, 1961], consists of a zone electrophoresis separation in a Whatman #3 paper device ($\phi = 0.5$, $\tau = 3.28$). This case is available in the `tutorials/paperBasedZE1` and `tutorials/paperBasedZE2` directories.

In this experiment, an amino acid mixture from a protein lysate is separated using a BGE composed of $252\,\mathrm{mmol\,dm^{-3}}$ pyridine and $158\,\mathrm{mmol\,dm^{-3}}$ histidine ($pH = 5.2$). The device is rather

Component	pK_a	Mobility $\times 10^{-9}$ [m^2 V^{-1} s]	Diffusivity $\times 10^{-9}$ [m^2 s^{-1}]
Acetic acid	4.76	42.4	1.09
Alanine	2.25, 9.86	35.9, 32.2	0.83
Arginine	1.58, 8.92, 12.48	61.0, 25.5, 26.9	0.66
Aspartic acid	1.90, 3.90, 10.0	30.6 ,30.1 ,55.3	0.78
Carrier ampholytes	ΔpK_a 2 (pI 3.5–10.5)	30.0	0.77
Citric acid	3.13, 4.76, 6.40	28.7, 54.7, 74.4	0.74
Glutamic acid	2.14, 4.32, 9.96	28.7, 27.0, 54.3	0.69
Histidine	2.01, 6.04, 9.33	47.50, 26.8, 9.33	0.69
Hydrochloric acid	-	79.1	2.04
Lysine	1.79, 9.13, 10.79	55.1, 28.6, 26.4	0.74
Oxalic acid	1.27, 4.27	42.40, 77.0	1.09
Pyridine	5.18	30.0	0.77

Table C.2: Physicochemical properties for all components included in application examples.

complex from a technical point of view. Different strategies were applied in order to avoid evaporation and temperature rise due to the Joule effect. The main separation paper is 108.5 cm long, 13.5 cm wide Whatman #3 paper. The computational domain, has the same dimensions, and the mesh consists of 10850 cells uniformly distributed in the length direction. The sample is deposited with a micro pipette at 7.5 cm from the left end of the paper. An electric field of 7500 V m^{-1} is applied along the separation channel, which is numerically accomplished (as far as BGE composition is constant in both space and time) by setting the corresponding `fixedValue` boundary condition for the electric potential at 8137.5 V, while the other end of the paper is grounded. First, the cathode is placed on the injection side to separate basic and neutral amino acids (`paperBasedZE1`), and afterwards, in a second experiment, the polarity is reversed to separate acidic amino acids (`paperBasedZE2`).

In order to numerically prototype this experiment, the initial condition for the sample plug is a 1 mm- wide Gaussian distribution placed at the injection position with a 1 mmol dm^{-3} concentration each. BGE components are initially uniformly distributed with the aforementioned concentrations. Constant EOF is considered and calculated from the information given in the original work, it is set to 0.729 µm s^{-1}.This value is based on the fact that the authors reported that neutral

compounds travel between 1.5 cm to 2 cm due to EOF after completing running time of 200 minutes. Consequently, such information was converted into a simulation parameter (EOF velocity) by using the scaling rule presented in [Schaumburg et al., 2020] as follows:

$$u_{eof} = \left(\frac{\Delta L\,\tau}{\Delta t}\right)\left(\frac{\phi}{\tau}\right) = \frac{\Delta L\,\phi}{\Delta t} = \frac{17.5\,\text{mm} \times 0.5}{200\,\text{min}} = 0.729\,\mu\text{m}\,\text{s}^{-1} \tag{C.8}$$

Additionally, two simulation runs were performed by considering free solution conditions for comparison with the experimental and paper-based model results. In order to switch to this classical model $\phi = 1$, $\tau = 1$, $s_f = 0$ and s_e=0 were considered.

Figure C.1A shows the distribution for basic amino acids concentration, the pre-processed experimental data, and the simulation using the free solution model, while Figure C.1B shows the concentrations for acidic amino acids for both numerical and the experimental runs after 200 min. Serial computation time for these examples were 928 s for `tutorials/paperBasedZE1` and 794 s for `tutorials/paperBasedZE2`; while parallel computation times were 295 s and 241 s, respectively.

A good match can be seen for both basic and acidic amino acids, with the chosen set of parameters that represent Whatman #3 paper. The highest error registered is around 1 cm for lysine. Regarding the difference on using the current model and the classical free solution model, the higher dispersion effects, and consequently the different peak shapes are evident. Considering the extremely long experimental time and substrate dimensions the results of the two models are rather similar for practical purposes. However, it is important to note that currently paper-based microfluidic device dimensions and their operational times are reduced more than 10 times compared to this case, and the differences between models are determinant when prototyping such devices as can be seen in [Schaumburg et al., 2020]. Taking into account that the total length of the paper is 108.5 cm, it yields a relative error below 1%.

Image scaling of the experimental results was performed by using the neutral compound displacement provided in the original work, i.e. 1.75 cm. Simulated peak heights were arbitrarily scaled (globally) as far as no information on particular concentration is provided in the original work. It is worth to emphasize that while the original experiment involved a complete protein lysate, for validation purposes, we included here (considering the working pH) one neutral amino acid, two basic, and two acidic. The other amino acids experimental signal were artificially removed from experimental data to adequately construct Figure C.1. The experimental signal was obtained by using ImageJ Software [Schneider et al., 2012] (NIH, Bethesda, MD, USA) by sampling the original figure with the "Plot profile" tool, and averaging in the direction of the strip width. Amino acids not considered in the validation, were replaced by statistically equivalent blank signal obtained from other portions of the image.

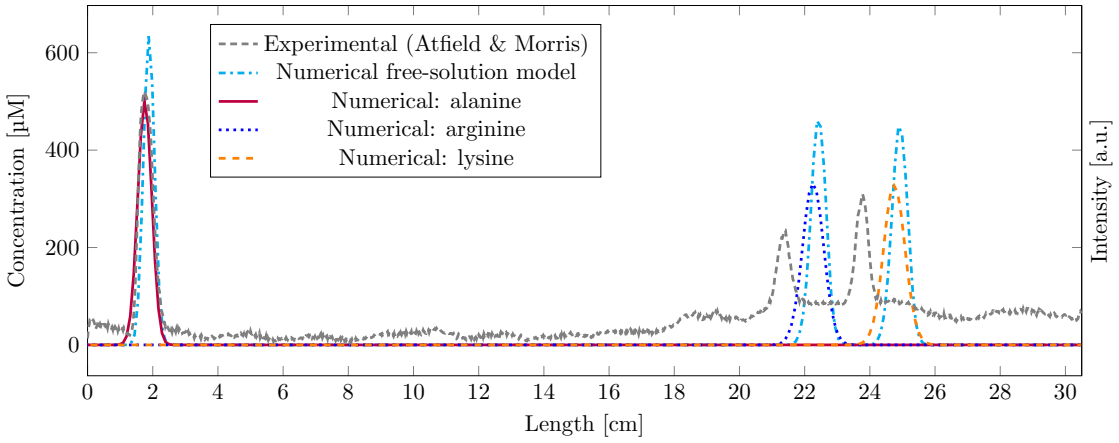

A

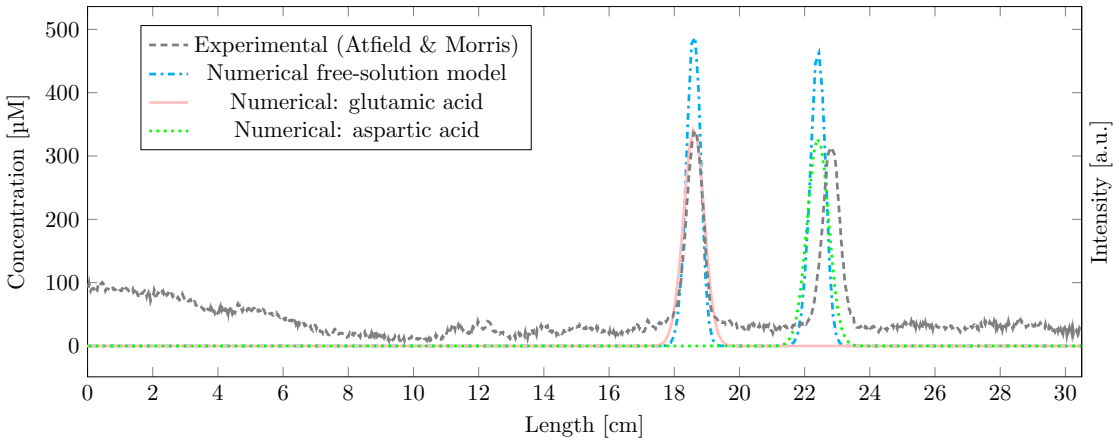

B

Figure C.1: `paperBasedZE1` (**A**), and `paperBasedZE2` (`B`) `application examples from electroMicroTransport` sources. Experimental, free solution, and numerical comparisons of amino acid concentrations measured along distance in the paper substrate after 200 minutes run.

C.4.2. Paper-based moving boundary electrophoresis

In the second application example, a continuous counter-EOF MBE application is presented. Due to the fact that analytes are anions, a negative electric potential difference is applied between the inlet and outlet reservoirs, and consequently, EOF counteracts the migration of anions. This counter-EOF configuration is beneficial as a way to increase the virtual length of the device, increasing separation resolution. Moreover, in some cases it can stop the net migration reaching the theoretical maximum stacking effect for samples [Schaumburg et al., 2020, Rosenfeld and Bercovici, 2018]. This mode of operation configures e-µPADs as excellent tools for analyte preconcentration.

In this application example, citric acid and oxalic acid are concentrated, starting from a sample of $3.12\,\mathrm{mmol\,dm^{-3}}$ and $1.1\,\mathrm{mmol\,dm^{-3}}$ of each in a $30\,\mathrm{mmol\,dm^{-3}}$ acetic acid solution used as TE. LE is $40\,\mathrm{mmol\,dm^{-3}}$ hydrochloric acid, and the counterion (for both LE and TE) is $100\,\mathrm{mmol\,dm^{-3}}$ aniline. The substrate is a Whatman #1 paper strip of 4 cm in length and 1 cm in width. The applied electric potential at the inlet is -400 V for the first case where constant electric potential is applied (`tutorials/paperBasedMBE1`); while for the second case (`tutorials/paperBasedMBE2`) a constant current of $-500\,\mu\mathrm{A}$ is applied. In both cases the outlet is grounded.

A graded mesh of 8000 elements was defined, where the first cell from the left is 25% in length of the last cell at the right in order to improve the resolution of the initial migrations. The electroosmotic flow was modeled by using a constant electrokinetic potential. Such electrokinetic potential, as well as all other paper properties are those reported in Table C.1. Boundary conditions for the top, bottom and lateral walls of the paper were set to `empty`, while inlet and outlet reservoirs were numerically configured with the `inletOutlet` boundary conditions. These conditions keep the initial concentrations of aniline ($100\,\mathrm{mmol\,dm^{-3}}$ at both reservoirs), hydrochloric acid ($40\,\mathrm{mmol\,dm^{-3}}$ at outlet reservoir), and citric, oxalic and acetic acid ($3.12\,\mathrm{mmol\,dm^{-3}}$, $1.1\,\mathrm{mmol\,dm^{-3}}$, and $30\,\mathrm{mmol\,dm^{-3}}$, respectively, at inlet reservoir).

Figure C.2A and B show the concentration profile for LE, TE, and analytes after 600 seconds for constant voltage and constant current, respectively. Computing times for running an 800 s simulation were $34\,102$ s and $12\,643$ s for serial and parallel runs respectively in the case of constant voltage. Similar computational costs were obtained for constant current. Figure C.2C shows the equivalent theoretical conductivity signal measured by a virtual detector placed at 30 mm from the inlet for both experiments. Finally, Figure C.2D shows the fluid velocity due to EOF measured at the outlet, showing a constant value for the case of constant voltage and a linear behavior for the constant current case (until all LE left the paper at 670 s, aproximately) as it can be expected. It is worth to mention that these velocity values are negative, as far as the velocity counteracts migration, i.e. fluid flow is towards left, and these values are recalculated by solving the fluid flow equation at every timestep in both cases. This outlet velocity represents also the velocity on any transverse section of the paper as far as continuity condition is preserved by solving eq.(C.2) at every timestep, which justify the higher computational cost compared to previous example.

C.4.3. Free-flow isoelectric focusing

IEF consists in the separation of amphoteric species based on their isoelectric points through the use of a pH gradient usually generated with a mixture of carrier ampholytes. Thus, IEF experiments require a large number of components [Mosher and Thormann, 2008]. In the case of

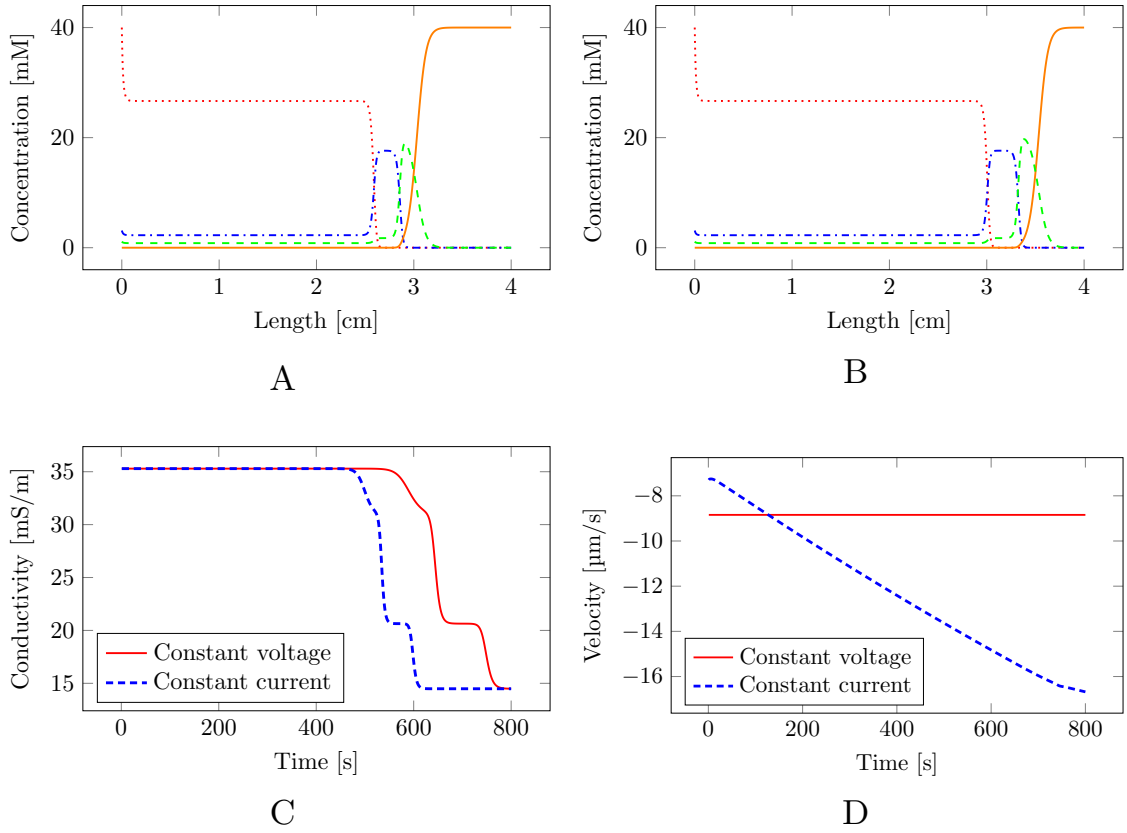

Figure C.2: Concentration profiles for hydrochloric acid (solid orange line), acetic acid (dotted red line), citric acid (dashed-dotted blue line) and oxalic acid (dashed green line), after 600 s under constant voltage (**A**) and constant current (**B**) conditions. **C**. Equivalent theoretical conductivity signals measured in time by a simulated detector placed at 30 mm from the inlet. **D**. Fluid flow velocities due to EOF as a function of time.

free-flow (FF) methods, the electrolytes are injected continuously into a flowing liquid carrier and the electric field is applied perpendicular to the fluid flow direction. In the separation chamber, molecules are deviated from the fluid flow streamlines in the direction of the vector composition of the hydrodynamic and electrophoretic velocities.

In this application example (available in `tutorials/paperBasedFFIEF` directory), the FF and IEF techniques are combined on a paper substrate, which can be extremely useful for analyzing low-conductivity samples [Zhou et al., 2019]. The proposed device is a rectangular separation chamber 15 cm in length (in the direction of fluid flow), and 3.75 cm wide (in the direction of the electric field). In such a chamber, a mixture of 32 carrier ampholytes is continuously introduced via a capillary-driven pump, while a transverse electric potential is applied in order to reach the desired pH gradient on the outlet of the separation chamber. The concentration of carrier ampholytes at the inlet is $1.29\,\mathrm{mmol\,dm^{-3}}$ for each species, while their pIs are uniformly distributed between

3.5 and 10.5.

The FFIEF separation of carrier ampholytes demonstrates the capabilities of the toolbox to deal with different physicochemical effects concurrently. The capillary-driven fluid flow is produced by a capillary pump (i.e., an absorbent pad) connected to the outlet, which produces a continuous fluid flow of 1 mm/s which is set as the inlet boundary condition. Fluid flow problem is solved at the beginning of the solving process and then considered as steady. Simultaneously, fixed value boundary conditions are set at the electrodes, resulting in an 800 V electric potential difference which produces a transverse electromigrative velocity. In Fig. C.3A both fluid flow streamlines and electric field lines are shown. The mesh for this case consists of 78000 cells each with area $0.234\,\mathrm{mm}^2$. Boundary conditions for carrier ampholytes are set to the `inletOutlet` type with an inlet concentration of $1.29\,\mathrm{mmol\,dm}^{-3}$.

Figs. C.3B and C.3C show the pH and conductivity profiles respectively in the separation chamber after 15 min. Computing time for this example was 42 527 s for a parallel run. It can be seen that the conductivity range decreases towards the outlet due to the carrier ampholytes arranging themselves according to their pIs, minimizing their charge. Fig. C.3D shows the concentration of carrier ampholytes and pH profile across the outlet section of the separation chamber. Results obtained are very similar to those of capillary-based separations [Márquez Damián et al., 2019] showing the potential of paper substrates for running self-focusing methods.

C.5. Concluding remarks

A new software based on the `electroMicroTransport` toolbox for the solution of 3D multiphysics problems involving fluid dynamic and electromigrative phenomena in paper substrates was implemented, validated, and publicly released. This original toolbox for e-µPAD numerical prototyping and its related mathematical model were validated against experimental results available in literature. `electroMicroTransport` was implemented on top of the OpenFOAM® platform, and therefore contains built-in support for 3D problems and parallel computation, and has its source code open under a GPL license. To authors' knowledge this is first toolbox to show validated and efficient computational capabilities for the numerical protoyping of e-µPADs.

`electroMicroTransport` offers a number of novel characteristics that makes it particularly interesting for the electrophoresis community, namely: (i) full e-µPADs support, including EOF and novel mechanical and electrical dispersion effects, implemented numerically for the fist time; (ii) full compatibility with the most recognized electrolyte database for electrophoretic separations; (iii) an original and robust algorithm for constant current computation and control, compatible with

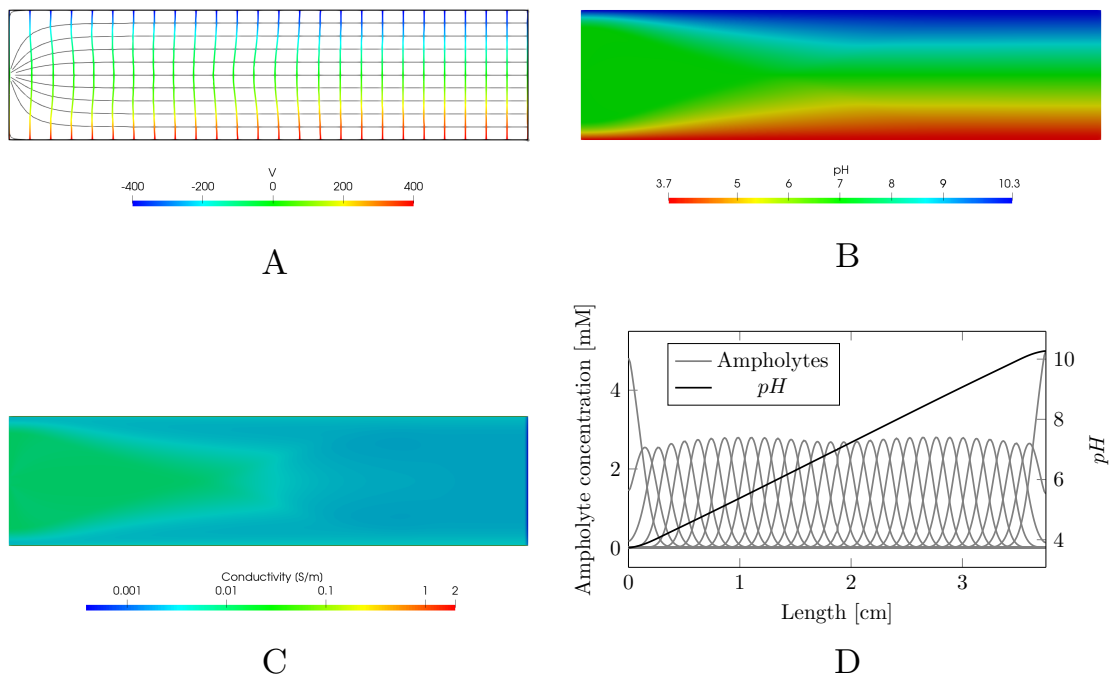

Figure C.3: Results of the free flow isoelectric focusing case after 15 min of simulation. **A**. Fluid flow streamlines (gray) and electric field lines (colored according to the local electric potential). **B**. pH distribution in the separation chamber. **C**. Electrical conductivity distribution in the separation chamber. **D**. Ampholyte concentrations and pH distribution along the outlet section of the separation chamber. In **A**,**B**,**C**, the inlet is at the left and the outlet at the right side of rectangular domains.

3D arbitrary geometries; and (iv) a new operating system–independent method of installation using Docker, which allows `electroMicroTransport` to be used on any computer.

Moreover, three e-µPAD based application examples are provided, including a complete validation from literature data and case of a complex 2D problem. That particular example demonstrates the capabilities of the toolbox for dealing simultaneously with different computational challenges such as a large number of electrolytes, capillary-driven flow and electromigrative velocities in orthogonal directions, and a relatively high number of mesh cells with a computational cost compatible with emerging developments of e-µPADs.

With this new version of `electroMicroTransport`, the scientific community is endowed with an efficient computational open-source tool to numerically prototype new e-µPADs. This is expected to boost the development of e-µPADs, resulting in new techniques and procedures that take full advantage of paper as separation substrate, but also complementing and enhancing

capillary and microchannel applications.

Acknowledgments

We sincerely thank Prof. Takeshi Hirokawa and Prof. Bohuslav Gas for their support regarding the electrolyte database. This research was supported by CONICET, ANPCyT (Grant PICT 2018-02920), and UTN (Grant PID ASUTNFE0005525), Argentina.

Conflict of interest statement

All authors declare complete absence of financial/commercial conflicts of interest.

Data Availability Statement

The data that support the findings of this study are openly available on GitLab at `https://gitlab.com/santiagomarquezd/electroMicroTransport`.

References

G. N. Atfield and C. Morris. Analytical separations by high-voltage paper electrophoresis. amino acids in protein hydrolysates. *Biochem. J*, 81(3):606–614, 1961.

M. Bercovici, S. K. Lele, and J. G. Santiago. Open source simulation tool for electrophoretic stacking, focusing, and separation. *J. Chromatogr. A*, 1216(6):1008–1018, 2009.

M. Bier, O. Palusinski, R. Mosher, and D. Saville. Electrophoresis: Mathematical modeling and computer simulation. *Science*, 219(4590):1281–1287, 1983.

C. L. Chagas, F. R. de Souza, T. M. Cardoso, R. C. Moreira, J. A. da Silva, D. P. de Jesus, and W. K. Coltro. A fully disposable paper-based electrophoresis microchip with integrated pencil-drawn electrodes for contactless conductivity detection. *Anal. Methods-UK*, 8(37):6682–6686, 2016.

H. Cremer and A. Tiselius. Electrophore sis of protein on filter paper. *Biochem. Ztschr.*, 320: 273–283, 1950.

S. Di Fraia, N. Massarotti, and P. Nithiarasu. Modelling electro-osmotic flow in porous media: a review. *Int. J. Numer. Method H*, 28(2):472–497, 2018.

Docker. Docker Inc. `https://www.docker.com/`, 2020. Accessed: 2020-09-25.

M. Dovhunová, M. Malỳ, P. Dubskỳ, G. S. Gerlero, and P. A. Kler. Generalized model of the linear theory of electromigration and its application to electrokinetic chromatography: Capillary zone electrophoretic systems with complex-forming equilibria. *J. Chromatogr. A*, 1610:460595, 2020.

N. Franck, F. Schaumburg, P. A. Kler, and R. Urteaga. Precise electroosmotic flow measurements on paper substrates. *Electrophoresis*, 42(7-8):975–982, 2021.

L. Ge, S. Wang, S. Ge, J. Yu, M. Yan, N. Li, and J. Huang. Electrophoretic separation in a microfluidic paper-based analytical device with an on-column wireless electrogenerated chemiluminescence detector. *Chem. Commun.*, 50(43):5699–5702, 2014.

M. M. Gong and D. Sinton. Turning the page: advancing paper-based microfluidics for broad diagnostic application. *Chem. Rev.*, 117(12):8447–8480, 2017.

T. Hirokawa, M. Nishino, N. Aoki, Y. Kiso, Y. Sawamoto, T. Yagi, and J.-I. Akiyama. Table of isotachophoretic indices: I. simulated qualitative and quantitative indices of 287 anionic substances in the range ph 3–10. *J. Chromatogr. A*, 271(2):D1–D106, 1983.

V. Hruška, M. Jaroš, and B. Gaš. Simul 5–free dynamic simulator of electrophoresis. *Electrophoresis*, 27(5-6):984–991, 2006.

J. W. Jorgenson and K. D. Lukacs. Zone electrophoresis in open-tubular glass capillaries. *Anal. Chem.*, 53(8):1298–1302, 1981.

H. G. Kunkel and A. Tiselius. Electrophoresis of proteins on filter paper. *J. Gen. Physiol.*, 35(1): 89–118, 1951.

S. Márquez Damián, F. Schaumburg, and P. A. Kler. Open-source toolbox for electromigrative separations. *Comput. Phys. Commun.*, 237:244–252, 2019.

B. Y. Moghadam, K. T. Connelly, and J. D. Posner. Isotachophoretic preconcenetration on paper-based microfluidic devices. *Anal. Chem.*, 86(12):5829–5837, 2014.

B. Y. Moghadam, K. T. Connelly, and J. D. Posner. Two orders of magnitude improvement in detection limit of lateral flow assays using isotachophoresis. *Anal. Chem.*, 87(2):1009–1017, 2015.

M. F. Mora, C. D. Garcia, F. Schaumburg, P. A. Kler, C. L. Berli, M. Hashimoto, and E. Carrilho. Patterning and modeling three-dimensional microfluidic devices fabricated on a single sheet of paper. *Anal. Chem.*, 91(13):8298–8303, 2019.

R. A. Mosher and W. Thormann. High-resolution computer simulation of the dynamics of isoelectric focusing: In quest of more realistic input parameters for carrier ampholytes. *Electrophoresis*, 29(5):1036–1047, 2008.

G. Ocvirk, M. Munroe, T. Tang, R. Oleschuk, K. Westra, and D. J. Harrison. Electrokinetic control of fluid flow in native poly (dimethylsiloxane) capillary electrophoresis devices. *Electrophoresis*, 21(1):107–115, 2000.

OpenFOAM. The open source CFD tool. `https://www.openfoam.com/`, 2019. Accessed: 2020-09-25.

T. Rosenfeld and M. Bercovici. 1000-fold sample focusing on paper-based microfluidic devices. *Lab Chip*, 14(23):4465–4474, 2014.

T. Rosenfeld and M. Bercovici. Amplification-free detection of dna in a paper-based microfluidic device using electroosmotically balanced isotachophoresis. *Lab Chip*, 18(6):861–868, 2018.

T. Rosenfeld and M. Bercovici. Dynamic control of capillary flow in porous media by electroosmotic pumping. *Lab Chip*, 19(2):328–334, 2019.

G. I. Salentijn, M. Grajewski, and E. Verpoorte. Reinventing (bio) chemical analysis with paper. *Anal. Chem.*, 90(23):13815–13825, 2018.

N. Scales and R. N. Tait. Modeling electroosmotic and pressure-driven flows in porous microfluidic devices: Zeta potential and porosity changes near the channel walls. *J. Chem. Phys.*, 125(9): 094714, 2006.

F. Schaumburg, R. Urteaga, P. A. Kler, and C. L. Berli. Design keys for paper-based concentration gradient generators. *J. Chromatogr. A*, 1561:83–91, 2018.

F. Schaumburg, P. A. Kler, and C. L. Berli. Comprehensive model of electromigrative transport in microfluidic paper based analytical devices. *Electrophoresis*, 41(7-8):598–606, 2020a.

F. Schaumburg, P. A. Kler, C. S. Carrell, C. L. Berli, and C. S. Henry. Usb powered microfluidic paper-based analytical devices. *Electrophoresis*, 41(7-8):562–569, 2020b.

C. A. Schneider, W. S. Rasband, and K. W. Eliceiri. Nih image to imagej: 25 years of image analysis. *Nature method.*, 9(7):671–675, 2012.

A. L. Shapiro, E. Viñuela, and J. V. Maizel Jr. Molecular weight estimation of polypeptide chains by electrophoresis in sds-polyacrylamide gels. *Biochem. Bioph. Res. Co.*, 28(5):815–820, 1967.

A. P. Shapiro and R. F. Probstein. Removal of contaminants from saturated clay by electroosmosis. *Envir. Sci. Tech.*, 27(2):283–291, 1993.

W. Thormann, J. Caslavska, and R. Mosher. Modeling of electroosmotic and electrophoretic mobilization in capillary and microchip isoelectric focusing. *J. Chromatogr. A*, 1155(2):154–163, 2007.

R. Urteaga, E. Elizalde, and C. L. Berli. Transverse solute dispersion in microfluidic paper-based analytical devices (μpads). *Analyst*, 2018.

H. G. Weller, G. Tabor, H. Jasak, and C. Fureby. A tensorial approach to computational continuum mechanics using object-oriented techniques. *Comput. Phys.*, 12(6):620–631, 1998.

C. Xu, W. Lin, and L. Cai. Demonstrating electrophoretic separation in a straight paper channel delimited by a hydrophobic wax barrier. *J. Chem. Educ.*, 93(5):903–905, 2016.

W. Zhou, L. Xia, X. Xiao, G. Li, and Q. Pu. A microchip device to enhance free flow electrophoresis using controllable pinched sample injections. *Electrophoresis*, 40(16-17):2165–2171, 2019.

Anexo D

electroMicroTransport v2107: Open-source toolbox for paper-based electromigrative separations

El artículo de tipo anuncio de nueva versión (NVA) presentado a continuación ha sido publicado en la revista **Computer Physics Communications**.

G. S. Gerlero, S. Márquez Damián, P. A. Kler. electroMicroTransport v2107: Open-source toolbox for paper-based electromigrative separations. *Computer Physics Communications*, 269:108143, 2021. https://doi.org/10.1002/elps.202000315

electroMicroTransport v2107: Open-source toolbox for paper-based electromigrative separations (New Version Announcement)

Gabriel S. Gerlero[1], Santiago Márquez Damián[1,2], Pablo A. Kler[1,3]

[1]Centro de Investigación en Métodos Computacionales (CIMEC, UNL–CONICET), Colectora RN 168 Km 472, S3000GLN Santa Fe, Argentina

[2]Departamento de Ingeniería Mecánica, FRSF-UTN
Lavaise 610, S3004EWB Santa Fe, Argentina

[3]Departamento de Ingeniería en Sistemas de Información, FRSF-UTN
Lavaise 610, S3004EWB Santa Fe, Argentina

Abstract

Paper-based electromigrative separations have recently gained relevance due to the rise of paper-based microfluidic devices and their combination with electrophoretic methods, used for many different analytical applications [Salentijn et al., 2018]. A new version of the open source toolbox `electroMicroTransport` for the numerical solution of electromigrative separations is presented, now featuring support for porous substrates, like paper, nitrocellulose and other materials used in paper-based microfluidics. This new version is based on a novel mathematical model for these phenomena recently published by our group. Similar to its previous versions, the toolbox was implemented using OpenFOAM®, meaning that it features native 3D problem handling, support for parallel computation, and a GNU GPL license. This new version of `electroMicroTransport` includes full support for electroosmotic flow and the novels mechanical and electrical dispersion

effects. It is now integrated with a well-recognized electrolyte database with its own management utility, and also includes a renewed algorithm for computing and controlling the electric current drainage in arbitrary surfaces. Moreover, for the first time `electroMicroTransport` is available for installation as a Docker image, which means that it is able to correctly run on any operating system. Finally, new tutorial examples and a user manual are provided. This new version of `electroMicroTransport` will enable efficient and reliable numerical prototypes of paper-based electromigrative separations to boost the continuous growth of paper-based microfluidics.

Keywords: Electroosmotic flow, Electrophoresis, Paper-based microfluidics, Finite volume method, High performance computing.

New version program summary

Program Title: electroMicroTransport
CPC Library link to program files: `https://doi.org/10.17632/9wpvypzj9y.2`
Developer's repository link: `https://gitlab.com/santiagomarquezd/electromicrotransport`
Licensing provisions: GPLv3
Programming language: C++, Python
Journal reference of previous version: Computer Physics Communications 237 (2019) 244-252
Does the new version supersede the previous version?: Yes
Reasons for the new version: This new version adds several new features, including support for porous substrates, new boundary conditions, a comprehensive electrolyte database, new tutorial cases, a streamlined installation process, and a Docker installation option.
Summary of revisions:

- Electrolyte database
    - `electroMicroTransport` now includes an electrolyte database based on the one bundled with Simul 6, itself built from the work of Prof. Hirokawa. [Hirokawa et al., 1983, Gaš and Bravenec, 2021]
    - The dabatabase includes the properties of 518 components by default.
    - Simulation cases can directly name database components for easy initialization of electrolyte properties.

    - A new `electrolytes` command-line utility provides access the default electrolyte database to search and query for component properties—as well as to add, update and remove user-defined components.

- New algorithm for electric constant current

    - The new boundary condition called `uniformCurrentDensity` replaces the earlier `uniform1DCurrentDensity` boundary condition [Márquez Damián et al., 2019] which was valid only for 1D domains. With this new condition, it is possible to prescribe a value for constant electric current drained from an arbitrary 3D shaped electrode.
    - Drained current I is calculated as the sum of all of the individual currents flowing through every cell adjacent to the electrode surface.
    - When using a `uniformCurrentDensity` boundary condition, on each iteration, `electroMicroTransport` will provide the user with information on the applied electric current and current density values, the target current, and the effective applied electric potential at the electrode.

- Support for paper substrates

    - This new version of `electroMicroTransport` offers full support for paper-based electrophoretic devices with modified transport equations based on a recent model [Schaumburg et al., 2020].
    - Users can provide different substrate properties such as porosity, tortuosity, Darcy permeability, bias conductivity, and electrokinetic potential.
    - Mechanical and electrophoretically driven dispersion terms require setting values for the coefficients s_f and s_e.
    - When the user cannot provide reliable values for these parameters, default values are used which match the physical characteristics of Whatman #1 paper.
    - A new body force term in the momentum equation for fluid flow was introduced in order to obtain a proper representation of EOF in porous substrates.

- New tutorial cases showcasing the new functionality

    - Paper-based zone electrophoresis experiments: `paperBasedZE`, `paperBasedZE1`, `paperBasedZE2`

  - Paper-based moving-boundary electrophoresis cases: `paperBasedMBE1` (constant voltage), `paperBasedMBE2` (constant current)
  - Paper-based free-flow isoelectric focusing case: `paperBasedFFIEF`

- Automated test suite
  - The `electroMicroTransport` project now includes an automated test suite used by developers to validate the implementations. Test cases are written using the `pytest` framework.
  - Following best practices, the test suite is run automatically as part of the continuous integration/deployment (CI/CD) process.

- User manual
  - A user manual of `electroMicroTransport` is now available, which guides users through the installation and use of the software.
  - The manual also covers many details of the software that might be of interest to users.

- Streamlined installation process
  - This new version of `electroMicroTransport` drops the requirement of a user-writable OpenFOAM installation. This means that `electroMicroTransport` can now be set up to use a system-wide installation of OpenFOAM without any privileges.
  - To allow this, code that previously required modifications to base OpenFOAM has now been packaged into a standalone shared library.
  - This change will benefit users who get OpenFOAM from their system's package manager, as well as any users of shared computers where they might not be able to modify existing packages (e.g. computer clusters).
  - This improvement in the architecture of the program implies a significant reduction in compilation time and resources.

- Docker installation option
  - `electroMicroTransport` is now also available as a Docker image for use with the Docker software [Gerlero et al., 2021]. This image is based on an official Docker image of OpenFOAM and contains pre-built installation of `electroMicroTransport`. It does not require an existing OpenFOAM installation.

- Official images of the toolbox can be obtained from the `microfluidica/electromicrotransport` repository on Docker Hub.
- All Docker images are built and tested automatically during the CI/CD process. This ensures that Docker users always have access to an up-to-date, validated version of the toolbox.
- Docker allows `electroMicroTransport` to be used on non-Linux systems that do not natively support OpenFOAM.

Nature of problem: The `electroMicroTransport` toolbox is intended to offer a complete suite for performing numerical simulations of electromigrative transport, including electroosmotic flow in both open channels and porous substrates. In order to perform this simulations, three partial differential equations and two non-linear conservation equations are solved. The coupled solution of this set of equations provides the different concentration fields for all electrolyte components of the system, the pH and conductivity fields, the fluid flow velocity and pressure fields (associated to the solvent, usually water), and the electric potential field over the entire calculation domain at any simulation time. Numerical simulations provided by `electroMicroTransport` can improve design process of microfluidic electrophoretic devices and its operational parameters as well as to contribute in basic research on developing new separation strategies for emerging analytical applications.

Solution method: As was previously mentioned, `electroMicroTransport` numerical solutions are based on the coupled solving of three partial differential equations and two non-linear conservation equations. The solution method for the partial (in both space and time) differential equations is the Finite Volume Method whose basic methods and functions are provided by the OpenFOAM® platform. The non-linear equations are solved by using ad hoc implemented Newton–Raphson methods in native `C++` language. The different equations are solved sequentially employing weak coupling and temporal sub-looping strategies. These strategies are justified by the fact that the various phenomena (chemical, electrochemical, mechanical and electrical) have different characteristic times for their evolutions. This scheme has been validated and has demonstrated both robustness and computational efficiency.

Additional comments including restrictions and unusual features: except when using the Docker image, installing and running `electroMicroTransport` requires an active installation of OpenFOAM. Only official OpenFOAM® releases distributed by OpenCFD Ltd. are supported by `electroMicroTransport`. This version of `electroMicroTransport` has been tested with OpenFOAM versions 1912, 2006 and 2012.

Acknowledgments

This research was supported by CONICET, ANPCyT (Grant PICT 2018-02920), and UTN (Grant PID ASUTNFE0005525), Argentina.

Conflict of interest statement

All authors declare complete absence of financial/commercial conflicts of interest.

References

B. Gaš and P. Bravenec. Simul 6: A fast dynamic simulator of electromigration. *Electrophoresis*, 2021.

G. S. Gerlero, S. M. Damián, F. Schaumburg, N. Franck, and P. A. Kler. Numerical simulations of paper-based electrophoretic separations with open-source tools. *Electrophoresis*, 2021. doi: \url{~https://doi.org/10.1002/elps.202000315}.

T. Hirokawa, M. Nishino, N. Aoki, Y. Kiso, Y. Sawamoto, T. Yagi, and J.-I. Akiyama. Table of isotachophoretic indices: I. simulated qualitative and quantitative indices of 287 anionic substances in the range ph 3–10. *J. Chromatogr. A*, 271(2):D1–D106, 1983.

S. Márquez Damián, F. Schaumburg, and P. A. Kler. Open-source toolbox for electromigrative separations. *Comput. Phys. Commun.*, 237:244–252, 2019.

G. I. Salentijn, M. Grajewski, and E. Verpoorte. Reinventing (bio) chemical analysis with paper. *Anal. Chem.*, 90(23):13815–13825, 2018.

F. Schaumburg, P. A. Kler, and C. L. A. Berli. Comprehensive model of electromigrative transport in microfluidic paper based analytical devices. *Electrophoresis*, 41(7-8):598–606, 2020.

Anexo E

Comprehensive numerical prototyping of paper-based microfluidic devices using open-source tools

El artículo presentado a continuación se encuentra en revisión en la revista **Talanta Open**.

G. S. Gerlero, C. L. A. Berli, P. A. Kler. Comprehensive numerical prototyping of paper-based microfluidic devices using open-source tools. En revisión.

Comprehensive numerical prototyping of paper-based microfluidic devices using open-source tools

Gabriel S. Gerlero[1,2], Zahar I. Guerenstein[3], Nicolás Franck[1,4], Claudio L. A. Berli[5], Pablo A. Kler[1,4]

[1]Centro de Investigación de Métodos Computacionales (CIMEC, UNL–CONICET), Colectora RN 168 km 472 (3000), Santa Fe, Argentina

[2]Universidad Nacional de Rafaela, Bv. Roca 989 (2300), Rafaela, Argentina

[3]Departamento de Ingeniería Mecánica, Facultad Regional Santa Fe, Universidad Tecnológica Nacional, Lavaisse 610 (3000), Santa Fe, Argentina

[4]Departamento de Ingeniería en Sistemas de Información, Facultad Regional Santa Fe, Universidad Tecnológica Nacional, Lavaisse 610 (3000), Santa Fe, Argentina

[5]Instituto de Desarrollo Tecnológico para la Industria Química (INTEC, UNL–CONICET), Colectora RN 168 km 472, (3000), Santa Fe, Argentina

Abstract

Paper-based microfluidics has emerged as a promising field with diverse applications ranging from medical diagnostics to environmental monitoring. Despite significant progress in research and development, the translation of paper-based prototypes into practical end-user devices remains limited. This limitation stems from challenges related to devices not being sufficiently portable and autonomous, which paper-based microfluidics is expected to overcome. Yet for this purpose, we note the lack of comprehensive numerical modeling tools capable of simulating the intricate physicochemical phenomena involved in order to optimize the development process; hence, in this study, we introduce `porousMicroTransport`, a novel simulation package integrated with the open-

source platform OpenFOAM®, designed to address these challenges. `porousMicroTransport` offers efficient solvers for fluid flow and transport phenomena in microfluidic porous media, including capillarity models and (bio)chemical reactions. We demonstrate the software's effectiveness in two example cases, showcasing its ability to accurately reproduce complex phenomena involved in paper-based devices. By virtue of being an easy-to-use and computationally efficient tool, `porousMicroTransport` facilitates the design and optimization of devices, potentially enabling more devices to meet the WHO's REASSURED criteria for point-of-care testing. We anticipate that this tool will accelerate the development and deployment of robust and portable diagnostic devices, bridging the gap between research and practical applications.

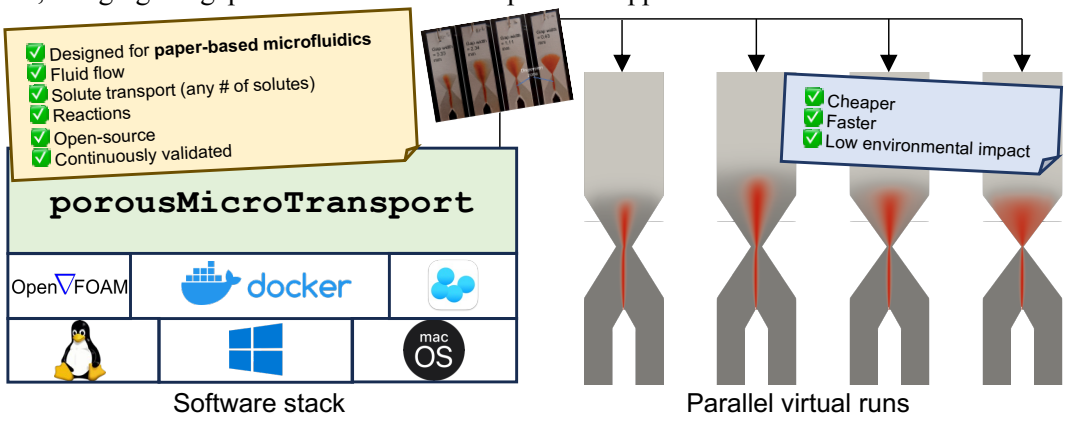

E.1. Introduction

Paper-based microfluidics is nowadays a well-established R&D field; however, the number of end-user applications is still certainly limited [Anushka et al., 2023]. The success of lateral flow assays (LFA), initially developed for pregnancy tests, and more recently widely spread with the rapid test for SARS-CoV-2 detection [Toft et al., 2023], could not be replicated by any other microfluidic paper-based analytical device (µPAD) [Wang et al., 2023]. Despite the huge efforts made by the scientific community to develop µPADs to comply with the REASSURED criteria proposed by the World Health Organization (WHO) [Mabey et al., 2004], at present, only a few examples are available for end users as real point-of-need testing devices [Schaumburg et al., 2022]. Many approaches have failed to simultaneously fulfill all REASSURED criteria mainly due to a high level of dependency on extra equipment for specific and complementary tasks such as heating, driving fluids, actuating valves, incubation, and reactions, among others [Aguiar et al., 2023]. Including these tasks within the functionality of µPADs requires increasing the complexity of devices with the consequent challenges on design and fabrication processes.

Nevertheless, the perspective is optimistic as many researchers both in academia and companies are currently working on improving different aspects of µPADs in medical diagnosis, envi-

ronmental monitoring, and food quality control—among other fields—, to perform more complex tasks while being more robust, portable, and efficient [Sharma et al., 2023]. For example, in order to improve robustness and portability, there are new developments in terms of fabrication techniques and the integration with mobile telephony [Schaumburg et al., 2022, Abou El-Nour et al., 2023]. Simultaneously, in order to improve sensitivity and specificity, new detection techniques coupled with the classic colorimetric and electrochemical ones are being tested [Silva-Neto et al., 2023, Macagno et al., 2023]. Moreover, by improving transport and reaction mechanisms, the limits of detection of the analytes of interest can be significantly increased [Hamidon et al., 2021].

The aforementioned process of optimizing fluid and solute transport, as well as reaction rates, involves the systematic characterization of different substrates [Franck et al., 2021], as well as the analytical and numerical modeling of the different phenomena involved [Gerlero et al., 2021b]. The success of these tasks will enable innovative designs that overcome the current limitations of µPADs. Unfortunately, the amount, complexity, and strong interdependence of the different physicochemical phenomena that determine the performance of a particular µPAD, turns the production of µPAD models with accurate prediction capabilities into an extremely challenging task [Modha et al., 2021]. The phenomena involved include unsaturated fluid flow governed by capillary forces; transport of multiple solute species, including unsaturated advection, anisotropic dispersion, adsorption; and (bio)chemical reactions; all of them strongly coupled and highly nonlinear [Bear and Cheng, 2010]. Remarkably, under very basic operation conditions and for simple geometries, some analytical and numerical models can help designers determine imbibition times or reactant volumes demanded [Gerlero et al., 2023, Elizalde et al., 2015, Berli and Kler, 2016]. However, accurate and computationally efficient numerical prototypes are mandatory for the design and optimization of more sophisticated applications involving 2D complex geometries, multistep procedures, multiple fluid inlets as well as several reacting species, automatic sequential fluid delivery, or different porous materials [Yang et al., 2021].

However, at present µPAD developers do not have any software tool available able to simulate all of the aforementioned phenomena and their interactions, particularly involving complex chemical reactions [Schaumburg et al., 2018a]. In contrast, soil, as an archetypical instance of porous media, has been simultaneously studied and modeled with a set of equations similar to that needed to model µPADs [Ladd and Szymczak, 2021]. Nonetheless, soil transport properties and capillary flow models differ significantly and are not fully valid for paper [Gerlero et al., 2022]. One of the most powerful tools in this scenario is PFLOTRAN [Lichtner et al., 2017], which is open-source and highly efficient for parallel computing, but it is not yet fully adapted for paper-based microfluidics [Berthet et al., 2009]. Moreover, few attempts of numerical modeling µPADs with COMSOL

Multiphysics were performed, yet significant discrepancies with experimental results for unsaturated flow and scalar transport were reported. Furthermore, chemical reactions were not reported within the models solved with this proprietary software [Tirapu-Azpiroz et al., 2018].

In this work, we propose the use of `porousMicroTransport`, a novel package that integrates with the open-source platform OpenFOAM®. Particularly, `porousMicroTransport` offers highly efficient solvers for saturated and unsaturated fluid flow, including the classical capillarity models (i.e. Brooks and Corey and Van Genuchten) as well as some alternative ones such as LET; including the possibility for users to define their own models. Regarding the scalar transport in porous media, several mechanisms are modeled such as (un)saturated advection, Brownian diffusion, mechanical dispersion, and adsorption, as well as a general arbitrary-order chemical reaction library that enables to the modeling of different types of (bio)chemical reactions. `porousMicroTransport` is also easy to set up, either on top of an OpenFOAM® installation or via Docker [Merkel et al., 2014], and several fully functional tutorials are available within its installation. Moreover, due to the integration of `porousMicroTransport` to OpenFOAM®, all the advantages of the latter platform are available for users such as native support for arbitrary 3D domains, automatic compatibility with parallel computation (which can scale up to supercomputing), and the availability of source code under a GNU GPL license.

Along this work, mathematical models for all phenomena involved are reported as well as the minimal computational details for enabling users to install `porousMicroTransport` and run the available tutorials. Two of such tutorials are presented here, while the comparison of the numerical results with experimental data is reported and discussed. Such tutorials include all the fluid flow, transport and chemical reactions mechanisms available in `porousMicroTransport` for accurate and efficient numerically prototyping of µPADs. `porousMicroTransport` is a powerful open-source tool for improving devices and boost the launch of devices that finally can fulfill the REASSURED criteria.

E.2. Mathematical modeling

E.2.1. Fluid flow modeling

Accurate modeling of passive capillary-based pumping in paper-based microfluidics, from simple lateral flow tests to more complex analytical devices, requires considering the flow in the unsaturated regime—i.e., solving for a scalar saturation or moisture content field that varies in space and time. Using a Darcy-based approach, unsaturated capillarity-driven flow in a porous

medium can be deemed governed by the moisture diffusivity equation[Bear and Cheng, 2010]:

$$\frac{\partial \theta}{\partial t} - \nabla \cdot [D(\theta) \nabla \theta] = 0 \tag{E.1}$$

This is a nonlinear diffusion equation in which θ represents the moisture content and $D(\theta)$ is a moisture content–dependent diffusivity defined by an unsaturated capillary flow model. It constitutes a special case of the Richards equation of flow in porous media when gravity effects are neglected, as is the case in µPADs [Gerlero et al., 2023]. For the case of the LETd capillary flow model [Gerlero et al., 2022], the diffusivity function has the expression:

$$D(\theta) = D_{wt} \frac{S_{wp}^L}{S_{wp}^L + E(1 - S_{wp})^T} \tag{E.2}$$

with $S_{wp} = (\theta - \theta_s) \,/\, (\theta_s - \theta_r)$, where θ_s is the material's effective porosity and θ_r is the residual moisture content, while L, E, T and θ_r are fitting parameters that characterize the solid–liquid system.

E.2.2. Solute transport

The transport of every diluted chemical species in a porous medium is modeled through the mass conservation equation as follows [Bear and Cheng, 2010]:

$$\frac{\partial R_d \theta C}{\partial t} = \nabla \cdot [\theta D_{\text{eff}} \nabla C] - \nabla \cdot [UC] + \theta F \tag{E.3}$$

where C is the species concentration (in terms of either mass or molar units), U is the Darcy velocity ($U = -D\nabla\theta$), R_d is a retardation factor, D_{eff} is an effective diffusivity, and F is a reaction term (c.f. Appendix E.2.3). In this conservation equation, the left hand side represents the temporal variation rate of C, while the right hand side represents the fluxes and the generation/exhaustion.

In the temporal term, the retardation factor R_d quantifies the resistance to the movement of the dissolved species due to reversible partial adsorption onto the porous matrix, which in paper is explained by chromatographic effects [Franck et al., 2023]. It is defined as:

$$R_d = 1 + \frac{\rho_s \left(1 - \varepsilon_{\text{tot}}\right) K_d}{\theta} \tag{E.4}$$

where ρ_s is the density of the solid material, ε_{tot} is the total porosity[1] and K_d is a species-dependent partitioning coefficient for adsorption. When K_d is zero, $R_d = 1$ and the coefficient has no effect; while the retardation effect increases as K_d grows.

[1] The total porosity may differ from the effective porosity due to the existence of non-connected void structures.

When considering the diffusive flow, the effective diffusivity D_{eff} accounts for the effects of Brownian molecular diffusion and mechanical dispersion in a porous material. Its expression is [Horgue et al., 2022, Bear and Cheng, 2010]:

$$D_{\text{eff}} = \left(\frac{D_M}{\tau} + \alpha_T |V| \right) I + (\alpha_L - \alpha_T) \frac{VV}{|V|} \tag{E.5}$$

where I is the identity tensor and V is the true velocity of the fluid ($V = U/\theta$). D_M is the species' molecular diffusion coefficient, while τ is the diffusive tortuosity, which measures the medium's resistance to diffusion. Finally, α_T and α_L are, respectively, scalar transverse and longitudinal dispersion coefficients of the medium.

E.2.3. Reaction terms

`porousMicroTransport` bundles an implementation of a reaction library. The library supports arbitrary order reactions, following a general expression of the form:

$$\mathrm{n_{R_1}\, R_1^{p_{R_1}} + n_{R_2}\, R_2^{p_{R_2}} + ... \underset{k_r}{\overset{k_f}{\rightleftharpoons}} n_{P_1}\, P_1^{p_{P_1}} + n_{P_2}\, P_2^{p_{P_2}} + ...} \tag{E.6}$$

where k_f and k_r are the forward and reverse rate constants, R_i are the reactant species, P_i the product species, $\mathrm{n_{R_i}}$ and $\mathrm{n_{P_i}}$ represent the stoichiometric coefficients, and $\mathrm{p_{R_i}}$ and $\mathrm{p_{P_i}}$ the reaction exponents for reactants and products respectively. Each Eq. (E.6) implies a net reaction rate F given by:

$$k_f \left([R_1]^{p_{R_1}} + [R_2]^{p_{R_2}} + ... \right) - k_r \left([P_1]^{p_{P_1}} + [P_2]^{p_{P_2}} + ... \right) \tag{E.7}$$

which is added to the reaction term in Eq. (E.3) for each product species P_i, but also to each reactant species R_i with opposite sign; in both cases multiplied by the species' stoichiometric coefficient n_{P_i} or n_{R_i}.

E.3. Materials and methods

E.3.1. Software

`porousMicroTransport` has been developed as an add-on for OpenFOAM®, an open-source multiphysics platform for solving partial differential problems [Jasak, 1996, Weller et al., 1998].

`porousMicroTransport` can either be compiled from its source code or downloaded in precompiled form as a Docker image. For compilation from source, `porousMicroTransport`'s only requirement is a development installation of OpenFOAM® v2112 or later as distributed by OpenCFD Ltd. (Bracknell, UK). As OpenFOAM®, `porousMicroTransport` is open-source software available under the GNU General Public License (GPL) v3.0.

Notably, the software includes an automated test suite that can verify the correct functioning of the different solvers. The test suite is written in Python and uses asynchronous APIs in order to run separate test cases in parallel, taking maximum advantage of the available computing resources in order to achieve very reasonable execution times of less than a minute for the entire suite using common hardware. This test suite also runs automatically online within the source code repository in order to ensure that any proposed changes do not negatively impact existing functionality. This continuous integration stage also tests for compatibility with all supported OpenFOAM versions, and uploads new Docker images if necessary.

For its part, the user-facing definition of `porousMicroTransport` cases is deliberately inspired by `porousMultiphaseFoam` [Horgue et al., 2022], another toolbox for OpenFOAM® dedicated to multiphase flow and transport (without reactions) in soil.

For more information on the installation and operation of `porousMicroTransport`, please refer to the online README file and/or in the supplementary material that accompanies this work.

Other software utilized for this work was ParaView (Kitware Inc., Clifton Park, N. Y., United States) for data visualization, and OpenFOAM.app [Gerlero, accessed Feb 15, 2024] for running OpenFOAM® natively on macOS.

E.3.2. Numerical details

All solvers use the finite-volume method for discretization of the equations as implemented in OpenFOAM®. What follows is a description of certain implementation details.

E.3.2.1. Flow equation

Within `porousMicroTransport`, linearization of Eq. (E.1)—which, depending on the conditions and the model used for D, can be highly nonlinear—is attained via Picard's method; i.e., repeated solving of a linear form of the equation that uses the previous known value for the nonlinear variables until a known tolerance is achieved.

E.3.2.2. Exhaustible-reservoir boundary condition

A special boundary condition can be used when solving Eq. (E.1) to represent an inlet reservoir with a finite volume of liquid (typically a drop) that can be exhausted. These kinds of reservoirs are used to orchestrate the temporal progression necessary for automatic sequential delivery. The boundary condition behaves as follows.

Under normal flow conditions—i.e., while the reservoir has enough remaining liquid that the inflow is limited solely by Eq. (E.1)—, the boundary condition behaves like a Dirichlet-type condition that prescribes the value of θ; exactly as would be used to model a reservoir with infinite capacity. However, once the remaining capacity falls below the inflow predicted by the flow equation, the boundary condition switches to the Neumann type. Under this Neumann-type condition, the flow through the boundary is prescribed to be equal to the remaining capacity, in order to allow the modeled reservoir to be fully exhausted while making sure that mass is conserved.

E.3.2.3. Reactive transport equation

The reaction model uses an explicit numerical scheme in order to support segregated solving—i.e., the concentration of each species is solved separately, as is conventional in OpenFOAM®—while ensuring that total mass is preserved. Notably, the reaction model is independent from the rest of the package and thus could be easily adapted for use by other solvers within the OpenFOAM® ecosystem. We note that the reactive transport equation, Eq. (E.3), can be nonlinear in the presence of reactions; yet there is no provision for iterative linearization for this equation. This is done in order to improve performance; nevertheless, it requires careful management of the timestepping in order to preserve accuracy.

E.3.2.4. Automatic timestep management

`porousMicroTransport` includes a modular timestep control library that can support the needs of the different solvers for the possibly concurrent phenomena of flow and reactive transport. When enabled, it automatically adjusts the timestep in order to improve performance while preserving a certain level of accuracy that can be configured independently for each phenomenon. For fluid flow, it uses the required number of Picard iterations as a proxy for the difficulty in solving Eq. (E.1); increasing or decreasing the timestep taken accordingly. For the reactive transport, the user can configure a maximum bound for the concentration change in a single timestep in a single finite-volume cell (as global absolute, per-species absolute, or relative tolerance), which will be used to adjust the steps taken. In all cases, a maximum step can also be configured and will—expectedly—take precedence.

Notably, and given that the nonlinearity of the phenomena at play works against an accurate prediction of the expected change in the variables being solved for in a single timestep, the timestep control library has the ability to rewind a timestep and solve again (with a smaller step, and repeatedly if necessary) if the changes in a solved timestep would violate the configured timestepping constraints. This means that any timestepping restrictions set by the user are always enforced; it also means that an appropriate initial timestep need not be configured by the user and can instead be left to be found automatically by the solvers.

E.3.2.5. Parallelism

The solvers in `porousMicroTransport` are compatible with parallel solving through domain decomposition and the MPI standard, a method which offers impressive scalability for complex problems.

E.3.3. Meshing

`porousMicroTransport` is compatible with any finite-volume mesh supported by OpenFOAM®. For the reactive mixing device discussed in Appendix E.4.1, the mesh consisted of 80 000 prisms and was made with a natural scripting mesher included in OpenFOAM®—i.e. `blockMesh`. This scripted mesh enables users to easily modify the geometry (including the gap, which is particularly important in this case—although any change in the layout can be applied this way) by just modifying a single line of code in the `blockMeshDict` configuration file. For the second case (Appendix E.4.2), a mesh of 87 325 hexahedra was generated with Simcenter STAR-CCM+ (Siemens Industry Software Inc, Plano, Texas, USA).

E.3.4. Hardware

The hardware used with `porousMicroTransport` for this paper was as follows. The reacting mixer case (Appendix E.4.1) was run on a MacBook Air (Apple Inc., Cupertino, Calif., USA) with an M1 chip with 8 GB of system RAM, using a single process for each case. For the sequential delivery application case (Appendix E.4.2), each case ran on a single supercomputing node equipped with two Xeon Gold 6226R (Intel Corporation, Santa Clara, Calif., USA) CPUs (for a total of 32 computing cores) and 192 GB of RAM.

E.4. Results and discussion

Two tutorial cases included in `porousMicroTransport` are presented, discussed and compared with experimental results with the aim of demonstrating its capabilities for the numerical prototyping of complex devices. The selected examples include multiple inlets for unsaturated flow, sequential delivery–class automation using exhaustible reservoirs, multiple solutes as reactants and products—including pre-adsorbed species—, and also two different reaction mechanisms. The results obtained are compared with the experimental results present in literature to show `porousMicroTransport` accuracy, while its robustness is shown through the complexity of the devices and its operation. In both cases, Whatman No. 1 filter paper was used as substrate. Fluid flow and transport properties of this filter paper are listed in Tables E.1 and E.2, respectively.

Description	Symbol	Value	Ref.
Effective porosity	θ_s	0.7	[Gerlero et al., 2022]
Initial moisture content	θ_i	0.025	[Gerlero et al., 2022]
Residual moisture content	θ_r	1.985×10^{-2}	[Gerlero et al., 2022]
LETd L coefficient	L	4.569×10^{-3}	[Gerlero et al., 2022]
LETd E coefficient	E	$12\,930$	[Gerlero et al., 2022]
LETd T coefficient	T	1.505	[Gerlero et al., 2022]
LETd D_{wt} coefficient	D_{wt}	$4.660 \times 10^{-4}\,\mathrm{m^2\,s^{-1}}$	[Gerlero et al., 2022]

Table E.1: Flow parameters for Whatman No. 1 paper

Description	Symbol	Value	Ref.
Diffusive tortuosity	τ	5.29	[Franck et al., 2022]
Mechanical dispersivity	α_T, α_L	$30 \times 10^{-6}\,\mathrm{m}$	[Urteaga et al., 2018]
Total porosity	ε_{tot}	0.7	[Gerlero et al., 2022]
Solid matrix density	ρ_s	$1611\,\mathrm{kg\,m^{-3}}$	[Gerlero et al., 2022, Pena-Pereira et al., 2018]

Table E.2: Transport parameters for Whatman No. 1 paper

E.4.1. Reactive flow in a passive mixing device

This first tutorial example discusses the numerical prototyping of a passive reactive mixer presented by Hamidon et al. [2021]. In that work, the authors present a patterned hourglass structure for the coflow and mixing of two reactant species: Fe^{3+} from $FeCl_3$, and SCN^- from KSCN in

solution. Each diluted compound enters the flow domain through reservoirs located at the bottom of the device. Due to imbibition, both solutions flow upward while generating a parallel reactive interface where the following reaction develops:

$$Fe^{3+} + SCN^{-} \underset{k_r}{\overset{k_f}{\rightleftharpoons}} FeSCN^{2+}.$$

The product of the strong covalent reaction $FeSCN^{2+}$ has a particular red color that can be measured with high-precision by using standard image processing tools.

One may add a brief perspective on the foundations and evolution of this problem: the transverse dispersion of analytes under capillary-driven flow in paper substrates was first evaluated by Urteaga et al. [2018]. Mechanical dispersion was assessed by theory and experiments, introducing a change of paradigm for the design of mixers, diluters, and concentration gradient generators on μPADs. On these foundations, the same group employed computer simulations to investigate the optimal design of paper geometries for these operations [Schaumburg et al., 2018b], where the sequence of constriction plus diffuser emerged as the best concept for mixing on paper. Later on, Verpoorte's group nicely implemented the concept to speed up reactions on paper substrates [Hamidon et al., 2021]. Here, we are presenting a numerical model that reproduces the entire problem for the first time, accounting for spontaneous liquid imbibition, species transport with both Brownian and mechanical dispersion, and chemical reactions. Hamidon et al. proposed the hourglass geometry with a gap of variable width in order to empirically study the mixing efficiency of the design (Fig. E.1(a)). This tutorial reproduces the behavior of all of the devices manufactured by the authors to make the comparison of mixing performance. Such performance is evaluated through the color profiles determined at the gap cross section.

E.4.1.1. Physical properties and boundary conditions

In Table E.3 the transport and reaction properties of reactants are reported, as well as the concentration of every reactant at its particular inlet reservoir. At the reservoirs, the reported concentration is imposed as a Dirichlet boundary condition as well as the full saturation condition for the imbibition flow solver. For the other boundaries of the domain, the condition for transport and flow is a natural Neumann condition, i.e. no fluid nor solute flow in the normal direction to the boundary.

E.4.1.2. Results

Fig. E.1 gathers the experimental (a) and numerical (b) results for the mixing/reactive transport process developed in the prototype proposed by Hamidon et al. [2021]. In this figure, the effect of

Description	Symbol	Value	Ref.
Inlet Fe concentration	$[\mathrm{Fe}]_0$	$50\,\mathrm{mm}$	[Hamidon et al., 2021]
Inlet SCN concentration	$[\mathrm{SCN}]_0$	$50\,\mathrm{mm}$	[Hamidon et al., 2021]
Molecular diffusivity Fe	$D_{M_{Fe}}$	$1.45 \times 10^{-9}\,\mathrm{m^2\,s^{-1}}$	[Gerlero et al., 2021a]
Molecular diffusivity SCN	$D_{M_{SCN}}$	$1.77 \times 10^{-9}\,\mathrm{m^2\,s^{-1}}$	[Gerlero et al., 2021a]
Forward reaction rate constant	k_f	$89\,\mathrm{m^{-1}\,s^{-1}}$	[de Berg, 2019]
Reverse reaction rate constant	k_r	$0.72\,\mathrm{s^{-1}}$	[de Berg, 2019]

Table E.3: Parameters for the reactive mixer tutorial case.

different gap widths is shown. The experimental results produced two kinds of colors. First, the grey field indicates the saturation field, and how the imbibition process developed upwards. The numerical results of the saturation field, solved through Eqs. (E.1) and (E.2) can be directly compared, showing similar results in terms of velocity of the fluid front, but also in terms of fluid front curvature. This result emphasizes the capability of `porousMicroTransport` to solve 2D imbibition flow in µPADs with non-trivial layout. It is noteworthy that our calculations take advantage of previous works devoted to the characterization of fluid flow and solute transport in Whatman No. 1 filter paper [Gerlero et al., 2022, Franck et al., 2022, Urteaga et al., 2018].

On the other hand, red is used to represent the concentration of the FeSCN product. When comparing the red-color profiles across all four devices, the similitude between the experimental and numerical fields for the same physical time is again remarkable. In this sense, it is important to highlight both the capability of `porousMicroTransport` to correctly reproduce all transport phenomena, and the fact that the transport properties and the reaction rate constants correctly characterize the experiments (Table E.3).

Moreover, when focusing the analysis on the concentration profiles shown in Fig. E.1 for all layouts with the aim of evaluating the mixing efficiency of each design, it can be seen that identical shapes are obtained for all cases. As it was already mentioned for the fluid flow and transport, it is clear that `porousMicroTransport` is able to reproduce the reaction mechanisms, but also the reaction rate constants extracted from literature. It is pertinent to emphasize here, that no arbitrary data or correction coefficient was used in the calculations: geometrical dimensions, and physicochemical parameters were directly obtained from the literature.

Regarding the numerical costs, the four cases ran simultaneously to completion in less than three hours on our hardware, which consisted of a lightweight consumer-grade laptop (c.f. Appendix E.3.4). The analysis of results is straightforward in ParaView. It is important to compare this cost with that of the experiments of the original work, upon developing every device and cor-

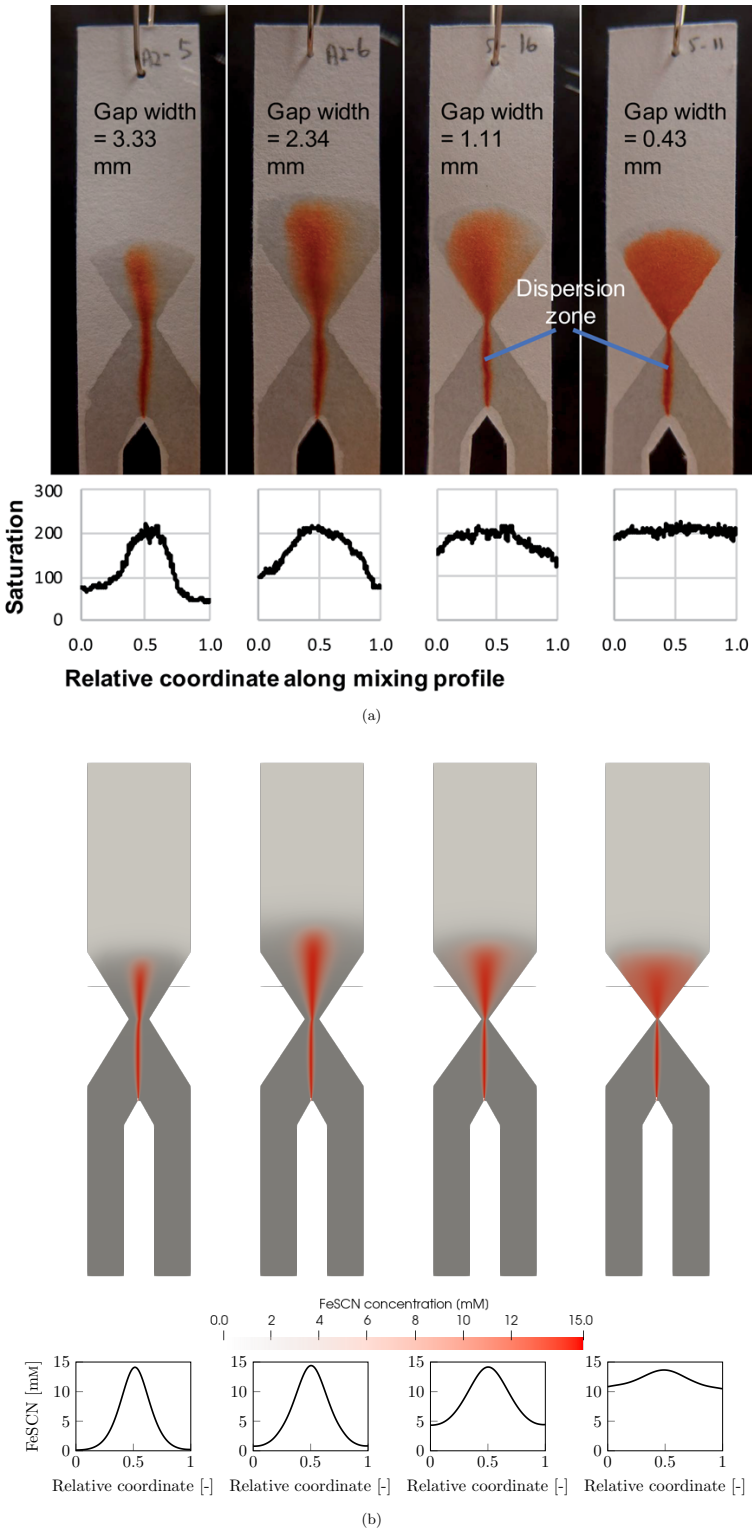

Figure E.1: (a) Experimental results from Hamidon et al. [2021]; upper panel, images of the four tested devices; lower panel, distribution of the reaction product at the mixing zone. Adapted under the Creative Commons Attribution 3.0 Unported License. (b) Numerical results obtained in this work; upper panel, images of the four geometries; lower panel, distribution of the reaction product at the mixing zone (horizontal line). The grey field indicates fluid saturation.

responding test. The latter costs include the manufacturing, operation, and analysis of the results, together with relatively high costs in materials and supplies, as well as qualified personnel-hours. In contrast, by using `porousMicroTransport` all the experimental tests can be run concurrently by a single person, on a consumer-grade computer. Furthermore, once the design and the operational sequence is optimized, a single experiment can be performed to corroborate the results, with the consequent decrease in resources and time invested in the development process.

E.4.2. Sequential delivery application

In this second tutorial, a paradigmatic μPAD is numerically prototyped. It is a device proposed by Fu et al. for detection of the malaria antigen *Pf* HRP2. In order to detect the aforementioned antigen, the authors proposed an Enzyme-Linked Immunosorbent Assay (ELISA) technique which involves several sequential steps illustrated in Fig. E.2: (i) the antigen solution (green) flows over the test line (Fig. E.2 (a-b)); (ii) the labeled antibody solution (pink) flows over the analyte attached to the test antibody and the control line (Fig. E.2 (c)); and finally, the gold enhancement reagent flows over the two lines turning the test and control lines more visible (Fig. E.2 (d)).

To highlight our contributions on this problem, it is appropriate to mention that the sequential delivery of fluids for a multistep reaction had been early proposed Fu et al. [2010], who demonstrated the controlled reagent transport in disposable 2D paper networks. Then, the same group used the platform to implement heterogeneous immunoassay reactions with the format of lateral flow assays [Liang et al., 2016], where the entire process was optimized on a purely experimental basis. More recently, Rath and Toley [2020] successfully implemented a computational model to describe the entire device, including relevant aspects, such as the flow through assemblies of multiple paper, species transport, and the feature of fluid reservoir with limited-volume. The numerical model we are presenting here improves on two critical aspects: (i) the prediction of the device readout in terms of test and control line product concentrations, by including the chemical reactions that take place, and (ii) the full description of species transport, by including mechanical dispersion, which is a dominant mechanism in paper substrates. Additionally, we have also tested the sequential assay concept of Liang et al. [2016] in a sequential delivery format with the purpose of enhancing the output signal.

The several reactions that develop in the µPAD were modeled as follows:

$$Pf\text{HRP2} + \text{LA} \rightleftharpoons Pf\text{HRP2 LA} \tag{E.8}$$

$$Pf\text{HRP2} + \text{TLA} \rightleftharpoons Pf\text{HRP2 TLA} \tag{E.9}$$

$$Pf\text{HRP2 LA} + \text{TLA} \rightleftharpoons Pf\text{HRP2 LA TLA} \tag{E.10}$$

$$Pf\text{HRP2 TLA} + \text{LA} \rightleftharpoons Pf\text{HRP2 LA TLA} \tag{E.11}$$

$$Pf\text{HRP2 LA TLA} + \text{GER} \rightleftharpoons Pf\text{HRP2 LA TLA GER} \tag{E.12}$$

$$\text{LA} + \text{CLA} \rightleftharpoons \text{LA CLA} \tag{E.13}$$

$$\text{LA CLA} + \text{GER} \rightleftharpoons \text{LA CLA GER} \tag{E.14}$$

where LA corresponds to the labeled antibody, TLA and CLA to the test- and control-line antibodies respectively, and GER refers to the gold enhancement reagent. We note that in the premix case—as opposed to the sequential format of Liang et al. [2016]—, the reaction Eqs. (E.9) and (E.11) do not apply.

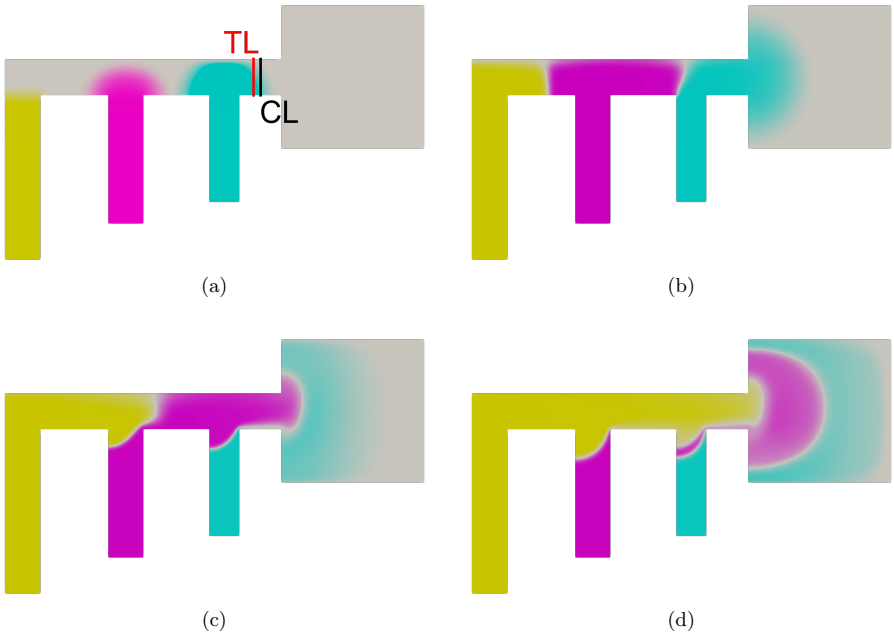

Figure E.2: Automatic delivery sequence. (a) Start of the sequence, with locations of the test (TL) and control (CL) lines highlighted. (b) First solute passes the test and control lines. (c) Second solute arrives at the test and control lines. (c) Final solute arrives.

E.4.2.1. Physical properties and boundary conditions

The transport properties of the antigen, antibody, and other molecules were taken from Fu et al. [2012]. In a similar fashion to the previous case, the inlet concentrations are imposed as a

Dirichlet boundary condition at the reservoirs. Regarding imbibition flow, exhaustible-reservoir boundary conditions are imposed to automatically develop the delivery sequence. Similarly, for the other boundaries of the domain, the condition for transport and fluid flow is natural Neumann condition; i.e. no fluid nor solvent flow in the normal direction to the boundary. The reaction rates are reported in Table E.4.

Reaction	Forward rate constant $[\mathrm{m}^{-1}\,\mathrm{s}^{-1}]$	Dissociation rate constant $[\mathrm{s}^{-1}]$
Eq. (E.8)	5×10^{7}	1.3×10^{-4}
Eq. (E.9)	1×10^{6}	7.1×10^{-4}
Eq. (E.10)	3.4×10^{3}	7.1×10^{-4}
Eq. (E.11)	1.6×10^{5}	2.2×10^{-3}
Eq. (E.12)	3.4×10^{5}	7.1×10^{-4}
Eq. (E.13)	3.4×10^{4}	7.1×10^{-4}
Eq. (E.13)	3.4×10^{5}	7.1×10^{-4}

Table E.4: Reaction rate constants for the sequential delivery application case, as obtained from Liang et al. [2016].

E.4.2.2. Results

Figure E.3 gathers several important results of the two numerical prototypes developed in this tutorial example. The results show qualitative agreement between the unamplified and amplified products of Fig. E.3(a) and (c), and simulations lie within the error bars in (b). The sequential configuration, although not experimentally tested in the sequential delivery format by Fu et al. [2012], is shown to yield higher concentrations of the amplified product than the premix configuration. Each simulation case runs to completion in approximately 45 minutes using 32 concurrent processes.

E.5. Conclusions

In this work, we have introduced a novel open-source tool for the comprehensive numerical prototyping of µPADs named `porousMicroTransport`. The software is distributed as an extension for the the well-known OpenFOAM® finite volume–based multiphysics platform, inheriting all of its advantages such as arbitrary 3D mesh compatibility, parallel and supercomputing sup-

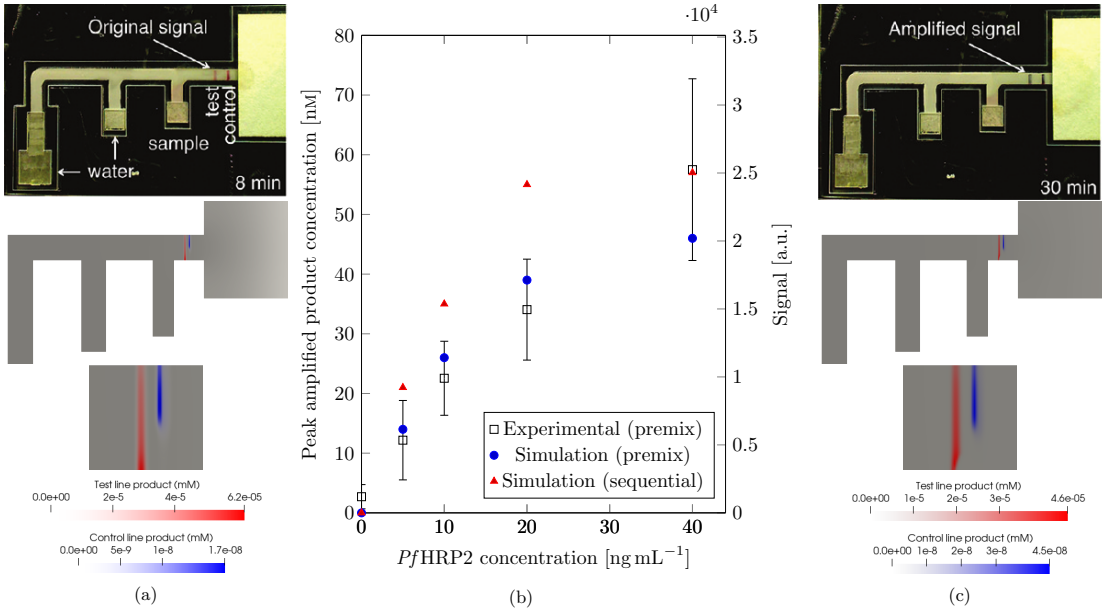

Figure E.3: (a) and (c) Visualization of unamplified and amplified (respectively) results for an analyte concentration of 200 ng mL^{-1}. Upper panels, experimental results from Fu et al. (Reprinted with permission from Fu et al. [2012]. Copyright 2012 American Chemical Society). Lower panels, numerical results obtained in this work, along with a focus on the test and control lines. (b) Comparison of test line signals and concentrations between experimental results from Fu et al. (optical signals) and this work (product concentrations), with an additional series showing a simulated sequential format based on the work of Liang et al. [2016] using this geometry.

port, compatibility with high-performance data visualization, and one of the most active developer communities for open-source simulation software.

Particularly, `porousMicroTransport` offers numerical capabilities for the simulation of any arbitrary µPAD layout and its different operating conditions. The numerical prototypes include saturated and unsaturated fluid flow regimes, with a collection of boundary conditions, such as fixed saturation or, exhaustible reservoir. Moreover, it includes a transport solver that includes all the known important mechanisms present in µPADs, i.e. fluid advection, Brownian diffusion, and anisotropic dispersion. Finally, it bundles a general reaction library with arbitrary order and stoichiometric coefficients. Notably, the software is easy to use for non-expert users, which is not presently a main characteristic of PFLOTRAN. It is also continuously validated by means of an automated test suite. Finally, it should be mentioned that `porousMicroTransport` is also able to run seamlessly on any major operating system due to its availability as a pre-compiled Docker image.

All the aforementioned features of `porousMicroTransport` were demonstrated along the paper by correctly and precisely reproducing all of the phenomena involved in the tutorial examples. These tutorials were selected due to their complexity and significance for the µPAD developer community. The success of `porousMicroTransport` in numerically prototyping both devices is more significant when considering the computational costs reported that are considerably lower than the experimental time demanded for obtaining similar analyses.

With this contribution, we offer µPAD developers a very competitive numerical tool for design and optimization, to be used before and coupled to experiments in the classical iterative path from concept to product. We expect that in the near future, with the aid of `porousMicroTransport`, more µPADs can finally fulfill the WHO's REASSURED criteria for end users.

Acknowledgements

This work was supported by CONICET, Agencia I+D+i [grant number PICT-2018-02920 and PICT-2021-00651] and UTN [grant numbers PID8132, PID8685], Argentina. The authors acknowledge Prof. Raúl Urteaga for fruitful discussions on the topic of chromatographic effects.

The present work used computational resources of the Pirayu cluster, acquired with funds from the Santa Fe Science, Technology and Innovation Agency (ASACTEI), Project AC-00010-18, Resolution No. 117/14. The aforementioned equipment is part of the National High-Performance Computing System (SNCAD).

CRediT authorship contribution statement

Gabriel S. Gerlero: Software, Validation, Investigation, Writing - Review & Editing, Visualization. **Zahar I. Guerenstein**: Investigation, Data curation, Writing - Review & Editing. **Nicolás Franck**: Methodology, Investigation, Data curation, Writing - Review & Editing. **Claudio L. A. Berli**: Conceptualization, Writing - Review & Editing, Project administration. **Pablo A. Kler**: Conceptualization, Validation, Writing - Original Draft, Project administration, Funding acquisition.

Conflicts of interest

The authors declare no financial/commercial or academic conflict of interest.

Data availability

The datasets generated and/or analyzed in the course of the current study are available at `https://github.com/gerlero/porousMicroTransport`.

References

K. M. Abou El-Nour, I. M. El-Sherbiny, A. M. Abbas, E. H. Salem, and G. M. Khairy. Applying smartphone camera, spectrophotometry, or ocular analysis-based dipsticks for the detection of glutathione level as a cancer biomarker. *Talanta Open*, 7:100211, 2023.

J. I. Aguiar, A. O. Rangel, and R. B. Mesquita. Salivary calcium determination with a specially developed microfluidic paper-based device for point-of-care analysis. *Talanta Open*, 8:100254, 2023.

Anushka, A. Bandopadhyay, and P. K. Das. Paper based microfluidic devices: a review of fabrication techniques and applications. *The European Physical Journal Special Topics*, 232(6): 781–815, 2023.

J. Bear and A. H.-D. Cheng. *Modeling groundwater flow and contaminant transport*, volume 23. Dordrecht, Netherlands, Springer Science & Business Media, 2010.

C. L. A. Berli and P. A. Kler. A quantitative model for lateral flow assays. *Microfluidics and Nanofluidics*, 20(7):104, 2016.

H. Berthet, H. Stone, F. Marty, B. Mercier, J. Jundt, and D. Angelescu. Design and characterization of a MEMS-microfluidic sensor for rheological applications. *Advanced Materials Research*, 74:81–84, 2009.

K. C. de Berg. *The Reaction and Its Kinetics*, pages 71–86. Springer International Publishing, Cham, 2019. ISBN 978-3-030-27316-3.

E. Elizalde, R. Urteaga, and C. L. A. Berli. Rational design of capillary-driven flows for paper-based microfluidics. *Lab on a Chip*, 15(10):2173–2180, 2015.

N. Franck, F. Schaumburg, P. A. Kler, and R. Urteaga. Precise electroosmotic flow measurements on paper substrates. *Electrophoresis*, 42(7-8):975–982, 2021.

N. Franck, C. L. A. Berli, P. A. Kler, and R. Urteaga. Multiphysics approach for fluid and charge transport in paper-based microfluidics. *Microfluidics and Nanofluidics*, 26(11):87, 2022.

N. Franck, L. Vera Candioti, G. S. Gerlero, R. Urteaga, and P. A. Kler. A simple method for the assessment of electrophoretic mobility in porous media. *Electrophoresis*, 2023.

E. Fu, B. Lutz, P. Kauffman, and P. Yager. Controlled reagent transport in disposable 2D paper networks. *Lab on a Chip*, 10(7):918–920, 2010.

E. Fu, T. Liang, P. Spicar-Mihalic, J. Houghtaling, S. Ramachandran, and P. Yager. Two-dimensional paper network format that enables simple multistep assays for use in low-resource settings in the context of malaria antigen detection. *Analytical Chemistry*, 84(10):4574–4579, 2012.

G. S. Gerlero. OpenFOAM.app: Native OpenFOAM for macOS. `https://github.com/gerlero/openfoam-app`, accessed Feb 15, 2024.

G. S. Gerlero, S. M. Damián, and P. A. Kler. electroMicroTransport v2107: Open-source toolbox for paper-based electromigrative separations. *Computer Physics Communications*, 269:108143, 2021a.

G. S. Gerlero, S. Marquez Damian, F. Schaumburg, N. Franck, and P. A. Kler. Numerical simulations of paper-based electrophoretic separations with open-source tools. *Electrophoresis*, 42 (16):1543–1551, 2021b.

G. S. Gerlero, A. R. Valdez, R. Urteaga, and P. A. Kler. Validity of capillary imbibition models in paper-based microfluidic applications. *Transport in Porous Media*, 141(2):359–378, 2022.

G. S. Gerlero, C. L. A. Berli, and P. A. Kler. Open-source high-performance software packages for direct and inverse solving of horizontal capillary flow. *Capillarity*, 6(2):31–40, 2023.

N. N. Hamidon, G. I. Salentijn, and E. Verpoorte. Enhanced passive mixing for paper microfluidics. *RSC advances*, 11(41):25677–25685, 2021.

P. Horgue, F. Renard, G. S. Gerlero, R. Guibert, and G. Debenest. porousMultiphaseFoam v2107: An open-source tool for modeling saturated/unsaturated water flows and solute transfers at watershed scale. *Computer Physics Communications*, 273:108278, 2022.

H. Jasak. *Error analysis and estimation for the finite volume method with applications to fluid flows*. PhD thesis, Department of Mechanical Engineering, Imperial College of Science, Technology and Medicine, London, UK, 1996.

A. J. Ladd and P. Szymczak. Reactive flows in porous media: challenges in theoretical and numerical methods. *Annual review of chemical and biomolecular engineering*, 12:543–571, 2021.

T. Liang, R. Robinson, J. Houghtaling, G. Fridley, S. A. Ramsey, and E. Fu. Investigation of reagent delivery formats in a multivalent malaria sandwich immunoassay and implications for assay performance. *Analytical chemistry*, 88(4):2311–2320, 2016.

P. Lichtner, G. Hammond, C. Lu, S. Karra, G. Bisht, B. Andre, R. Mills, and J. Kumar. PFLOTRAN User Manual: A massively parallel reactive flow and transport model for describing subsurface processes. https://www.pflotran.org/, 2017.

D. Mabey, R. W. Peeling, A. Ustianowski, and M. D. Perkins. Diagnostics for the developing world. *Nature Reviews Microbiology*, 2(3):231–240, 2004.

J. Macagno, G. S. Gerlero, M. L. Satuf, and C. L. A. Berli. Field-deployable aptasensor with automated analysis of stain patterns for the detection of chlorpyrifos in water. *Talanta*, 252: 123782, 2023.

D. Merkel et al. Docker: lightweight linux containers for consistent development and deployment. *Linux Journal*, 239(2):2, 2014.

S. Modha, C. Castro, and H. Tsutsui. Recent developments in flow modeling and fluid control for paper-based microfluidic biosensors. *Biosensors and Bioelectronics*, 178:113026, 2021.

F. Pena-Pereira, L. Villar-Blanco, I. Lavilla, and C. Bendicho. Test for arsenic speciation in waters based on a paper-based analytical device with scanometric detection. *Analytica chimica acta*, 1011:1–10, 2018.

D. Rath and B. J. Toley. Modeling-guided design of paper microfluidic networks: a case study of sequential fluid delivery. *ACS Sensors*, 6(1):91–99, 2020.

F. Schaumburg, P. A. Kler, and C. L. A. Berli. Numerical prototyping of lateral flow biosensors. *Sensors and Actuators B: Chemical*, 259:1099–1107, 2018a.

F. Schaumburg, R. Urteaga, P. A. Kler, and C. L. A. Berli. Design keys for paper-based concentration gradient generators. *Journal of Chromatography A*, 1561:83–91, 2018b.

F. Schaumburg, J. P. Vidocevich, G. S. Gerlero, N. Pujato, J. Macagno, P. A. Kler, and C. L. Berli. A free customizable tool for easy integration of microfluidics and smartphones. *Scientific Reports*, 12(1):8969, 2022.

A. Sharma, B. K. Kashyap, and N. Puranik. *State-of-the-art of paper-based technology and challenges in its commercialization*, pages 11–1–11–20. IOP Publishing Bristol, UK, 2023.

H. A. Silva-Neto, I. V. Arantes, A. L. Ferreira, G. H. do Nascimento, G. N. Meloni, W. R. de Araujo, T. R. Paixão, and W. K. Coltro. Recent advances on paper-based microfluidic devices for bioanalysis. *TrAC Trends in Analytical Chemistry*, 158:116893, 2023.

J. Tirapu-Azpiroz, A. F. Silva, M. E. Ferreira, W. F. L. Candela, P. W. Bryant, R. L. Ohta, M. Engel, and M. B. Steiner. Modeling fluid transport in two-dimensional paper networks. *Journal of Micro/Nanolithography, MEMS, and MOEMS*, 17(2):025003–025003, 2018.

C. J. Toft, R. A. Bourquin, A. E. Sorenson, P. F. Horwood, J. D. Druce, and P. M. Schaeffer. Analytical sensitivity of COVID-19 rapid antigen tests: A case for a robust reference standard. *Talanta Open*, 7:100187, 2023.

R. Urteaga, E. Elizalde, and C. L. A. Berli. Transverse solute dispersion in microfluidic paper-based analytical devices (μpads). *Analyst*, 143(10):2259–2266, 2018.

N. Wang, J. Zhang, B. Xiao, and A. Chen. Microfluidic-assisted integrated nucleic acid test strips for poct. *Talanta*, page 125150, 2023.

H. G. Weller, G. Tabor, H. Jasak, and C. Fureby. A tensorial approach to computational continuum mechanics using object-oriented techniques. *Computers in Physics*, 12(6):620–631, 1998.

X. Yang, H. Sun, Y. Yang, Y. Liu, and X. Li. Recent progress in multi-scale modeling and simulation of flow and solute transport in porous media. *Wiley Interdisciplinary Reviews: Water*, 8(6):e1561, 2021.

Doctorado en Ingeniería
mención Mecánica computacional

Título de la obra:

Modelado y simulación de fenómenos de flujo y transporte en medios porosos integrados a dispositivos de microfluídica

Autor: Gabriel Santiago Gerlero

Lugar: Santa Fe, Argentina

Palabras Claves:

microfluídica en papel, simulaciones numéricas, medios porosos, flujo capilar, electroforesis en papel, transporte reactivo, flujo lateral, OpenFOAM, caracterización experimental, mecánica computacional